High-precision Fluorescence Photometry for Real-time Biomarkers Detection

Thèse

Vahid Khojasteh Lazarjan

Doctorat en génie électrique
Philosophiæ doctor (Ph. D.)

Québec, Canada

High-precision Fluorescence Photometry for Real-time Biomarkers Detection

Thèse

Vahid Khojasteh Lazarjan

Sous la direction de :

Benoit Gosselin, directeur de recherche

Pierre Marquet, codirecteur de recherche

Résumé

Les derniers évènements planétaires et plus particulièrement l'avènement sans précédent du nouveau coronavirus augmente la demande pour des appareils de test à proximité du patient. Ceux-ci fonctionnent avec une batterie et peuvent identifier rapidement des biomarqueurs cibles. Pareils systèmes permettent aux utilisateurs, disposant de connaissances limitées en la matière, de réagir rapidement, par exemple dans la détection d'un cas positif de COVID-19. La mise en œuvre de l'élaboration d'un tel instrument est un projet multidisciplinaire impliquant notamment la conception de circuits intégrés, la programmation, la conception optique et la biologie, demandant tous une maîtrise pointue des détails. De plus, l'établissement des spécifications et des exigences pour mesurer avec précision les interactions lumière-échantillon s'additionnent au besoin d'expérience dans la conception et la fabrication de tels systèmes microélectriques personnalisés et nécessitent en elles-mêmes, une connaissance approfondie de la physique et des mathématiques.

Ce projet vise donc à concevoir et à mettre en œuvre un appareil sans fil pour détecter rapidement des biomarqueurs impliqués dans des maladies infectieuses telles que le COVID-19 ou des types de cancers en milieu ambulatoire. Cette détection se fait grâce à des méthodes basées sur la fluorescence. La spectrophotométrie de fluorescence permet aux médecins d'identifier la présence de matériel génétique viral ou bactérien tel que l'ADN ou l'ARN et de les caractériser. Les appareils de paillasse sont énormes et gourmand énergétiquement tandis que les spectrophotomètres à fluorescence miniatuarisés disponibles dans le commerce sont confrontés à de nombreux défis. Ces appareils miniaturisés ont été découverts en tirant parti des diodes électroluminescentes (DEL) à semi-conducteurs peu coûteuses et de la technologie des circuits intégrés. Ces avantages aident les scientifiques à réduire les erreurs possibles, la consommation d'énergie et le coût du produit final utilisé par la population. Cependant, comme leurs homologues de paillasse, ces appareils POC doivent quantifier les concentrations en micro-volume d'analytes sur une large gamme de longueurs d'onde suivant le cadre d'une économie en ressources. Le microsystème envisagé bénéficie d'une approche de haute

précision pour fabriquer une puce microélectronique CMOS. Ce procédé se fait de concert avec un boîtier personnalisé imprimé en 3D pour réaliser le spectrophotomètre à la fluorescence nécessaire à la détection quantitative d'analytes en microvolume. En ce qui a trait à la conception de circuits, une nouvelle technique de mise à auto-zeroing est appliquée à l'amplificateur central, celui-ci étant linéarisé avec des techniques de recyclage et de polarisation adaptative. Cet amplificateur central est entièrement différentiel et est utilisé dans un amplificateur à verrouillage pour récupérer le signal d'intérêt éclipsé par le bruit. De plus, l'augmentation de la sensibilité de l'appareil permet des mesures quantitatives avec des concentrations en micro-volume d'analytes ayant moins d'erreurs de prédiction de concentration. Cet avantage cumulé à une faible consommation d'énergie, un faible coût, de petites dimensions et un poids léger font de notre appareil une solution POC prometteuse dans le domaine de la spectrophotométrie de fluorescence.

La validation de ce projet s'est fait en concevant, fabriquant et testant un prototype discret et sans fil. Son article de référence a été publié dans IEEE LSC 2018. Quant à la caractérisation et l'interprétation du prototype d'expériences in vitro à l'aide d'une interface MATLAB personnalisée, cet article a été publié dans IEEE Sensors journal (2021). Les circuits intégrés et les photodétecteurs ont été fabriqués ont été conçus et fabriqués par Cadence en 2019. Relativement aux solutions de circuit proposées, elles ont été fabriquées avec la technologie CMOS 180 nm et publiées lors de la conférence IEEE MWSCAS 2020. Tout comme cette dernière contribution, les expériences in vitro avec le dispositif proposé incluant la puce personnalisée et le boîtier imprimé en 3D ont été réalisés et les résultats électriques et optiques ont été soumis au IEEE Journal of Solid-State Circuits (JSSC 2022).

Abstract

The most recent and unprecedented experience of the novel coronavirus increases the demand for battery-operated near-patient testing devices that can rapidly identify the target biomarkers. Such systems enable end-users with limited resources to quickly get feedback on various medical tests, such as detecting positive COVID-19 cases. Implementing such a device is a multidisciplinary project dealing with multiple areas of expertise, including integrated circuit design, programming, optical design, and biology, each of which needs a firm grasp of details. Alongside the need for experience in designing and manufacturing custom microelectronic systems, establishing the specifications and requirements to precisely measure the light-sample interactions requires an in-depth knowledge of physics and mathematics.

This project aims to design and implement a wireless point-of-care (POC) device to rapidly detect biomarkers involved in infectious diseases such as COVID-19 or different types of cancers in an ambulatory setting using fluorescence-based methods. Fluorescence spectrophotometry allows physicians to identify and characterize viral or bacterial genetic materials such as DNAs or RNAs. The benchtop devices that are currently available are bulky and power-hungry, whereas the commercially available miniaturized fluorescence spectrophotometers are facing many challenges. Many of these difficulties have been resolved in literature thanks to inexpensive semiconductor light-emitting diodes (LEDs) and integrated circuits technology. Such advantages aid scientists in decreasing the size, power consumption, and cost of the final product for end-users. However, like the benchtop counterparts, such POC devices must quantify micro-volume concentrations of analytes across a wide wavelength range under an economy of resources. The envisioned microsystem benefits from a high-precision approach to fabricating a CMOS microelectronic chip combined with a custom 3D-printed housing. This implementation results in a fluorescence spectrophotometer for qualitative and quantitative detection of micro-volume analytes. In terms of circuit design, a novel switched-biasing ping-pong auto-zeroed technique is applied to the core amplifier, linearized with recycling and adaptive biasing techniques. The fully differential core amplifier is utilized within a lock-in amplifier to retrieve the signal of interest overshadowed by noise.

Increasing the device's sensitivity allows quantitative measurements down to micro-volume concentrations of analytes with less concentration prediction error. Such an advantage, along with low-power consumption, low cost, low weight, and small dimensions, make our device a promising POC solution in the fluorescence spectrophotometry area.

The approach of this project was validated by designing, fabricating, and testing a discrete and wireless prototype. Its conference paper was published in IEEE LSC 2018, and the prototype characterization and interpretation of *in vitro* experiments using a custom MATLAB interface were published in IEEE Sensors Journal (2021). The integrated circuits and photodetectors were designed and fabricated by the Cadence circuit design toolbox (2019). The proposed circuit solutions were fabricated with 180-nm CMOS technology and published at IEEE MWSCAS 2020 conference. As the last contribution, the *in vitro* experiments with the proposed device, including the custom chip and 3D-printed housing, were performed, and the electrical and optical results were submitted to the IEEE Journal of Solid-State Circuits (JSSC 2022).

Table of contents

List of figures

List of tables

List of abbreviations

3D	3-dimension
ADC	Analog to Digital Converter
BPF	Band Pass Filter
CC	Coarse Counter
CG	Conversion Gain
CPS	Coarse Phase Selector
CPSL	Coarse Phase-Shifting Line
CTIA	Capacitive Transimpedance Amplifier
DCU	Digital Control Unit
DFT	Discrete Fourier Transform
DUT	Device Under Test
EOS	End of Scan
FC	Fine Counter
FOV	Field of View
FPS	Fine Phase Selector
FPSL	Fine Phase-Shifting Line
FVF	Flipped Voltage Follower
ISM	Industrial, Scientific, and Medical
LCMFB	Local Common Mode Feedback
LDR	Linear Dynamic Range
LED	Light Emitting Diodes
LIA	Lock-in Amplifier

LNA	Low Noise Amplifier
LOD	Limit of Detection
LOQ	Limit of Quantification
LPF	Low Pass Filter
MAE	Mean Absolute Error
MSE	Mean Squared Error
NA	Numerical Aperture
NEP	Noise Equivalent Power
PBS	Phosphate-Buffered Saline
PCB	Printed Circuit Board
PD	Photodiode
PGA	Programmable Gain Amplifier
POC	Point of Care
RFC	Recycling Folded Cascode
RMSE	Root Mean Squared Error
RSD	Relative Standard Deviation
SC	Switched Capacitor
SNR	Signal-to-Noise Ratio
SPI	Serial Peripheral Interface
SR	Slew Rate
SUT	Sample Under Test

Acknowledgment

First and foremost, I would like to express my sincere appreciation to my supervisor, Professor Benoit Gosselin. I cannot thank him enough for his constant support, encouragement, and inspiration and for providing me with an environment where I could perform my research autonomously and yet in a structured way.

I wish to thank Professor Pierre Marquet for guiding my research, providing me with the resources, and allowing me to work in his laboratories.

I would also like to thank Professor Wei Shi for his insightful and valuable comments and criticism that helped the project progress.

I am also thankful to Professor Alain Garnier for his support and contribution during my research and allowing me to use his laboratory facilities.

I would like to thank members of my dissertation committee for their time, insightful feedback and helpful comments that led to improvements in this work.

Thanks to all my lab-mates for their constant friendship and practical help throughout this journey, and for all the pleasant and insightful conversations that we had through the stressful times.

I would like to thank my family for their constant support and advice. Finally and yet importantly, I want to thank my wife, Anahita, for always believing in me. The completion of this project could not have been possible without her encouragement, motivation, and support.

Foreword

The current dissertation includes a general introduction, four chapters, and a general conclusion. The introduction states the basics, challenges, and the motivation of the research, the chapter 1 covers the literature review, and then the chapter 2 states the methodology of this thesis. The following two chapters are based on published or under review results in IEEE journals, in which the text and figures are modified for better coherency. The 3rd chapter consists of the materials published in the IEEE Sensors Journal. The 4th chapter includes the results submitted to the IEEE Journal of Solid-State Circuits (JSSC). Finally, the last chapter concludes the study and projects the future of this work. The followings are the publications resulted from this work.

Paper 1: **V. K. Lazarjan**, A. B. Gashti, M. Feshki, A. Garnier, and B. Gosselin, "Miniature Fiber-Spectrophotometer for Real-Time Biomarkers Detection," in IEEE Sensors Journal, vol. 21, no. 13, pp. 14822-14837, 1 July1, 2021. I am the main designer of the system and the algorithm and I wrote the entire article jointly with Dr B. Gosselin, who supervised the research work and contributed ideas. The measurements were done in the Smart Biomedical Microsystems Lab and the laboratories of Dr. A. Garnier at Laval University. Dr. A. B. Gashti contributed to the design of the *in vitro* experiments and measurements, and M. Feshki was involved in the design of the algorithm.

Paper 2: **V. K. Lazarjan**, M. N. Khiarak, A. B. Gashti, A. Garnier, and Benoit Gosselin. "Miniaturized Wireless Cell Spectrophotometer Platform in Visible and Near-IR Range." In 2018 IEEE Life Sciences Conference (LSC), pp. 29-32. IEEE, 2018. I am the main designer of this platform and I wrote the article under the supervision of Dr. B. Gosselin who conducted the whole project. All measurements were done in the Smart Biomedical Microsystems Lab and the laboratories of Dr. A. Garnier at Laval University. Dr. M. N. Khiarak contributed to the design of the 3D-printed housing. Dr. A. B. Gashti contributed to the design of the *in vitro* experiments, and experimental measurements.

Paper 3: **V. K. Lazarjan**, S. N. Hosseini, M. N. Khiarak, and B. Gosselin. "CMOS Optoelectronic Sensor with Ping-pong Auto-zeroed Transimpedance Amplifier." In 2020 IEEE 63rd International Midwest Symposium on Circuits and Systems

(MWSCAS), pp. 17-20. IEEE, 2020. I am the main designer of this project and the entire article is written by me under the supervision of Dr. B. Gosselin who conducted the whole research project. S. N. Hosseini contributed to part of the layout section and Dr. M. N. Khiarak was involved in part of the design section.

Paper 4: **V. K. Lazarjan**, M. Crochetière, M. N. Khiarak, S. A. Aarani, S. N. Hosseini, P. Marquet, B. Gosselin. "High-Precision Ping-pong Auto-zeroed Lock-in Fluorescence Photometry Sensor." Submitted to IEEE Journal of Solid-State Circuits (JSSC 2022). I am the main designer of this project and I wrote the entire article under the supervision of Dr. B. Gosselin who conducted the whole research project. The measurements were performed in the Smart Biomedical Microsystems Lab, and the *in vitro* measurements were conducted at CERVO, the laboratory of Dr. P. Marquet at Laval University. Dr. P. Marquet and M. Crochetière contributed to designing the *in vitro* experiments, including the preparation of cells, and the tag process. Dr. M. N. Khiarak, S. G. Aarani, and S. N. Hosseini were involved in the design and layout process.

Introduction

Exploring the presence, the abundance, the localization, and the fluctuations of various biomarkers in cell culture through the fluorescence cell photometry systems has received significant attention, and has been vastly studied during the recent decades [1]–[3]. Such a luminescence-based method allows physicians to rapidly identify the existence of viral materials initiating contiguous diseases [2]. Opportune detection of viruses such as coronavirus can significantly lessen the number of fatalities [3], [4]. Using a precise and prompt method such as fluorescence cell photometry could control the number of occurring waves and prevent multiple pandemics by rapidly identifying and quarantining the infected people and following the course of treatment in the confirmed cases. Such a strategy could also be helpful in the event of other epidemics such as HIV and Ebola.

Fluorescence cell spectrophotometry can identify unhealthy tissues by characterizing and analyzing the samples containing abnormal cells. Physicians can diagnose tumors and determine their either malignant or benign state [5]–[8]. Physicians can estimate an accurate prognosis of a patient's cancer and determine the stages of a tumor using precise benchtop photometry systems. Responsible for close to 10 million deaths in 2020, cancer is a leading global reason for fatality. Rapid detection of a pre-cancerous lesion and the follow-up screening of the treatment effect can significantly reduce the total mortality.

High-precision and affordable point-of-care (POC) photometry systems are needed to quickly detect viruses, such as SARS-CoV-2 and delay or prevent the spread of contagious diseases [2]. These envisioned POC fluorescence photometry devices would enable disease prevention, early diagnosis, and fast treatment response monitoring by providing quick and frequent biomarkers concentration measurement [3].

The SMAART CREATE program founded by the Natural Sciences and Engineering Research Council of Canada (NSERC) supports the idea of implementing such a smart, autonomous, adaptive and innovative optical

design as part of its satellite partnership with the Sentinel North program. The SMAART program focuses on the engineering of optical devices. It aims to facilitate the connections between university and industry through multiple events that students could acquire transdisciplinary knowledge related to their projects in various fields such as environment, nutrition, and health. Moreover, the Canada Research Chair in Smart Biomedical Microsystems at Laval University supports the idea of this project by providing the necessary training.

In addition, the combination of diverse laboratories in different areas of expertise was necessary to conduct this project. To fulfill the objectives of this project, all the electronic and electrical measurements were performed in the laboratory of Professor Benoit Gosselin at Laval University. The first step of *in vitro* experiments was performed in Professor Alain Garnier's laboratories in the Chemical Engineering Department of Laval University, which led to the first journal publication. The second step of the *in vitro* measurement, including the preparation of the cells, the tagging procedure, and microscopy to confirm the results, was performed in the laboratories of Professor Pierre Marquet in the CERVO research center of Laval University. Such a multidisciplinary collaboration between these groups led to the successful implementation of a miniature microsystem submitted to prestigious IEEE journals.

In conclusion, the importance of the mentioned applications in public life expectancy, the vital role of such an optical technique in these applications, and improving the availability of such an envisioned device in inaccessible places worldwide convince us to continue this ongoing study.

I.1 Principle behind this technique

This section explains the interaction between light and other materials such as biological samples and the important features that can affect this interaction. Then, the possibility of implementing a photodiode in CMOS technology is investigated. Finally, some initial results of my work are presented.

I.1.1 Light-sample Interaction

Light propagates as electromagnetic waves with a travel speed, C, of almost 3 × 10^8 m/s in free space. According to $C = \nu \times \lambda$ equation, there is a direct

Table I.1 Refractive index of various substances (derived from Wikipedia)

Material	Refractive index
Air	1.000
Water	1.333
Cytoplasm	1.350–1.375
Epidermis	1.34–1.43
Viruses	1.5–1.57
Mitochondria	1.38–1.41
Blood	1.355–1.398
Animal Cells	1.35-1.38
Bone	1.55
Nucleus	1.38-1.41

relation between the speed of the light in free space and two characteristics of the propagated waveform light: its wavelength (λ) and frequency (v). Moreover, the speed of light (*S*) traveling through a translucent or transparent medium or biological sample can be slowed down. Eq. I.1 presents the relation between the *C* and *S*.

$$S = \frac{C}{n}, \tag{I.1}$$

where, n is the refractive index of the material to which the light is traveling. Table I.1 presents the refractive index of various materials. For instance, viruses have an average refractive index varying from 1.5 to 1.57. Consequently, the speed of light traveling in biological tissue is around 1.95×10^8 m/s. However, this value changes in many cases based on the wavelength of the light.

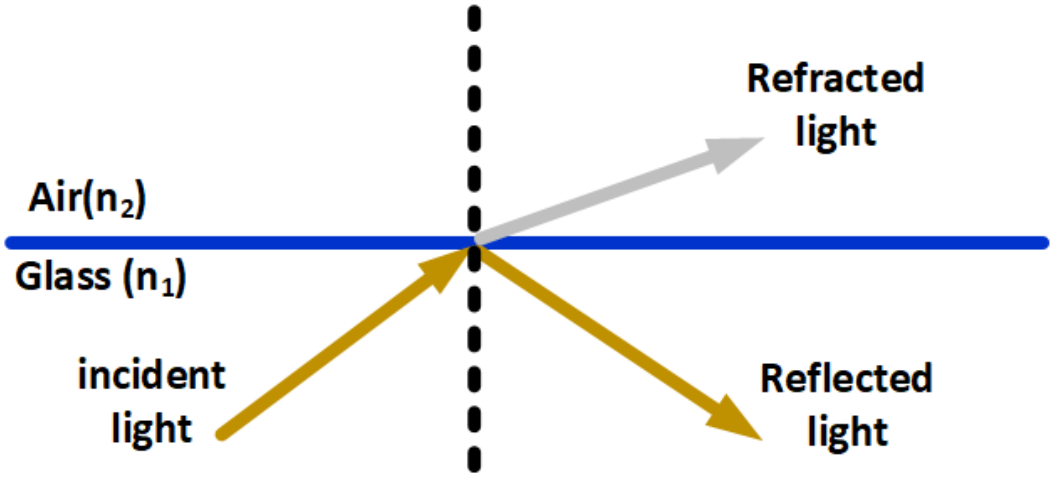

Fig. I.1. Reflection and refraction of light (n_2<n_1).

As shown in Fig. I.1, the fate of the light reaching an interface between two different substances depends on their refractive index. Hence, based on the refractive index of the media, a part of the light will be reflected, and the remaining will be bent (with a slower speed when n_1>n_2) or refracted into the second substance.

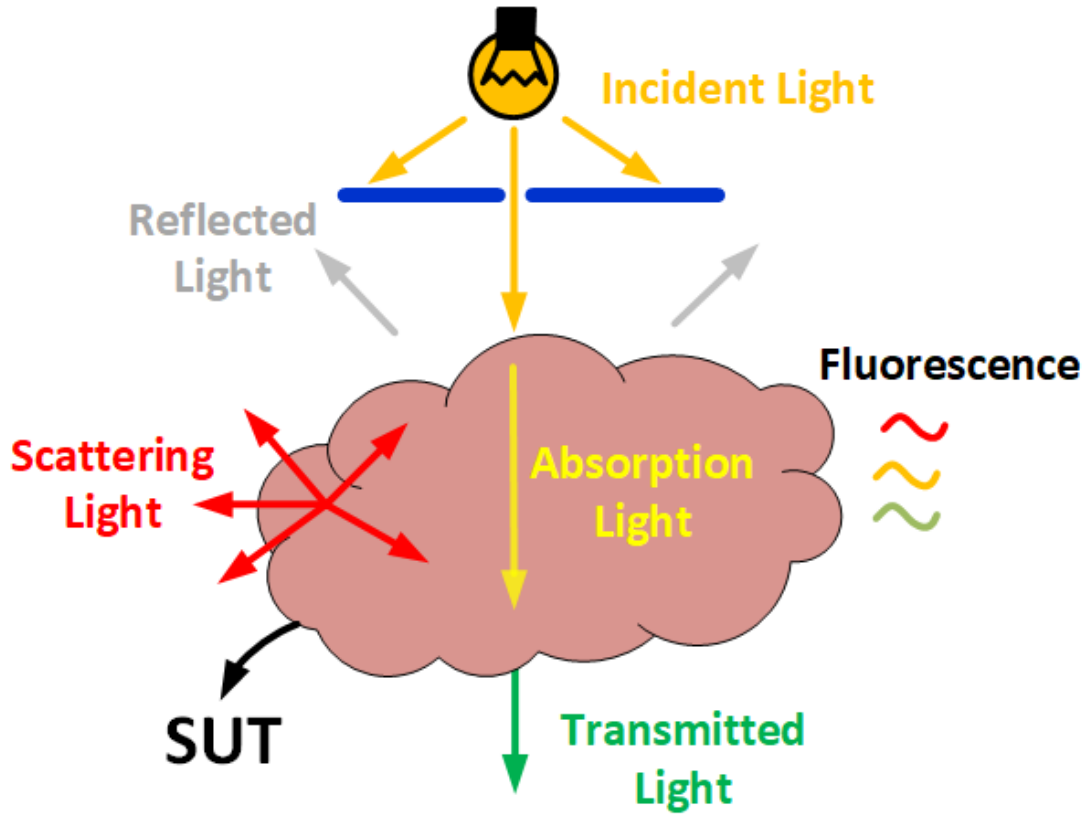

Fig. I.2. Light-sample interaction.

Table I.2 Range of detection for different materials used in photodetectors (derived from Wikipedia)

Material	Electromagnetic spectrum wavelength range (nm)
Silicon	190-1100
Germanium	400–1700
Indium gallium arsenide	800–2600
Lead(II) sulfide	<1000–3500
Mercury cadmium telluride	400–14000

The optical properties of the biological substances could vary based on the wavelength of the light. Other factors such as temperature, optical power per area irradiated, light exposure time, and light polarization can affect the optical properties of a sample [9].

The wavelength of the source light, the light power of the source, the irradiance, the irradiated area, the beam variation before reaching the sample, the on-time of the source light, the beam variation over time, the source irradiance variation over the wavelength, and the source light polarization are some of the important parameters that influence the biological sample reaction to the light exposure.

Fig. I.2 shows the interaction between light and a sample under test (SUT), comprising fluorescence, absorption, reflection, and scattering that can be used to analyze the biological samples.

I.1.2 Photodiode

A photodiode is a semiconductor device that converts light into an electrical current. The material used to make a photodiode is critical in defining its properties because only photons with sufficient energy to excite electrons across the material's bandgap can produce significant photocurrents. Materials commonly used to produce photodiodes are listed in Table I.2.

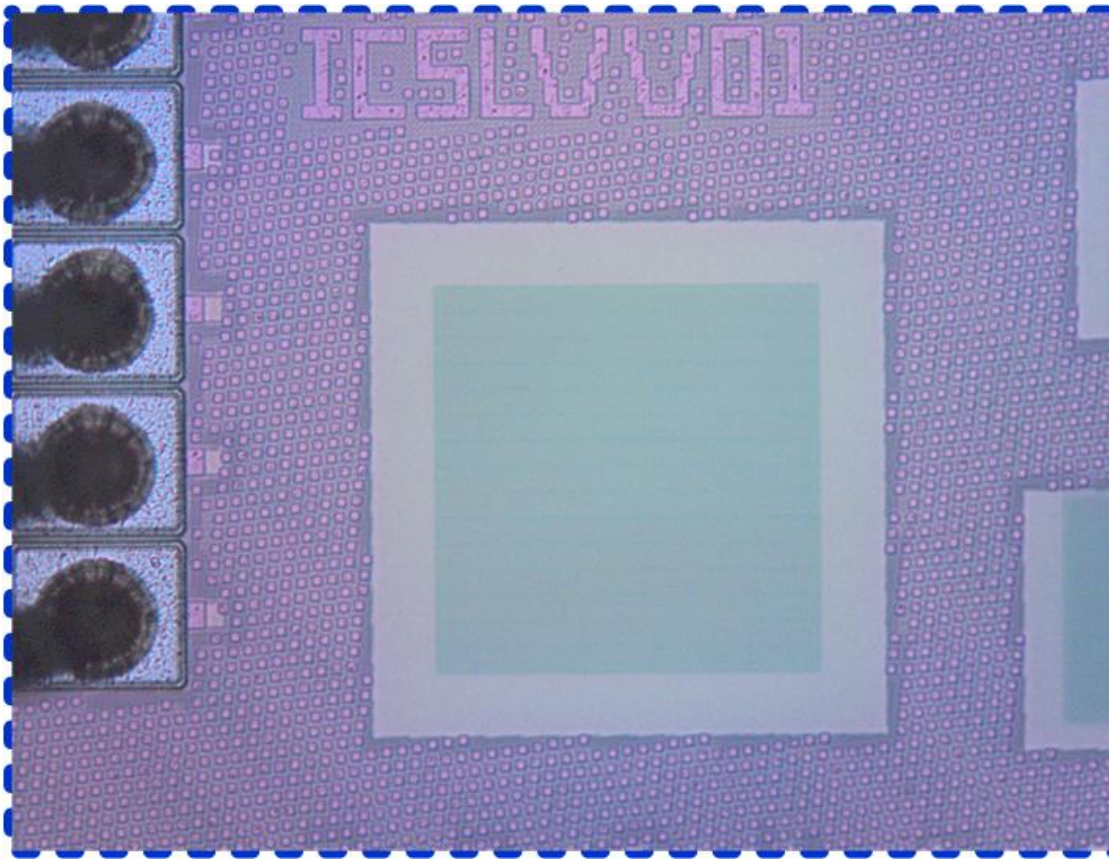

Fig. I.3. Microphotograph of the implemented photodiode with 65 nm CMOS technology.

Table I.2 shows that the whole range of spectrum wavelengths for this project, which is in blue and green range, is detectable by silicon material. Therefore,

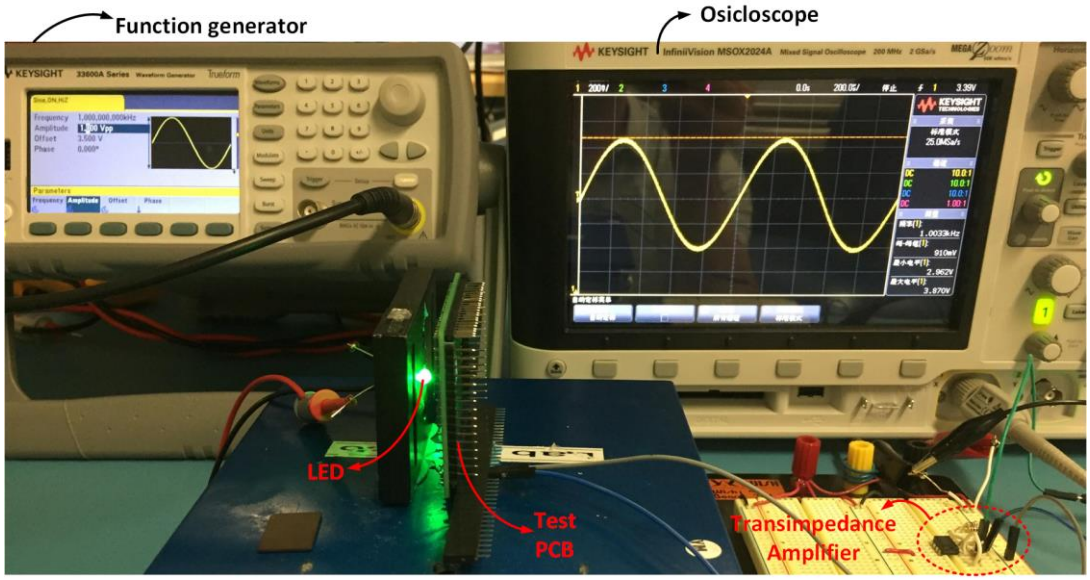

Fig. I.4. Test setup to validate the functionality of the implemented photodiode.

designing a photodetector with CMOS technology is a practical way to detect UV and NIR light. To have an experimental result, we implemented a chip with a photodiode. The microphotograph of the photodiode, which is implemented with 65 nm CMOS technology, is shown in Fig. I.3. As shown in Fig. I.4, the test setup includes an LED, a function generator, and an oscilloscope. In addition, a transimpedance amplifier converts the output current of the photodiode into a voltage signal. In this experiment, the LED functions with a sinusoidal input with 1 kHz frequency. The oscilloscope detects a voltage with the same frequency. The same experiment with different colors and amplitude showed the implemented photodiode's functionality for the subsequent experiments.

I.1.3 Preliminary Results

The preliminary prototype uses a Hamamatsu mini spectrometer C12880MA. The Hamamatsu C12880MA employs a reflective concave blazed grating formed by nanoimprint. It also has a CMOS image sensor chip integrated with the optical slit by etching technology. The incident light passes the input slit, and the grating chip diffracts the coming light to different wavelengths, which are finally detected by the CMOS linear image sensor. The image sensor delivers the intensity value of each wavelength, based on the resolution of the C12880MA, to its output node. After this step, the data should be amplified, digitized, and transmitted to the receiver. The output of the preliminary sensor

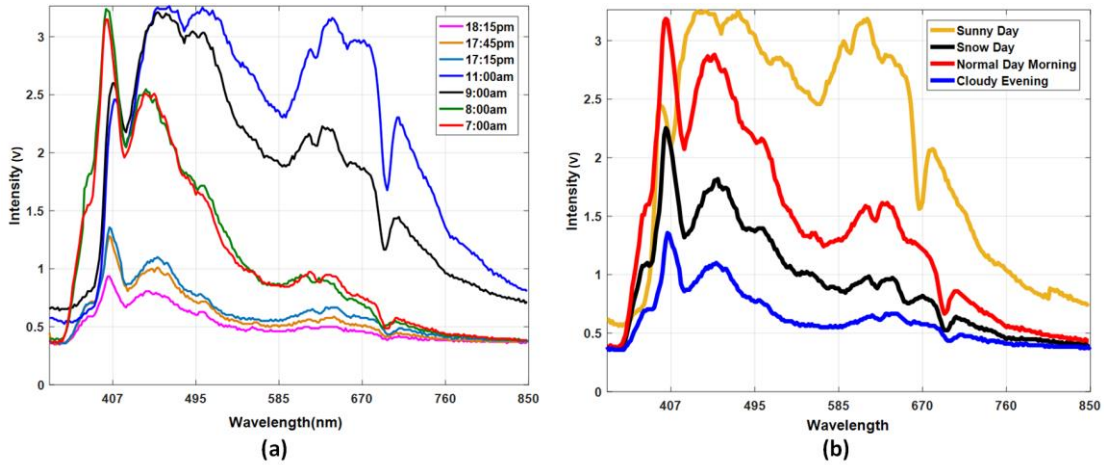

Fig. I.5. Measured ambient light intensities: (a) during one day (b) on different types of weather in different days.

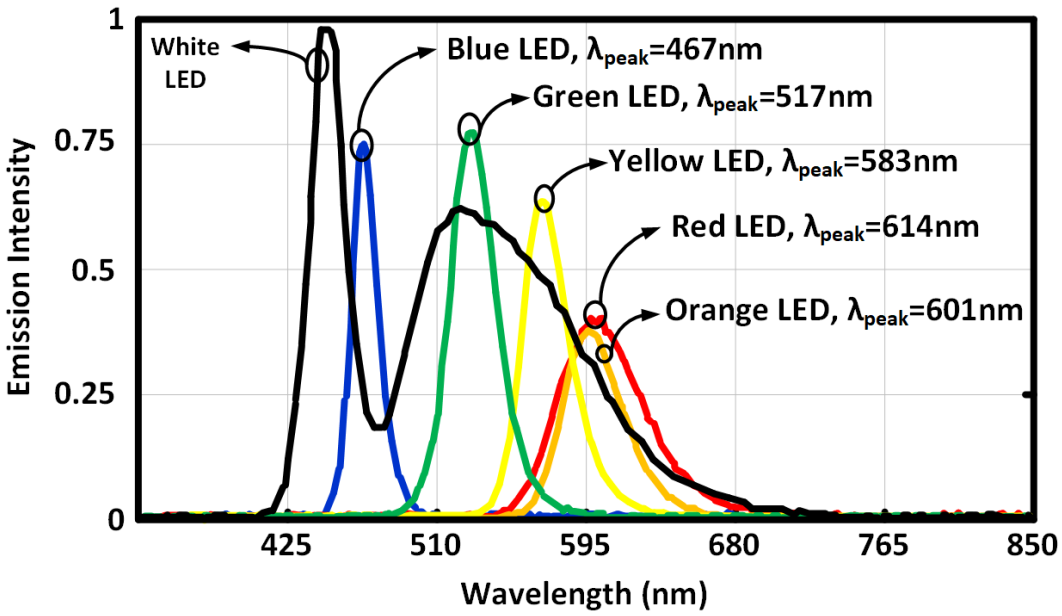

Fig. I.6. Measured spectrum of different LEDs with different wavelengths.

delivers serial data to a microcontroller (MSP430). The output of the microcontroller is then transmitted to the receiver using the NRF24l01 module. Finally, another microcontroller delivers the data to the computer using a USB cable. The final data delivered to the computer are processed and plotted using MATLAB codes.

The preliminary prototype functionality was tested using several experiments. First, Fig. I.5 (a) shows different ambient light intensities during one day, and Fig. I.5 (b) shows the recorded ambient light intensities under different weather conditions on different days. Such measurements show the capability of the preliminary prototype to detect different intensities. Then, the intensities of different colors of LEDs were measured to show the ability of the preliminary prototype to differentiate between different wavelengths. Fig. I.6 shows the ability of the device to identify different colors of LEDs.

Based on the presented results, further modifications and experiments have been applied to the preliminary prototype to realize a fluorescence-based cell spectrophotometer setup.

I.2 Contribution

In this research, fluorescence-based designs are explored to propose a portable, precise, and low-power device that can be used under the limited accessibility to bulky and costly facilities. The scheme consists of an LED, fiber, optical filters and lenses, 3D-printed housing, CMOS optical sensors, and electronic circuitries. The proposed design aims to provide the features of benchtop and conventional cell spectroscopy systems in detecting and extracting optical data. The whole thesis introduces two main setups, and each work's contribution is described in the following lines.

- The first design uses wireless spectrally resolved fluorescence cell fiber photometry system. 1- Using a multi-wavelength CMOS photo sensor in this design avoids the utilization of an emission filter in the path of the reflected light allowing more power to reach the photodetector. Such a scheme can increase the sensitivity of the prototype. Observing the performed experiments with and without this technique shows a three times sensitivity improvement. 2- The spectrally resolved scenario decreases the concentration prediction error by measuring the whole spectrum instead of a narrow wavelength band. 3- Such an improvement of the sensitivity enables the device to identify and quantify the micro-volume concentrations of analytes. 4- A high correlation coefficient square (R^2) between the analyte concentrations and the measured light emission intensities shows the ability of the prototype to quantify a wide range of different concentrations linearly. 5- Increasing the sensitivity allows the prototype to utilize a lower LED power to illuminate the analytes. 6- The proposed device can be used with multiple fluorophores in different wavelengths by changing the optical components, providing flexibility and high selectivity. 7- The low power consumption of the proposed design allows the prototype to work with a small battery for a long period. 8- It comprises a transceiver and antenna to transmit the extracted data to the base station for real-time presentation of the results and further raw data processing. 9- The design has a featherweight, an economical price, and has low-power consumption, making it a promising POC system.

- 1- The second design utilizes a fully differential front-end detection TIA that includes a switched-biasing ping-pong auto-zeroed technique to decrease the input-referred noise. This noise reduction technique consumes a lower power consumption compared to the previous methods. 2- The performance of the core amplifier is also improved using circuit techniques such as additional cascode, adaptive biasing, and recycling. The results show that the input noise is reduced while the power is constant compared to previous reports. 3- The presented work also uses automatic phase-alignment feedback to achieve the maximum sensitivity of the LIA. 4- Two photodiodes (PDs) as the optical sensors are implemented on the same die alongside the circuits to make a fully integrated optoelectronic sensor. 5- A miniature setup as a preliminary POC device is designed, including the LIA chip and other optical components to perform the *in vitro* tests. The results reveal that the proposed LIA can successfully detect different intensities of the light and deliver the corresponding DC voltages. 6- The extremely low-noise design and the phase alignment feedback increase the device's sensitivity to detect micro-volume samples. 7- Requiring low energy, a low cost, and having a lightweight make this design a promising candidate for POC applications.

I.3 Thesis Outline

The thesis is organized as follows: The introduction describes the motivation and the importance of this research together with the contributions. Then, chapter 1 presents the previously reported studies and the best commercially available devices and explains their challenges. The second chapter describes the methodology and road of this study from the beginning by describing the results and outcomes of this PhD and the way that different papers fulfilled the objectives of the project. The third chapter presents the miniature fluorescence fiber-cell spectrophotometry system by describing the design block diagram, implementation procedure, and in vitro results for the whole wireless system. Chapter 4 presents the CMOS fluorescence cell photometry system modified with a ping-pong auto-zeroed lock-in amplifier for real-time biomarkers

detections. Finally, a general conclusion finalizes the thesis, presents future work, and describes the suggested improvements.

Chapter 1

Literature review

In the field of fluorescence-based biosensors, various studies and implementation techniques are presented to detect different types of biomarkers. For instance, in [10], authors employed a fiber in fluorescence photometry approach, termed fiber photometry, to access neural activity in deep brain structures. Fig. 1.1 presents the block diagram of the measurement setup and the part number of the devices used in this study. The proposed setup illuminates the fluorescent materials with a 1.8-1.9 mW laser that functions at 475 nm wavelength. The emission light is then captured with high sensitivity photodetector and is converted to a voltage signal by a bench top lock-in amplifier. Finally, a data acquisition unit (LabJack DAQ) transmits the data to a computer for further analysis by custom Python software. Such real-time projection enables scientists to study the medication effect on neural activity, encode neuropsychiatric disorders, and assess the contribution of neurons to social interactions. In addition, the social interactions between mice were studied by observing the changes in the intensity of the emission light. In [11], the authors modify such a photometry approach to achieve simultaneous measurements of two fluorophores. Such measurements demonstrate the activities of the neurons from two parallel detection units, and the amplitude of

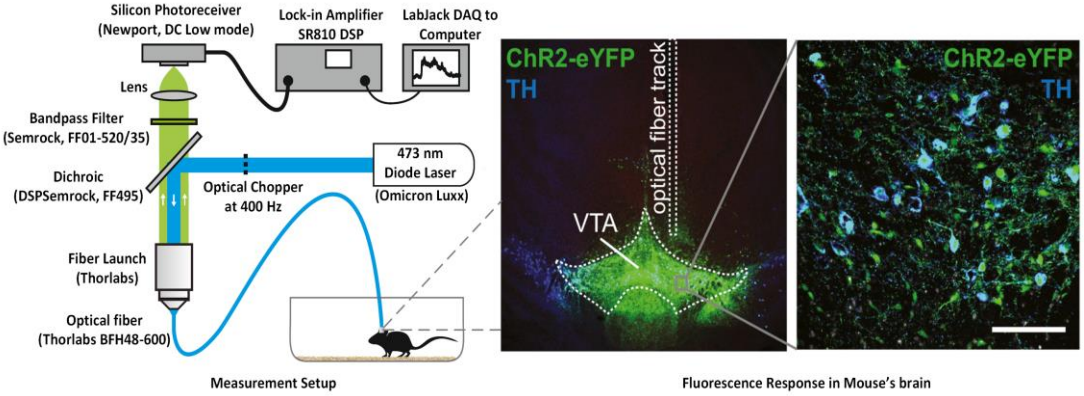

Fig. 1.1. Block diagram of a bench-top fluorescence-based measurement setup and confocal images of fluorescence response in the brain, adapted from [5].

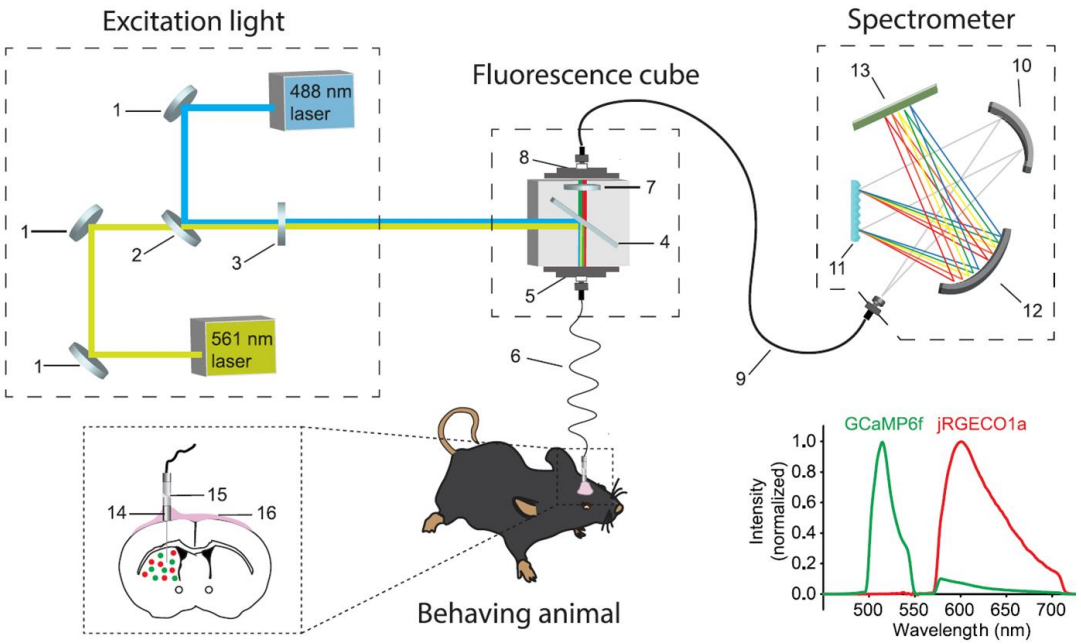

(1): broadband mirrors, (2): laser beam combiner, (3): neutral density filter, (4): dual-edge dichroic beam splitter, (5): front fiber port, (6): 105 mm core multi-mode optical fiber patch cable, (7): dual-band pass emission filter, (8): rear fiber port, (9): 200 mm core multi-mode optical fiber patch cable, (10): collimating mirror, (11): diffraction grating, (12): focusing mirror, (13): linear CCD array, (14): implanted fiber probe with 1.25 mm OD ceramic ferrule, (15): ceramic mating sleeve, (16): dental cement (16).

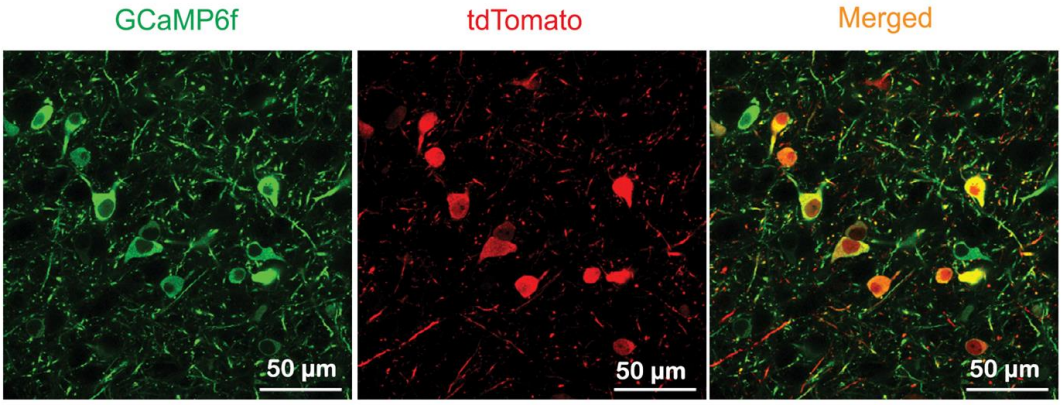

Fig. 1.2. Block diagram of the multi-color measurement setup and the normalized response of two fluorescences. The images at the bottom-side show the response of each color and the merged response, adapted from [24].

their signals coordinately can predict the fate of a movement. Fig. 1.2 shows the block diagram of such a measurement setup that can extract multi-color data and the images from each color, and the merged one.

Benchtop devices are bulky, costly, and require frequent maintenance with specialized personnel [10], [12]. Much effort has been devoted to creating miniaturized devices over the past number of years due to the increasing

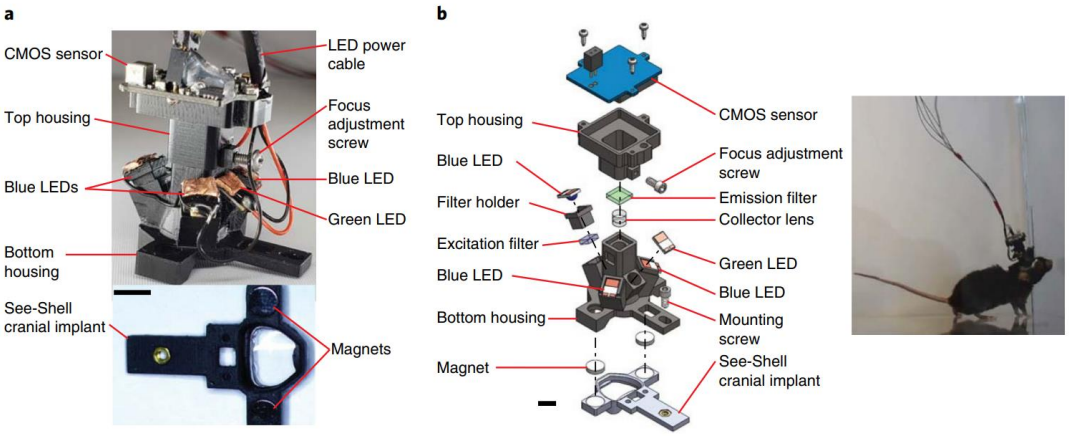

Fig. 1.3. a) Photograph of the mini-mScope. b) Left: 3D representation of the mini-mScope showing each component. Right: an image of a mouse bearing the mini-mScope, adapted from [40].

demand for battery-operated portable equipment and power-saving circuits. An inexpensive POC device could allow effective disease prevention, early diagnosis, accurate drug identification, and direct drug response monitoring [13], [14], by frequently monitoring the localization and the concentration of the biomarkers, including proteins [15], pathogenic nucleic acids [16], RNAs [17], DNAs [13], and creatinine [18]. Miniaturized cell spectrophotometers have been designed by taking advantage of inexpensive semiconductor light-emitting diodes (LEDs), MEMS, and integrated circuits technology to decrease the size, power consumption, and cost of the entire device [19]–[34]. However, these spectrophotometers face many challenges in providing high performance under

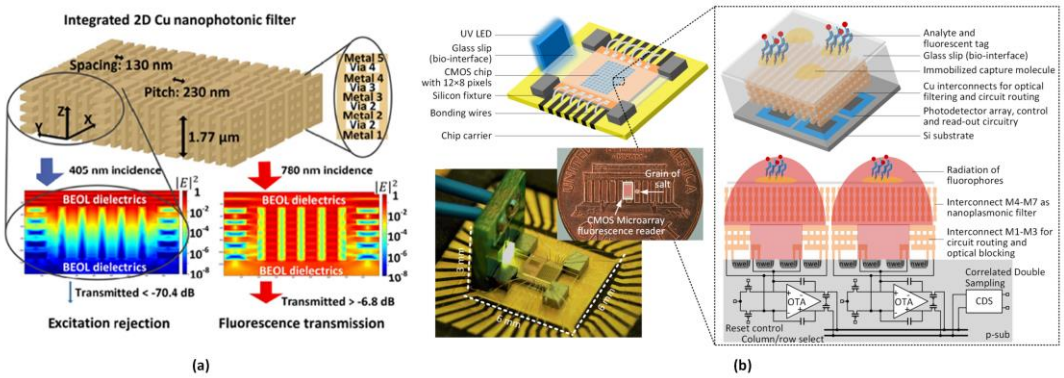

Fig. 1.4. (a) Details of implemented filter that pass the 780 nm and rejects 405 nm. (b) The final design structure and the details of the inner circuits, adapted from [26] and [41].

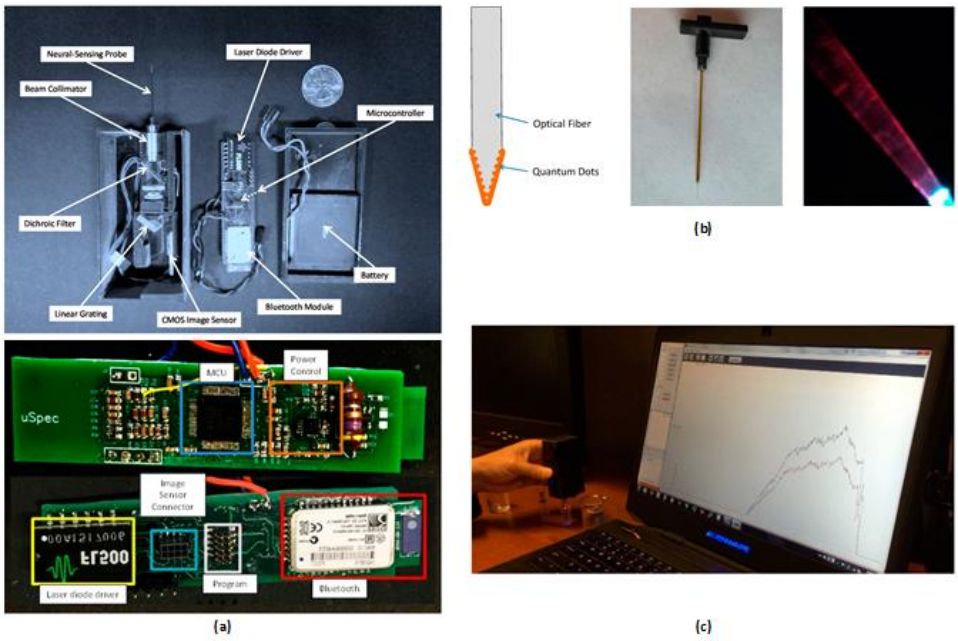

Fig. 1.5. (a) Details of the implemented setup, (b) The optical fiber structure, (c) An image of the experimental setup, adapted from [42].

an economy of resources. Similar to their benchtop counterpart, these spectrophotometers must allow the measurement of micro-volume concentrations of analytes across a wide wavelength range.

Among these miniaturization explorations, as shown in Fig. 1.3 [35], authors provide insights into cellular activities, while the device cannot function wirelessly and does not deliver depth-tissue information. Interpreting the output

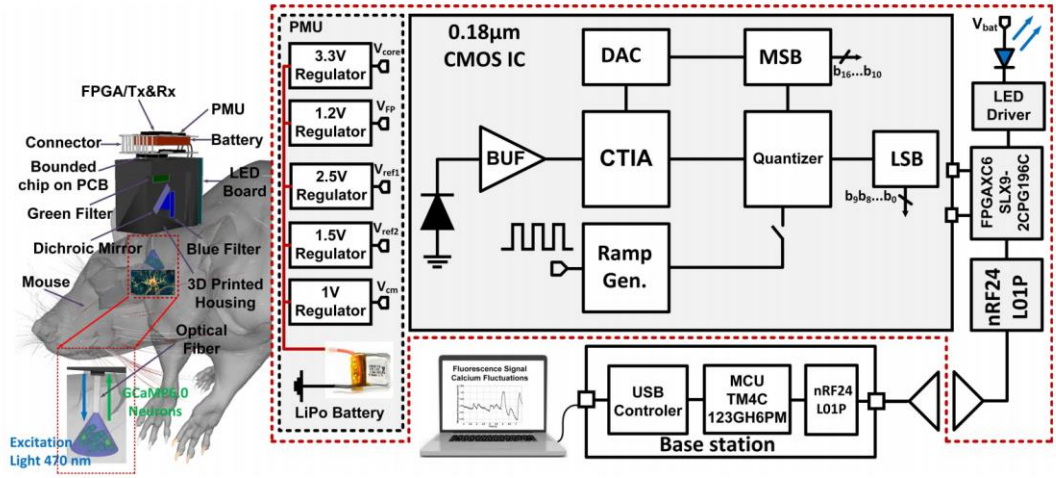

Fig. 1.6. Block diagram of the miniaturized fluorescence-based system utilizing a CTIA, adapted from [21].

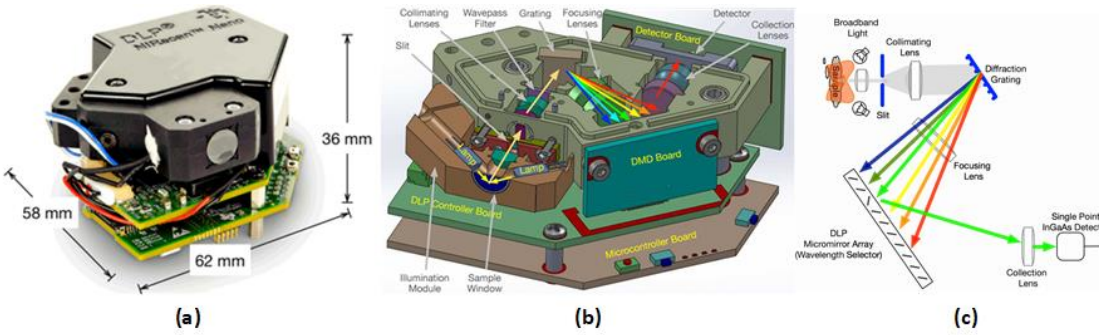

Fig. 1.7. (a) Image of DLP NIRscan Nano device, (b) Graphical details of the DLP, (c) Representing the functioning details of the whole device, adapted from TI.com.

data of such experiments can deeply expand our knowledge of human neural disorders such as Alzheimer.

In [19], [36], as shown in Fig. 1.4, the authors introduced a fully integrated filter on a CMOS chip to decrease the size and power consumption of the spectrophotometer drastically. This device requires a wavelength gap of 400 nm between the excitation and fluorescence lights to operate properly, which confines the use of the spectrophotometer only to a small subset of fluorophores. In [37], Kim et al. designed a high-sensitivity system using a customized optical sensing probe, as shown in Fig. 1.5. Adding CdSe/ZnS quantum dots to the tip of the fiber enhanced the sensing performance of the device with excellent selectivity over uric and ascorbic acids. This work focused on implementing real-time monitoring of dopamine in the brain to study neurological disorders and diseases. However, the size of the probe, the weight of the entire device, and the high current drawn by the LED were substantially

Table 1.1 Characteristics of DLP NIRscan Nano

Key Features	DPL NIRscan Nano
Power	1.2-5 w
EVM Wavelength Range	900-1700 nm
EVM Spectral Resolution	10 nm
size	58 mm × 62 mm × 36 mm

Fig. 1.8. Ocean optics spectroscopy device, USB4000 (left-side) and STS-UV (right-side), adapted from oceaninsight.com.

limiting for a mobile device. In [21], [38], the authors presented a fiber photometry sensor, as shown in Fig. 1.6. The miniaturized fluorescence sensing prototype uses an LED as an excitation light source, a customized CMOS chip, and a band-pass optical filter to block the excitation light and prevent the photodetector saturation while isolating the fluorescence light. However, this prototype cannot discriminate between different wavelengths.

Additionally, the optical band-pass filter contributes to the emission fluorescence light power attenuation, thus decreasing the sensitivity of the

Table 1.2 Ocean Optics components' features

Key Features	USB4000	STS-UV
Configurable range	200 – 1100 nm	190-650 (UV) 350-800 (Vis) 650-1100 (NIR)
Dimensions	89.1 mm x 63.3 mm x 34.4 mm	40 mm x 42 mm x 24 mm
Weight	190 g	60 g
Power Consumption	250 mA @ 5 VDC	150 mA @ 5 VDC

entire device. This phenomenon was circumvented by raising the light power of the excitation LED at the cost of additional energy consumption. However, raising the light source power or the time span of exposure to increase the precision can cause photobleaching [38]. Photobleaching is a photon-induced chemical alteration that can permanently cancel the fluorescence capability of fluorophores. Depending on their chemical bonding, fluorophores can photobleach after absorbing only a few photons, while other molecules with improved photostability can undergo many light absorption/emission cycles before losing their fluorescence capability. Increasing the light intensity raises the fluorophore cycling between the ground and excited states, rendering the SUT remarkably prone to photobleaching [9].

To the best of our knowledge Texas Instruments, Ocean Optics, and Hamamatsu's companies produce the best spectrophotometry sensors in terms of size, power, and wavelength range. Fig. 1.7 (a) shows the digital light processing (DLP) NIRscan Nano device. The presented system is compact and battery-operated, making it a perfect design for portable solutions. The EVM includes a diffraction grating and a detector with a TI processor (Tiva™ TM4C1297NCZAD). Such a handheld design enables scientists to perform food or skin analysis and wear it as a health monitoring system. Table 1.1 shows the key features of this device. Fig. 1.7 (b) shows the different components inside this device. It also shows how the light is going to the detector from the sample. Fig. 1.7 (c) clearly explains the way that it is working. Diffraction grating separates different wavelengths, and micro mirror arrays select and transmit these wavelengths to the detector. Ocean Optics Company also has mini spectrometers shown in Fig. 1.8, and their features are summarized in Table 1.2.

Chapter 2

Methodology

This project aims to design and implement a high-precision wireless POC device for the rapid detection of biomarkers involved in infectious diseases such as coronavirus or different types of cancers in an ambulatory setting using fluorescence-based methods. The results are summarized in two conferences and two journals that are published or submitted. The envisioned microsystem benefits from a multi-technology approach to fabricate a CMOS microelectronic chip in combination with optoelectronics to realize a fluorescence-based POC device for qualitative and quantitative detection of micro-volume analytes. This multidisciplinary project deals with multiple areas of expertise, including integrated circuit design, programming, optical design, and biology, and each needs a firm grasp of details.

This PhD research was started in September 2016 with a background in microelectronic designs. During the first year, the focus was on the biology applications and the possible methods of implementing such a system that requires multiple areas of expertise. In 2017, initial results and solutions for the challenges were presented as part of the pre-doc exam requirements. The approach was then validated by designing, fabricating, and testing a preliminary prototype.

The purpose of the preliminary prototype was to realize a miniature spectrophotometer with discrete components that can autonomously excite and detect the fluorescent emission light emitted from a sample while consuming low power. Also, designing such a prototype helped us study various challenges of implementing a complete photometry system.

This prototype included a Hamamatsu sensor (C12880MA) and a compact multilayer printed circuit board. The layers were stacked and joined together with a rigid custom-designed connector. Using a multistage PCB in this design helped decrease the final device's size. The spectroscopy system detected the emitted light from a sample under test using a fiber with a 1-mm diameter. The

fiber was used to specify the test area. It also helped to prevent the leakage of light into the sensor slit, which improved the quality of the detected signal. A 3D-printed housing was designed to prevent the leakage of light from the input slit of the sensor and was also responsible for holding the fiber. The detected light was processed by analog and digital building blocks, which generated digital code representing the input signal information and were placed on the multistage PCB. The recorded data was transmitted to a base station located a few meters away from the experiment. The antenna and transmission modules were also placed on the upper layer of the multistage PCB. The dimensions of the PCB layers were 3 cm × 2.4 cm × 1 cm. The entire wireless spectroscopy sensor interface was powered by two 3.7 V, 100 mAh, 2.1 g Lithium-ion batteries, which provide 7.4 V when configured together. After sending the data to the computer, the interface provided by MATLAB showed us the intensity of each wavelength detected by the device. This interface was designed with MATLAB to visualize the detected light intensity versus wavelength. Light intensity was normalized from 0 to 1 for the wavelengths from 340 nm to 850 nm.

The main contribution of this work was validating the prototype that can detect fluorescent light and differentiate between different wavelengths. It could also wirelessly deliver the detected light intensity and its corresponding wavelength to a base station. However, this prototype did not include any LED as a light source. Multiple tests were performed to present the functionality of the proposed prototype. First, multicolor LEDs emitting different wavelengths were tested to show the capability of the prototype in detecting the light intensities at different wavelengths. It is also shown that this system can scan a sample, detect incoming light power and transmit corresponding data to a base station for further analysis in the 340 nm to 850 nm range. *In vitro* measurement results with VERO E6 cells tagged with DAPI and Alexa Fluor488 with the help of a microscope lamp were presented to demonstrate its performance. Notable features include the device’s ability to detect light emitted by cells, as well as easy handling. The system's low power consumption (88 mW), its minimal use of hardware resources, and its total weight of 17 g incorporated into a small wireless platform make the device suitable for real-time implementation in the

most common low-power cell spectrophotometer applications. The corresponding conference paper was published at IEEE Life Science Conference (LSC) 2018.

- **V. K. Lazarjan**, M. N. Khiarak, A. B. Gashti, A. Garnier, and Benoit Gosselin. "Miniaturized Wireless Cell Spectrophotometer Platform in Visible and Near-IR Range." In 2018 IEEE Life Sciences Conference (LSC), pp. 29-32. IEEE, 2018.

As mentioned, the first version did not include any light source. In order to complete the photometry system, the prototype needed modifications. Therefore, an LED driver on a tiny PCB, a dichroic filter, and an excitation filter were added to the design. A new 3D-printed housing was then designed to encapsulate all these optical components. Such a 3D-printed housing allowed the excitation light to reach the sample and emission light to reach the photodetector. This new prototype version also included the Hamamatsu sensor (C12880MA), and the multistage PCB comprised of the amplification, digitization, and wireless transmission blocks. Multiple *in vitro* designs were implemented to assess the prototype's functionality and find the possible challenges for a complete fluorescence photometry system.

The main contribution was designing a complete wireless prototype that can excite a sample with LED light at a specific wavelength and then detect the spectrum of the fluorescence emission *in vitro* with high precision. This prototype detects multiple colors, delivering higher precision and less prediction error than conventional fluorescence measurement.

The characterization of the final version and the interpretation of *in vitro* experiments using MATLAB was published in IEEE Sensors Journal 2021. The materials of this journal are presented in Chapter 3. This paper presented a sufficiently sensitive device for detecting micro-volume samples in an ambulatory setting, which was fast enough to identify biomarkers in real-time. The prototype comprises a highly sensitive spectrometer embedded in an inexpensive 3D-printed housing and a custom-designed printed circuit board to transmit the data wirelessly. The prototype includes an LED with an LED driver to illuminate the sample. It also includes optical filters to conduct the emission

and excitation lights through the utilized fiber. In this prototype, the emission band-pass filter of conventional fluorescence photometry systems is removed, and a diffraction grating is replaced, separating the incoming light into multiple colors and providing a better resolution. Such an approach, as demonstrated in the result section of the paper, increases the sensitivity and saves the excitation source power. Multiple *in vitro* experiments are presented in this paper to show the replicability of the same results with a small prediction error for identifying and quantifying a sample such as a tubulin protein, which is the essential constituent of innate cells and is associated with different types of cancer.

It is shown that the prototype consumes 103 mW power, weighs 19 g, with a dimension of 30 mm × 24 mm × 43 mm, and provides a resolution of 15 nm, limit of detection of 25 nM, and responsivity of 85 mV/nW. The results show a better precision compared to previous studies. The comparison table and measurement details are presented in the IEEE Sensors Journal and Chapter 3.

- **V. K. Lazarjan**, A. B. Gashti, M. Feshki, A. Garnier, and B. Gosselin, "Miniature Fiber-Spectrophotometer for Real-Time Biomarkers Detection," in IEEE Sensors Journal, vol. 21, no. 13, pp. 14822-14837, 1 July1, 2021.

Charge-coupled devices (CCD) and CMOS sensors are the two main types of image sensors [39]–[41]. CMOS sensors are always preferable when the primary concern is the cost. CMC Microsystem offers AMS CMOS 0.35 µm process for imaging applications [42]. This process includes an anti-reflective coating which enhances the photodiode sensitivity. Here, we compare AMS 0.35 µm with TSMC 180 nm in terms of size, power, and cost to justify using a TSMC 180nm process in this work.

AMS 0.35 µm has only four metal layers, while TSMC 180 nm includes six metal layers. Using a limited number of metal layers and an older technology node can increase the chip area for a complete and large design such as this project. Moreover, the 180 nm CMOS technology includes a mimcap feature that allows us to implement the capacitors on the same chip to decrease the ending prototype's size drastically. This necessary feature is not available in AMS 0.35

µm. In 180 nm CMOS technology, the transistors can function with 1.8 V supply voltage, and transistors work with a lower threshold voltage compared to the AMS 0.35 µm, which can lead to less power consumption. In terms of price, each 1 mm^2 of one silicon chip fabricated with TSMC 180 nm CMOS technology costs 675$, while the same area fabricated with AMS 0.35 µm costs 1300$. So, more than 48% of the cost is saved when using TSMC 180 nm. Finally, another incentive to choose a standard CMOS process for this project was because it opens the door to the integration of complementary digital circuits along with the photosensor in the same SOC for a future version.

The Cadence interface was used to design, simulate, and fabricate the first chip (2019). The post-layout simulation of this software can provide a precise estimation of the electrical performance and response of the fabricated circuits. The main purpose of designing a chip was to miniaturize the dimension and increase the final device's precision. Such a low-power and miniaturized device is suitable for POC applications. The first chip includes multiple photodetectors in 65 nm technology to test the possibility of implementing a sensor beside the circuit in the same chip. After testing the photodetectors, the proposed circuit solutions were fabricated in 180 nm CMOS technology (2020). The preliminary results were published at IEEE MWSCAS 2020 conference. In this design, a differential switched biasing ping-pong auto-zeroed structure was proposed, which resolves the input DC offset problem and reduces the flicker noise. This conference includes the post-layout simulation results regarding the proposed novelties.

Based on the post-layout simulation results with 0.18 µm CMOS technology at a 1 kHz operating frequency, the transimpedance amplifier of the front-end detection unit has 40 dB gain and a DC offset rejection factor of 16 dB, and its input-referred noise is 90 pA/√Hz. The lock-in amplifier has a sensitivity of 100 mV/nA while consuming only 345 µW power from 1.8 V supply voltage and has an input detection range of 1 pA to 1nA. The main contribution of this work was designing a high-precision system that can decrease the noise and retrieve a small amplitude of the target signal overshadowed by noise. To perform this objective, a lock-in amplifier structure was used. In a lock-in amplifier, the target signal is modulated with a reference frequency at the input, and the

corresponding voltage level can be filtered out at the output even for small target signals with negative input SNR. A switched biasing structure was used to eliminate the input flicker noise to further decrease the noise. Compared to previous designs, as shown in the paper, the sensitivity and input range were increased while consuming low power (345 µW).

- **V. K. Lazarjan**, S. N. Hosseini, M. N. Khiarak, and B. Gosselin. "CMOS Optoelectronic Sensor with Ping-pong Auto-zeroed Transimpedance Amplifier." In 2020 IEEE 63rd International Midwest Symposium on Circuits and Systems (MWSCAS), pp. 17-20. IEEE, 2020.

The core amplifier of the preliminary chip needed modifications to improve the linearity of the op-amp encountering different intensities of incoming light. Therefore, the last chip was designed, fabricated, and tested with all device, circuit, and system-level novelties at the end of 2021. This chip grouped all the functional building blocks of the previous chips to realize a fully integrated LIA-based photometry sensor.

This chip includes two photodiodes and a lock-in amplifier design. The lock-in amplifier consists of three main modules: a front-end module, an output module, and an automatic phase-alignment module. The front-end module consists of a TIA, a band-pass filter, and a programmable gain amplifier. The differential structure of the TIA reads the current of sensing and dummy photodiodes. This differential scheme improves the rejection of imperfections such as the dark current of the photodiodes, noise, and DC offset of the op-amp. The automatic phase-alignment module accurately adjusts the phases of the input and reference signal. Such a phase adjustment increases the precision of the lock-in amplifier, which is explained in detail in chapter 4. The output module comprises a mixer and low-pass filter that are responsible for extracting the output DC voltage corresponding to the detected input light. Finally, this chip is used in a POC prototype that connects the chip's output to a data acquisition unit. The prototype, which includes an optical mirror, lenses, and a small 30 mm × 36mm × 30 mm printed circuit board enclosed inside the 3D-printed housing, consumes 36.7 mW and weighs 120 g. The output voltage of the chip is digitized and delivered with a USB connection to a processing unit

responsible for analyzing, displaying, and storing the fluorescence measurements.

All the modifications of the final chip resulted in a system that presented this thesis's objective, including designing a miniature POC system that provides a high-precision to detect a small amplitude of fluorescence signals overshadowed by considerable noise. This chip is encapsulated in a lightweight and economic POC system that consumes a small amount of power. The proposed POC device is tested with beads solutions and *in vitro* with tagged cells. The experimental results confirmed the realization of a high-precision fluorescence device. The results were submitted to the JSSC journal 2022.

The design is fabricated in a 0.18-µm CMOS process. The measured results show that the LIA can retrieve noisy input signals with a dynamic reserve of 42 dB. It consumes only 0.7 mW from a 1.8 V supply voltage. The measurements show that the LIA can detect a wide range of incident light power from 8 nW to 24 µW, with a sensitivity of 250 V/mW. The proposed design, as presented in the last journal paper, includes multiple system-level and circuit-level novelties to improve the performance of the design. Compared to other solutions, our custom integrated fluorescence sensor includes several novelties that pushed the limits regarding sensitivity and power consumption, two critical parameters for the demonstration of a complete point-of-care prototype. 1) The fluorescence photometry sensor uses a lock-in amplifier scheme to retrieve signals at an extremely low signal-to-noise ratio by modulating the weak fluorescence signal at a known carrier frequency. 2) The design utilizes a fully differential optoelectronic front-end detection transimpedance amplifier that includes a switched-biasing ping-pong auto-zeroed technique to decrease the input-referred noise. 3) The performance of the core amplifier is also improved using high-performance circuit techniques such as gain boosting, adaptive biasing, local common-mode feedback, and current recycling. 4) A high-precision automatic phase-alignment feedback system is designed to maximize the sensitivity of the lock-in amplifier. This feedback scheme identifies the relative phase differences between the input and the reference signals, and then automatically adjust the phase using digital and analog building blocks. Such a phase-alignment feedback module allows extremely precise phase

alignment for a very low-power and small-size budget. 5) Two on-chip photodiodes are used as optical sensors. They are implemented on the same CMOS silicon die alongside the circuits to realize a fully integrated optoelectronic sensor. 6) The lock-in sensor is used as a core module to demonstrate a point-of-care device prototype able to detect and characterize cell cultures in vitro. The extremely low-noise performance and the high-precision phase alignment feedback scheme of our design increase the device's sensitivity and allow us to characterize micro-volume samples. 7) The prototype is used in practical applications to characterize various micro-volume concentrations in vitro: i) a beads solution and ii) NIH3T3 mouse cells tagged with membrane dye. The results reveal that the proposed LIA can successfully detect different intensities of the light and deliver the corresponding DC voltages.

- **V. K. Lazarjan**, M. Crochetière, M. N. Khiarak, S. N. Hosseini, P. Marquet, B. Gosselin. " CMOS Fluorescence Cell Photometry with Ping-Pong Auto-Zeroed Lock-In Amplifier for Real-Time Biomarkers Detections." Submitted to IEEE Journal of Solid-State Circuits (JSSC 2022).

To put it in a nutshell, the first prototype was a preliminary proof of concept design that could spectrally resolve the incoming light. The tests and validation results were reported at the IEEE LSC conference. The IEEE LSC conference paper presents that the first prototype could detect light intensities from 340 nm to 850 nm. However, it could not illuminate the sample under test. Therefore, a complete prototype that could illuminate the sample and read the fluorescence signal simultaneously was designed and fabricated. This prototype was tested in multiple experiments to assess its ability to detect and quantify a sample. The performance of this prototype is fully illustrated and characterized in the IEEE Sensor Journal. The comparison with other reports showed an improvement in the precisions and power consumption. As the main goal of designing this discrete prototype, it helps us understand the required knowledge in diverse fields such as electronics, programming, data communications, data processing, optics, and biology to implement a fully autonomous fluorescence photometry system. It also familiarized us with different *in vitro* experiments that

can characterize a photometry system. Then, to decrease the size and improve the precision, the IEEE MWSCAS presents the design of an envisioned chip. This paper includes the post-layout simulation results of the proposed lock-in amplifier. The state-of-the-art table shows that the proposed techniques can improve the detection precision while it consumes a low amount of power. However, the core amplifier needs modifications to stabilize its performance for large input signals. Finally, the last chip improved the performance and the linearity of the core amplifier with circuit techniques such as adaptive biasing, gain boosting, recycling, and local common-mode feedback. In this implementation, two photodetectors were integrated into the same chip with a lock-in amplifier circuit to compact the detection unit. A fully differential front-end detection unit that utilizes a switched-biasing ping-pong auto-zeroed technique to decrease the input-referred noise was implemented. Comparing the modified ping-pong structure with chopping, the proposed front-end does not require a high bandwidth amplifier which can save power. A chopper-stabilized amplifier first transfers the signal of interest to higher frequencies before it enters the amplifier and then demodulates the signal after the amplification. Such an approach can decrease the impact of flicker noise and drastically increase SNR. This work incorporates an LIA structure that includes a modulation and demodulation process. In this work, the LIA transfers the target signal to a 1kHz frequency, considerably decreasing the flicker noise. In addition, the switched-biasing technique is utilized in this work as a reset phase, during which all transistors are off, to eliminate the flicker noise. Pushing the target signal to a higher frequency (such as 500 kHz) could potentially improve further the SNR, but it would necessitate the design of a wideband amplifier, which would increase power consumption drastically compared to this design. This work also uses automatic phase-alignment feedback to achieve the maximum sensitivity of the LIA. Two photodiodes as the optical sensors are implemented on the same die alongside the circuits to make a fully integrated optoelectronic sensor. This chip is used in a POC fluorescence photometry prototype. Experiments with a beads solution diluted in PBS demonstrate that the sensor has enough sensitivity to detect 1:100 k concentration of a sample. Experimental results obtained *in vitro* with NIH3T3 mouse cells tagged with membrane dye show the ability of the prototype to detect different densities of

cell culture. The in-depth characterization of the final POC device is presented in the second journal paper.

Chapter 3

Miniature Fiber-Spectrophotometer for Real-Time Biomarkers Detection

3.1. Résumé

Ce chapitre présente un spectrophotomètre à fibre cellulaire miniature et économique basé sur la détection d'émission de fluorescence pour la détection en temps réel de biomarqueurs. Le prototype comprend un spectromètre très sensible intégré dans un boîtier imprimé en 3D peu coûteux et une carte de circuit imprimé conçue sur mesure pour transmettre les données sans fil. Les résultats montrent que ce système portable peut identifier des échantillons de micro-volume de protéine de tubuline, un biomarqueur bien connu, pour étudier différents types de cancer. De plus, notre prototype ambulatoire est de petite taille (30 mm × 24 mm × 43 mm), léger (19 g), économique et de faible puissance (103 mW). Les résultats de mesure de spectrophotométrie de fluorescence obtenus *in vitro* pour les cellules VERO E6 colorées à l'aide du prototype présenté sont rapportés. Un ensemble d'échantillons avec des concentrations variables d'Alexa Fluor 488 ont également été testés et leurs réponses spectrales ont été mesurées dans l'intervalle de 340 à 850 nm avec une résolution de 15 nm. Les limites mesurées de quantification et de détection sont respectivement de 20 et 4 µg/mL, tandis que la sensibilité mesurée est de 85 mV/nW avec une puissance détectable minimale de 117 fW à 519 nm. Des écarts-types relatifs intra- et inter-journaliers de 1.5% et 4.7%, respectivement, ont été mesurés au cours des expériences de sensibilité longitudinale.

3.2. Abstract

This chapter presents a miniature and cost-effective cell fiber-spectrophotometer based on fluorescence emission sensing for the real-time detection of biomarkers. The prototype comprises a highly sensitive spectrometer embedded in an inexpensive 3D-printed housing and a custom-designed printed circuit board to transmit the data wirelessly. Results show that this portable system can identify micro-volume samples of tubulin protein, a well-known biomarker, to study different types of cancer. Additionally, our ambulatory prototype is small in size (30 mm × 24 mm × 43 mm), lightweight (19 g), economical, and low-power (103 mW). Fluorescence spectrophotometry measurement results obtained *in vitro* for stained VERO E6 cells using the presented prototype are reported. A set of samples with varying concentrations of Alexa Fluor 488 were also tested, and their spectral responses were measured within the range of 340–850 nm with a resolution of 15 nm. The measured limits of quantification and detection are 20 and 4 µg/mL, respectively, while the measured responsivity is 85 mV/nW with a minimum detectable power of 117 fW at 519 nm. Intra- and inter-day relative standard deviations of 1.5% and 4.7%, respectively, were measured during longitudinal sensitivity experiments.

3.3. Introduction

Fluorescence cell spectrophotometry allows physicians to identify the presence of viral or bacterial genetic materials such as RNAs or DNAs, to detect infectious diseases [1], [2], [43] or analyze and characterize a diversified set of biomarkers, such as proteins, to examine a tissue or body samples [17], [44]. Since December 2019, the pandemic of the novel coronavirus (SARS-CoV-2) has caused more than 2.4 million deaths and 110 million confirmed cases. Developing a rapid and accurate detection to quarantine the infected people can attenuate the pace of the spread. Such an isolation strategy flattens the wave peak and helps healthcare personnel to face and manage the pandemic. SARS-CoV-2 can be detected within less than 40 min by attaching a fluorophore to the RNA [1], [43]. Implementing such a method within a point-of-care (POC) device to detect SARS-CoV-2 could considerably reduce the steep rise in the number of new cases by facilitating the test procedure [2], [45]. POC devices could be instrumental in controlling the spread of many infectious diseases and recurrent large-scale epidemics, such as the Ebola virus, HIV, and SARS. Cancer, another major cause of death worldwide, can also be detected using fluorophores. Up to 11% of men are likely to develop prostate cancer, while 12.5% of women are diagnosed with breast cancer in their lifetime. In 2018 only, 2.09 million cases of lung cancers, which led to 1.76 million deaths, were reported in accordance with the world health organization [46]. The development of practical and effective tools enabling the early detection of cancer is the key to saving lives. The ability to diagnose diseases precisely by informing the tissue composition through spectrophotometry has allowed physicians to improve the treatment of cancers significantly, such as Merkel cell carcinoma (i.e., an aggressive skin cancer) [47]–[49], neuropsychiatric disorders [10], [37], [50], and cardiovascular diseases [51].

In fluorescence cell spectrophotometry measurements, human biological samples are collected and tested in a laboratory to determine the properties of biological matters [13], [50], [52], [53]. The sample transportation to the laboratory can be expensive and time-consuming and can alter the integrity of the samples [54]. Moreover, such a condition is exacerbated when multiple tests must be performed for the same patient at different time points. After

Table 3.1 Examples of Fluorophores and Applications

Fluorophore	Excitation/Emission Wavelength (nm)	Q_F*	Disease
SYTO 9	480/500	0.58	COVID-19 [1]
Malachite Green	616/665	7.9 × 10−5	COVID-19 [47]
Alexa Fluor 633	633/647	-	Breast Cancer [5]
Alexa Fluor 555	555/580	0.10	Breast Cancer [5]
DAPI	358/461	0.92	Pancreatic Cancer [6]
Rhodamine red-X	570/590	0.16	Ovarian Cancer [7]
Cy3	550/570	0.04	Prostate Cancer [8]
Alexa Fluor 488	470/519	0.92	Lung Cancer [9]

* fluorescence quantum yield

transporting the sample to the laboratory, the personnel must tag the sample with an appropriate antibody and with one or several fluorophores. A benchtop spectrophotometer is then used to analyze the samples. The collected spectrophotometry data are finally interpreted by health professionals aided by specialized software [10], [44]. Table 3.1 provides examples of fluorophores extensively used by health professionals to detect infectious diseases, such as COVID-19 [1], [43], and cancers [5]–[8], [13], [55]. Benchtop spectrophotometers are bulky and expensive devices requiring the attention of highly qualified technical staff and frequent maintenance [10], [12]. The lengthy and costly clinical evaluations associated with these benchtop spectrophotometers, the availability of samples and patients, and the need for hiring multidisciplinary groups to perform such evaluations are only some of the many problems that prevent physicians from quickly performing tests to make a diagnosis [44].

An inexpensive POC device could allow effective disease prevention, early diagnosis, accurate drug identification, and direct drug response monitoring [13], [14], by frequently monitoring the localization and the concentration of the biomarkers, including proteins [15], pathogenic nucleic acids [16], RNAs [17], DNAs [13], and creatinine [18]. Methods based on sensitivity enhancers, such as surface plasmon resonance, have shown to improve the limit of detection (LOD) for monitoring bacterial species [56] or cortisol levels in the human body [57]. Fiber specklegram, a highly sensitive and low-cost probing method, has been proven useful in structural health monitoring and biochemical parameter

assessment. Increased complexity due to the necessity for image post-processing, low-dynamic range, and high cross-sensitivity to environmental parameters are some important limitations of these methods [58]. Miniaturized cell spectrophotometers have been designed by taking advantage of inexpensive semiconductor light-emitting diodes (LEDs), MEMS, and integrated circuits technology to decrease the size, power consumption, and cost of the entire device [19]–[34]. However, these spectrophotometers are facing many challenges to providing high performance under an economy of resources. Similar to their benchtop counterpart, these spectrophotometers must allow the measurement of micro-volume concentrations of analytes across a wide wavelength range. In [19], Hong et al. introduced a fully integrated filter on a CMOS chip to decrease the size and power consumption of the spectrophotometer drastically. This device requires a wavelength gap of 400 nm between the excitation and fluorescence lights to operate properly, which confines the use of the spectrophotometer only with a small subset of fluorophores. In [37], Kim et al. designed a high-sensitivity system using a customized optical sensing probe. Adding CdSe/ZnS quantum dots to the tip of the fiber enhanced the sensing performance of the device with excellent selectivity over uric and ascorbic acids. However, the size of the probe, the weight of the entire device, and the high current drawn by the LED were substantially limiting for an ambulatory device. In [21], Khiarak et al. presented a fiber photometry sensor. Their miniaturized fluorescence sensing prototype uses an LED as an excitation light source, a customized CMOS chip, and a band-pass optical filter to block the excitation light and prevent the photodetector saturation while isolating the fluorescence light. However, this prototype cannot discriminate between different wavelengths. Additionally, the optical band-pass filter contributes to the emission fluorescence light power attenuation, thus decreasing the sensitivity of the entire device. This phenomenon was circumvented by raising the light power of the excitation LED at the cost of additional energy consumption. However, raising the light source power or the time span of exposure to increase the precision can cause photobleaching [38]. Photobleaching is a photon-induced chemical alteration that can permanently cancel the fluorescence capability of fluorophores. Depending on their chemical bonding, fluorophores can photobleach after

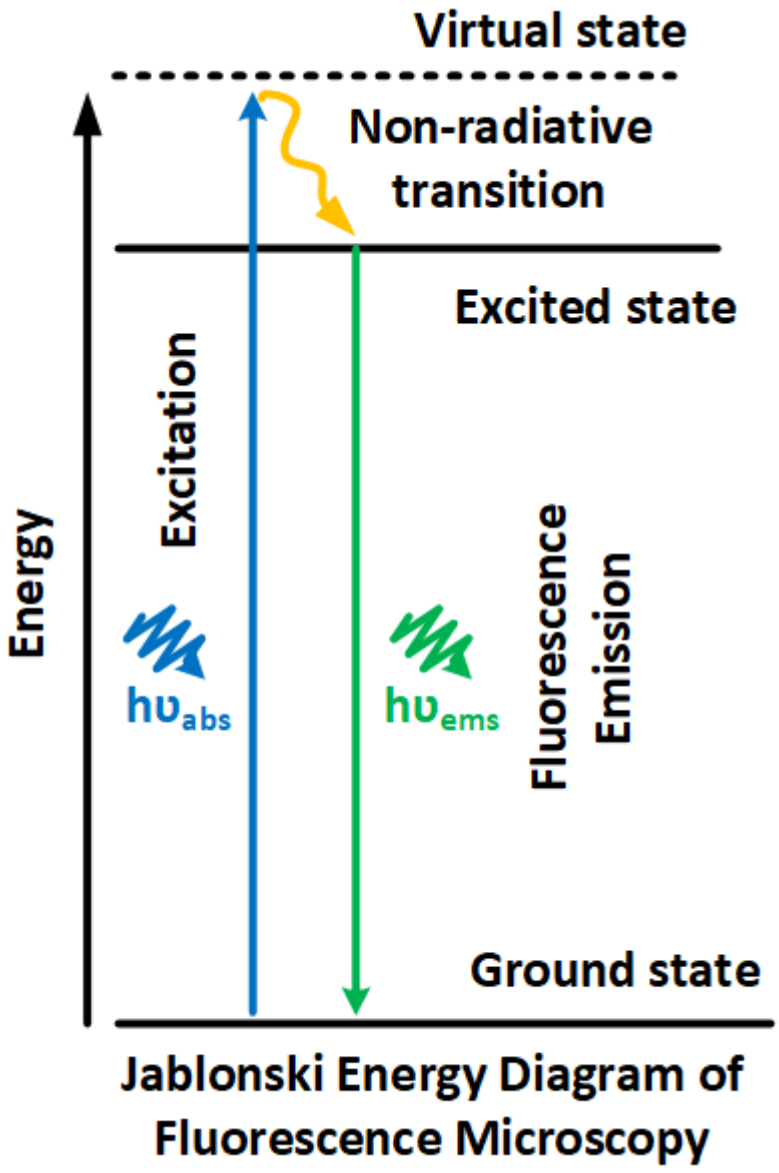

Fig. 3.1. Jablonski energy diagram illustrating the principle behind fluorescence cell spectrophotometry. A fluorophore absorbs an excitation light power of a specific wavelength and emits back emission fluorescence light at another wavelength.

absorbing only a few photons, while other molecules with improved photostability can undergo many cycles of light absorption/emission before losing their fluorescence capability. Increasing the light intensity raises the fluorophore cycling between the ground and excited states, rendering the sample under test (SUT) remarkably prone to photobleaching [9].

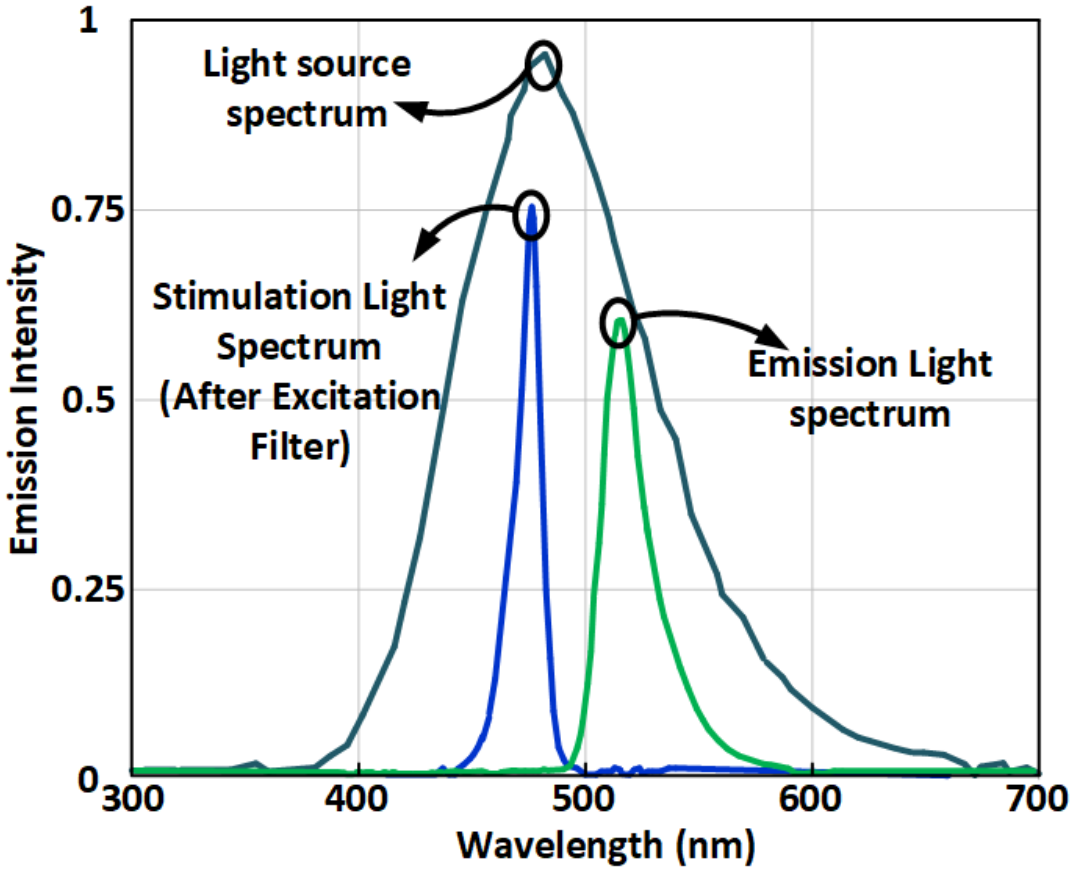

Fig. 3.2. Spectrum of the light source, stimulation light, and emission light. An excitation filter is used to remove the unwanted wavelengths from the light source.

This article presents the design of a miniaturized and wireless fluorescence cell fiber-spectrophotometer prototype toward a cost-effective and low-power POC prototype. This prototype is sufficiently sensitive for detecting micro-volume samples and fast in identifying biomarkers in real-time in an ambulatory setting. The prototype uses a simplified and compact design, replacing the emission band-pass filter of fluorescence photometry systems, the role of which is to avoid light saturation by passing only the measured fluorescence light towards the photodetector, i.e., blocking the excitation light, with a diffraction grating that separates the incoming light into multiple colors and provides a better resolution. The advantages of such an approach are demonstrated to increase the sensitivity and save excitation light source power. The proposed prototype is used to quantify various concentrations of Alexa Fluor 488 and identify tubulin protein, which is the essential constituent of innate cells, including nervous,

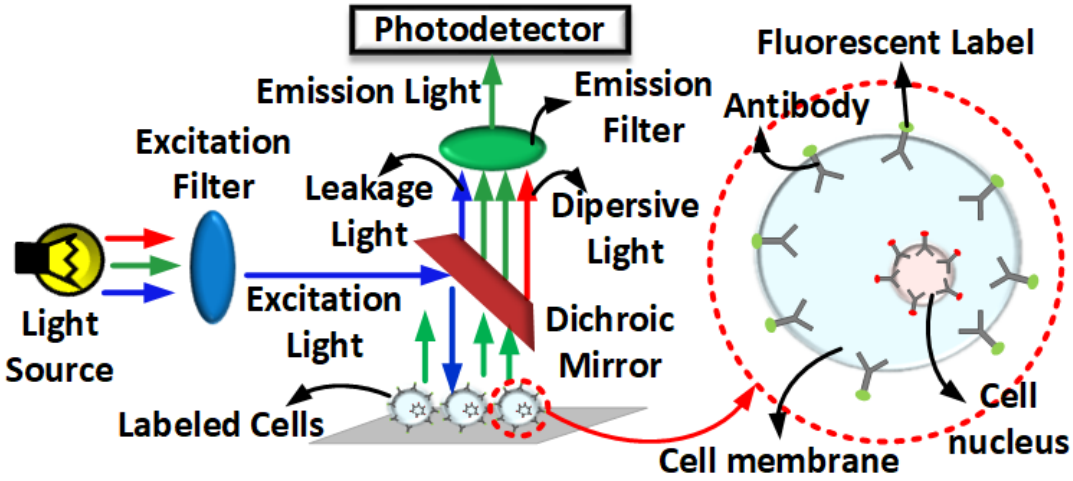

Fig. 3.3. Block diagram of fluorescence photometry with emission filter.

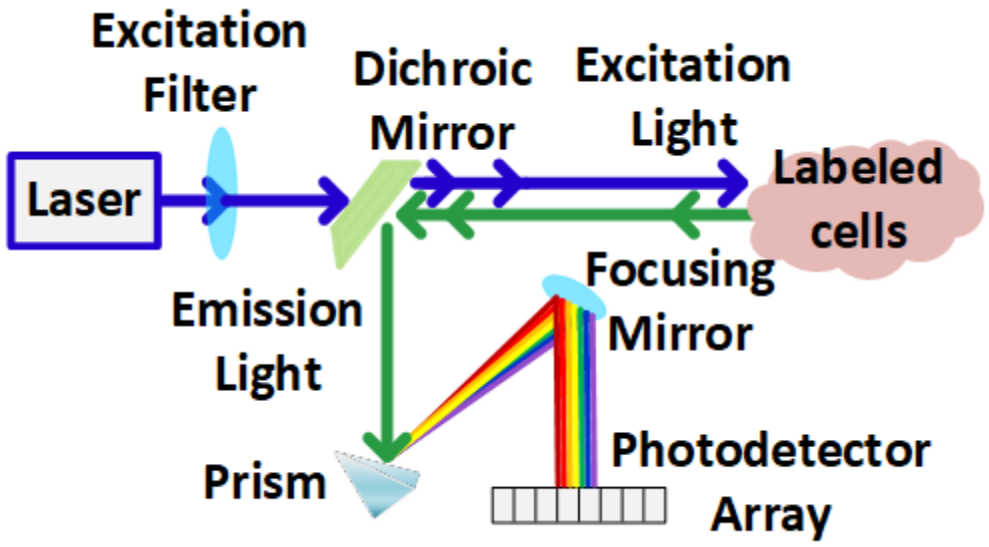

Fig. 3.4. Block diagram of a fluorescence cell spectrophotometry with a prism and photodetector array.

musculoskeletal, and blood cells, and which is also associated with different types of cancer [12], [15], [59]. The results reveal that the micro-volume concentrations of Alexa Fluor 488 are successfully detected by the presented fiber-spectrophotometer prototype. We report the measured performance and finally present the comparison with previously reported prototypes. The rest of this chapter is organized as follows. Section 3.4 summarizes the principles of fluorescence cell fiber-spectrophotometry principles. Section 3.5 provides an overview of the proposed design. Section 3.6 covers the design of the proposed

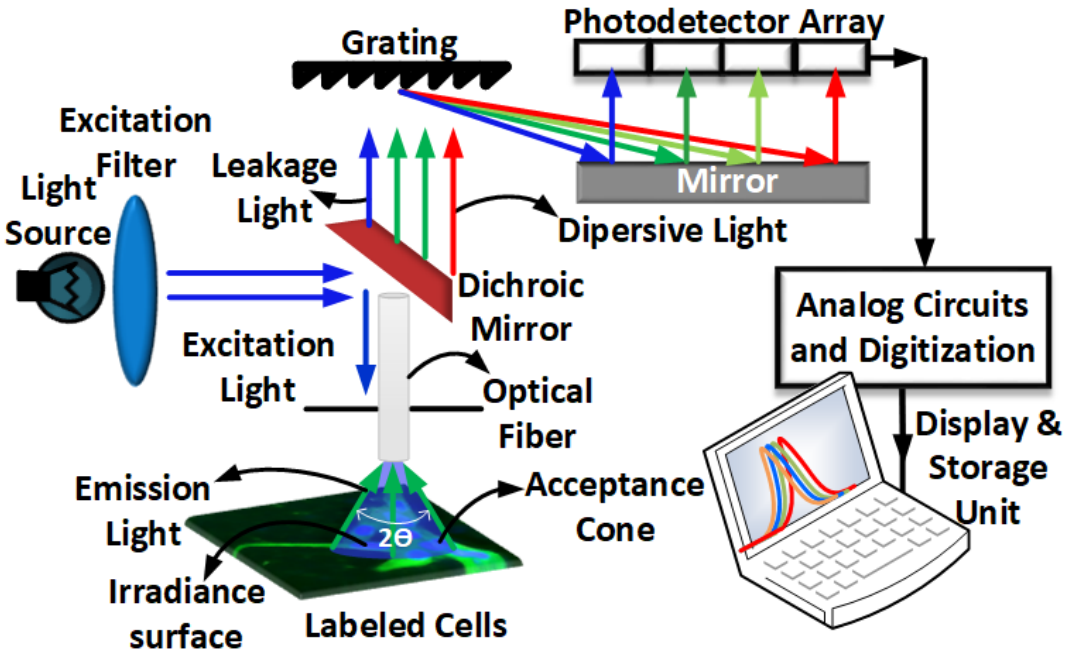

Fig. 3.5. Block diagram of a fluorescence cell fiber-spectrophotometer using a grating component. The sample cells must first be tagged with different antibodies and labels on the cells membrane and nucleus. The number of light arrows conceptually indicates the attenuation effect of each optical component on the emission light.

prototype. Section 3.7 presents the measured performance and experimental results. Section 3.8 concludes the chapter.

3.4. Principles of Fluorescence Cell Fiber-spectrophotometry

Fluorescence emission can be measured either by fluorescence photometry [21], where a single value encompassing several wavelengths is measured, or by fluorescence spectrophotometry [60], where several values are measured separately at different wavelengths. In Fig. 3.1, the Jablonski energy diagram shows the different energy states of fluorescence molecules and describes the underlying principles of fluorescence cell spectrophotometry. The fluorophores absorb light comprised within a preferred wavelength interval. This excitation light increases their energy level, from a ground state up to a virtual state (Fig. 3.1). The molecule then loses a part of the energy through a non-radiative process and falls into the excited state. The difference between the amount of excitation and emission energy leads to fluorescence light emission

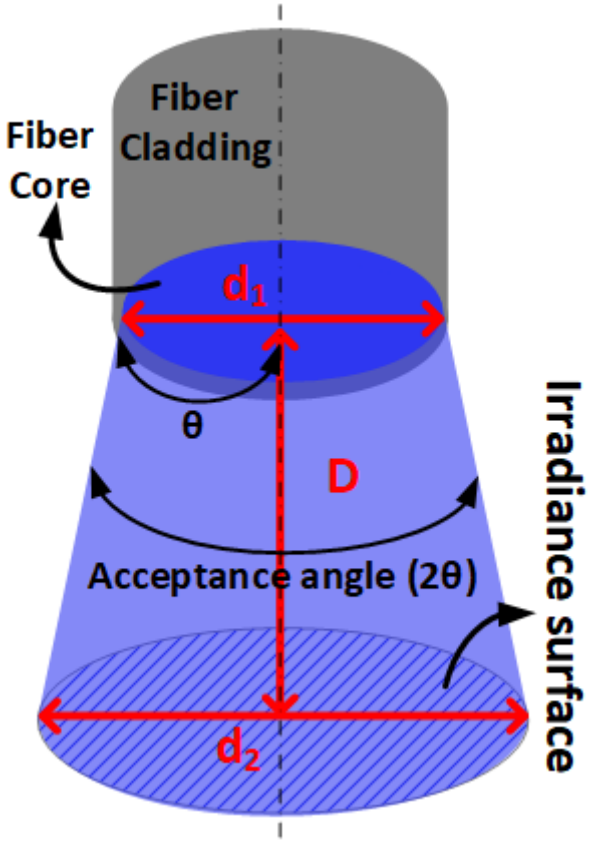

Fig. 3.6. Fiber Specifications.

at a higher wavelength than the excitation wavelength. Fig. 3.2 conceptually presents the light source and fluorescence emission light spectra. An excitation filter must be used after the light source to narrow down the delivered stimulation light spectrum and avoid overlap with the emission spectrum for proper fluorescence sensing. Particularly, utilizing such a filter in the presence of a diffuse excitation light source is crucial. The Beer–Lambert law describes the relationship between the incident excitation light (I_{ex}), the transmitted light (I_T), and the concentration (c) of analytes for a specific wavelength (λ) [61]:

$$I_T = I_{ex} \times e^{-\varepsilon_\lambda l C}, \tag{3.1}$$

where ε_λ is the molar absorption coefficient at wavelength λ, and l is the optical path length. The ratio of emission light intensity (I_{ems}) to the absorption light intensity (I_{abs}) is called the fluorescence quantum yield (Q_F):

$$Q_F = \frac{I_{ems}}{I_{abs}}. \quad (3.2)$$

Q_F depends on several factors related to the fluorophores and the experimental environment [62], [63]. The Q_F of several fluorophores is presented in Table 3.1. $I_T = I_{ex} - I_{abs}$; thus, substituting (1) in (2) shows that the fluorescence emission intensity is directly proportional to the excitation light intensity:

$$I_{ems} = I_{ex} Q_F (1 - e^{-\varepsilon_\lambda l C}), \quad (3.3)$$

which relates the emission light intensity to the concentration of the SUT based on the Beer–Lambert law.

As shown in Fig. 3.3, a fluorescent dye binds to target molecules in the cell, allowing monitoring of important characteristics and cell activities. Labeling cells with a fluorescent dye requires a primary antibody that binds to the target molecule and acts as an intermediate compound between the target molecule and the fluorescent dye.

Fig. 3.3 shows that an emission filter used before the sensor to pass the fluorescence emission and block any out-of-band light wavelengths can attenuate the fluorescence emission light power and decrease the resolution of a fluorescence photometry system. By contrast, a fluorescence cell spectrophotometer uses a prism or a grating to separate the fluorescence emission into several colors and measures the intensity at each wavelength using a photodetector array. Thus, fluorescence spectrophotometry can assess a sample using a collection of data rather than only a single value [60], [64].

The simplified block diagram of fluorescence cell spectrophotometry is shown in Fig. 3.4. Such a system includes the following: 1) an excitation light source, such as a laser, to elicit fluorescence from a sample; 2) excitation/emission optical filters to pass the light and retrieve the spectrum of the fluorescence emission; 3) a prism or a grating to diffract the fluorescence emission light into different colors; 4) a dichroic mirror to pass or block specific wavelength spectrum; 5) a photodetector array and photomultipliers to detect, amplify, and convert the fluorescence signal into an electrical signal. The SUT is illuminated

by the excitation light source, and the fluorescence emission light is then collected and processed by the optical components and the photodetector.

An optical fiber is often used to deliver the excitation light to the fluorophores and collect the fluorescence signal locally, especially when a diffuse excitation light source (e.g., an LED) is used (Fig. 3.5) [21], [31], [38]. The divergence of the excitation light beam emerging from the optical fiber depends on the core size and the numerical aperture (NA) of the fiber [9]. As shown in Fig. 3.6, the fiber has a cone of acceptance defined by the NA of the fiber. The light falling inside the acceptance angle is guided into the core–cladding interface, while that falling outside the acceptance cone is refracted out of the core. A large NA improves the collection of additional light power by the fiber. Assuming the medium between the fiber and SUT is air, the NA can be calculated as follows:

$$NA = sin(\theta) = \sqrt{n_{core}^2 - n_{clad}^2}, \tag{3.4}$$

where θ represents half of the acceptance angle, and n_{core} and n_{clad} are the fiber core and cladding refractive indexes, respectively. Given the acceptance angle of the fiber, changing the distance (D) between the tip of the fiber and the target area varies the illuminated area. This variation can be calculated as follows:

$$D = (d_2 - d_1)\frac{cos(\theta)}{2 \times NA}, \tag{3.5}$$

where d_1 and d_2 are the diameters of the fiber core and the illuminated surface, respectively. Conversely, decreasing the distance between the tip and the sample reduces the surface irradiance when exiting the sample but increases the radiant flux, namely the light power. Increasing the distance between the tip and the SUT raises the irradiance surface but decreases the radiant flux, which can result in detection error due to the minimal fluorescence power captured by the fiber [65], [66]. Therefore, (5) presents the optimal distance between the

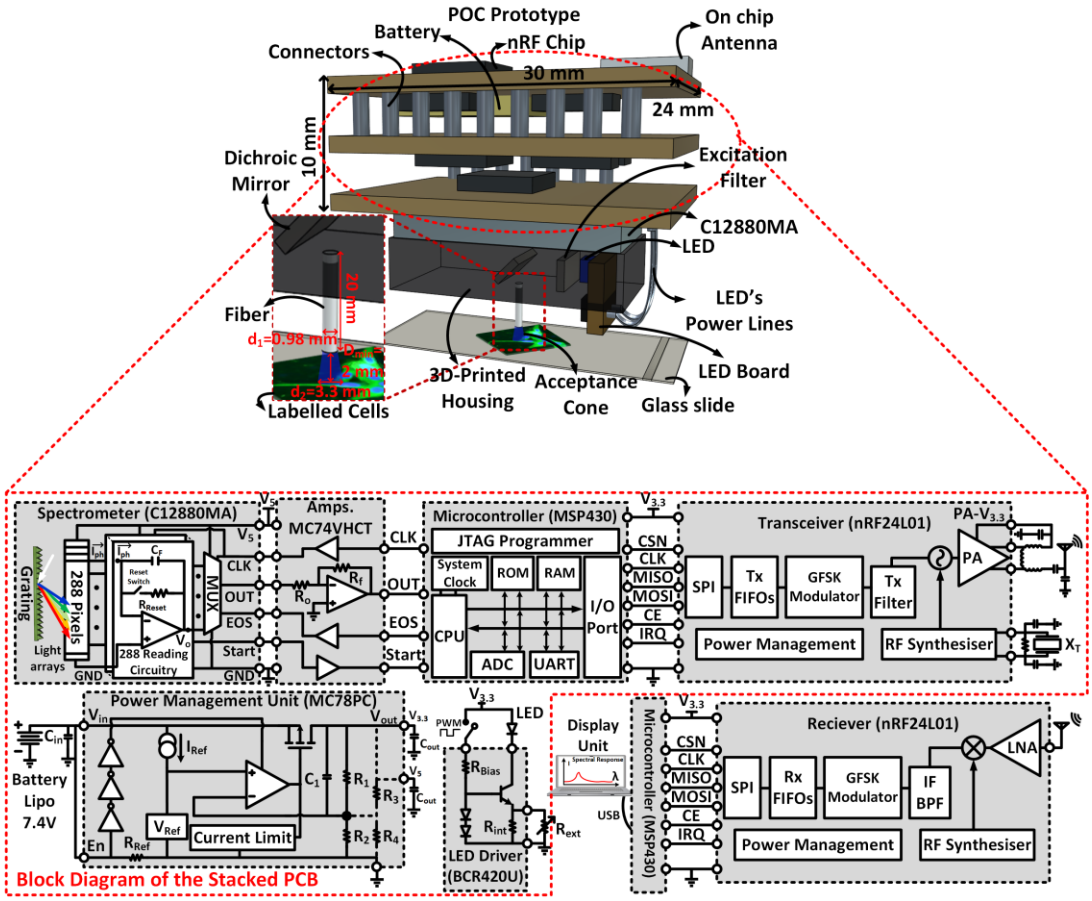

Fig. 3.7. Representation and block diagram of the presented wireless miniaturized cell fiber-spectrophotometer. The 3D representation of the prototype shows the photodetector, wherein the optical fiber is enclosed in a lightweight 3D-printed housing. On the right-hand side, the block diagram presents each part of the prototype, their interconnections, and interfaces. On the left-hand side, the graphical image presents all optical and electrical components of the prototype.

sample and the tip of the fiber to analyze a given sample area using a fiber-spectrophotometer of a given NA.

3.5. System Overview

Fig. 3.7 shows the block diagram of the miniature cell fiber-spectrophotometer prototype. The device uses a blue LUXEON Rebel LED from Lumileds (San Jose, CA, USA) as the excitation light source. The LED is controlled by an LED driver circuit and mounted on a small electronic board embedded inside a lightweight 3D-printed plastic housing. The diffuse excitation light is first passed

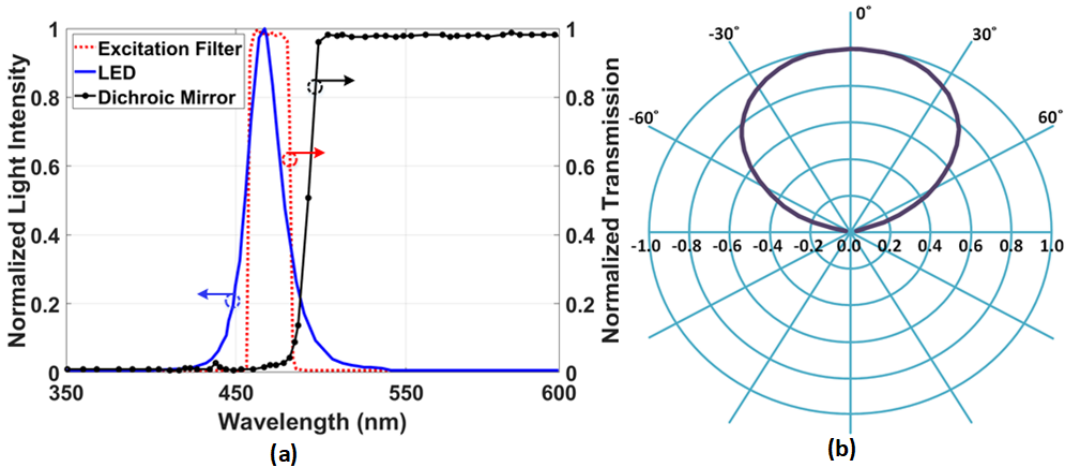

Fig. 3.8. Prototype uses a Blue LUXEON Rebel LED as excitation light source. (a) The spectrum of the LED ranges from 425 nm to 525 nm and a peak at 470 nm (blue line), the theoretical response of the excitation filter ranges from 458 nm to 482 nm (dash line), and the response of the dichroic mirror with a cut-off wavelength of 495 nm. (b) Polar radiation pattern of the LED (right-hand side).

through an optical band-pass filter between 458 and 482 nm (ET470/24m, Chroma Technology, Bellows Falls, VT, USA) to narrow the excitation spectrum. A dichroic mirror blocks the excitation light below 495 nm. Thus, only the fluorescence emission light can pass through the dichroic mirror and reach The spectrometer. This filter, called the excitation filter, collimates the blue light toward the dichroic mirror and narrows the excitation light spectrum. The transmission/blocking response of the excitation filter is shown in Fig. 3.8 (a). The dichroic mirror (Fig. 3.8 (a)), which is a long-pass filter with a cut-off wavelength of 495 nm (495L pxr, Chroma Technology, Bellows Falls, VT, USA), deflects the excitation light source into a multimode fiber (SN 02-534, Edmund Optics, Barrington, NJ, Canada). Using an optical fiber allows the delivery of the excitation light to micro-volume samples and the effective retrieval of the fluorescence signal locally from these samples. A 1 mm diameter and 20 mm length plastic fiber with a core diameter of 980 µm and an attenuation factor of 0.15 dB/m is used in this design. The n_{core} and n_{clad} of the multimode fiber are 1.492 and 1.402, respectively. The fiber has an NA of 0.51 with a tolerance of ±0.03, which corresponds to an acceptance angle of 61°. Such an angle enhances the light source coupling into the fiber and increases the fluorescence

Table 3.2 Fiber specifications

Parameter	Value
Length	20 mm
Outer diameter	1 mm
Core diameter (d_1)	980 µm
ncore	1.492
nclad	1.402
NA	0.51
NA tolerance	±0.03
Acceptance angle	61°
Attenuation	0.15 dB/m
Core material	Polymethyl Methacrylate Resin
Cladding material	Fluorinated Polymer
Operating Temperature	-55 to +70 °C
D	2 mm
Irradiance surface	d_2: 3.3 mm, area: 8.8 mm^2

emission retrieval capability of the system. The fluorescence light of the SUT entering the fiber at a lower angle than 61° is guided toward the spectrometer [9]. A distance of D = 2 mm is recommended with the presented prototype, which corresponds to a target area of around 8.8 mm^2. The blue excitation light passes through the fiber, reaches the SUT, illuminates the target area, and stimulates the tagged cells. Once exposed to sufficient blue light intensity, the stimulated tagged cells emit fluorescence light, which is retrieved by the same fiber, and passed to the spectrometer through the long-pass filter. The dichroic mirror is transparent at the wavelength of the emitted fluorescence light. Therefore, the fluorescence light passes through the mirror and the spectrometer slit, hits the grating, and reaches the photodetector array inside the mini-spectrometer (C12880MA, Hamamatsu Photonics, Shizuoka, Japan). After reaching the grating surface, the fluorescence light diffracts into several colors, each having different angles, reaching the photodetector array at a specific pixel. The photodiode converts the incoming fluorescence light into an electrical current (I_{ph}), which is then converted to an output voltage (V_o) by the reading circuit inside the C12880MA (Fig. 3.7). Vo can be calculated as follows:

$$V_O = \frac{1}{C_F} \times I_{ph} \times t_i, \tag{3.6}$$

where t_i is the integration time of the reading circuit to charge the capacitor CF with the photodiode current (I_{ph}). The reading circuit can deliver a valid output

Table 3.3 Prototype characteristic

Parameter	Value
Wavelength range	340–850 nm
Resolution	15 nm
Minimum exposure time of LED	1.88 ms
Conversion gain (CG)	50 μV/e^-
Total weight	19 g
Size	30 mm × 24 mm × 43 mm
Center radio frequency	2.4 GHz
Radio link nominal data rate	2 Mbps
Communication range	10 m
Sampling frequency	2 MHz
Spectrum refresh rate	525 Hz
Microcontroller clock frequency	8 MHz
Number of bits	12

after one integration time t_i, which defines the minimum exposure time of the sample to the excitation light of the LED. The value of t_i can be adjusted by changing the clock frequency of the spectrometer, which is recommended to be in the range of 0.2 to 5 MHz by the manufacturer. The clock signal of the spectrometer frequency is set to 200 kHz in this design, which corresponds to t_i = 435 μs. The output of the photodetector array corresponds to a discrete-time sequence of discrete voltages, the amplitude of which corresponds to the detected light intensities of each wavelength. Each discrete voltage has a time duration of 5 μs.

Analog circuits, namely buffers and amplifiers, are then used to adjust the analog output voltages of the C12880MA spectrometer and transfer them to an ADC inside a microcontroller for digitization. The microcontroller samples and digitizes the data on 12 bits. The recorded data are then transmitted to a base station located 10 m away from the prototype using a 2.4 GHz industrial, scientific, and medical (ISM) radio module. The prototype is supplied by a small lithium-ion rechargeable battery and a power management unit mounted on a stack of printed circuit boards (PCBs). The proposed prototype employs three PCBs (Fig. 3.7) to perform signal amplification, digitization, and communications. The PCBs are stacked on top of each other using rigid connectors to decrease the size of the entire device. The size of the stacked PCB is 30 mm × 24 mm × 10 mm, as shown in Fig. 3.7. Finally, a MATLAB user

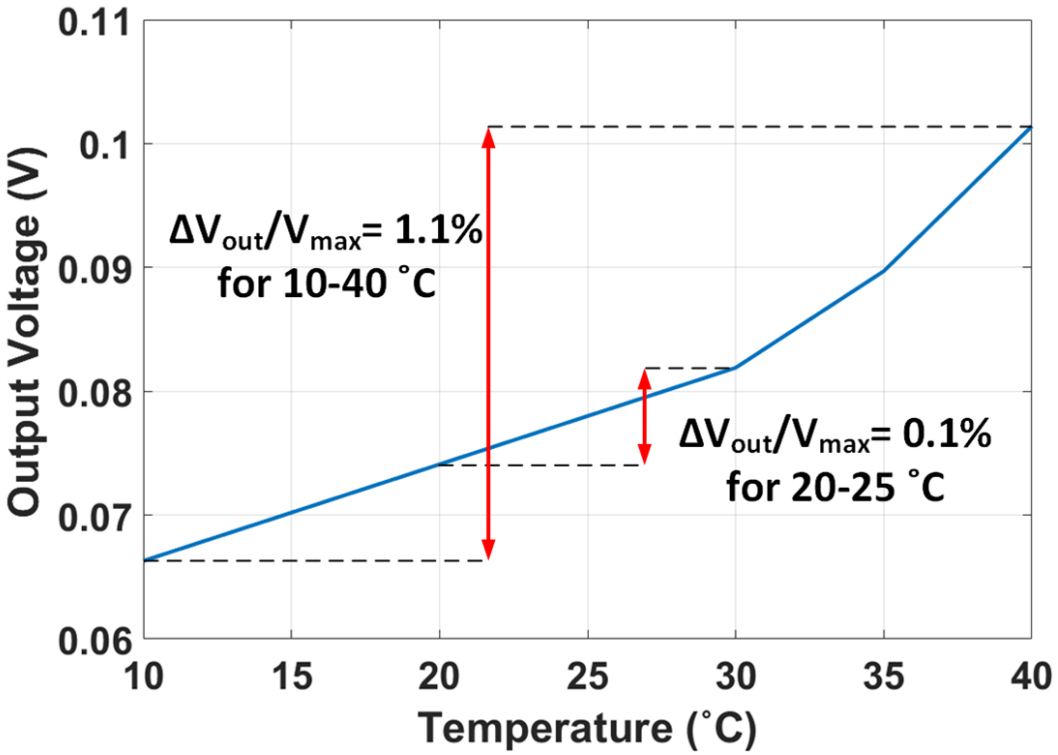

Fig. 3.9. Measured output voltage versus temperature for the whole prototype. The output varies by only 1.1% across a 30° temperature variation.

interface allows visualization of the spectral response of the retrieved fluorescence light. This spectral response is normalized in amplitude over the

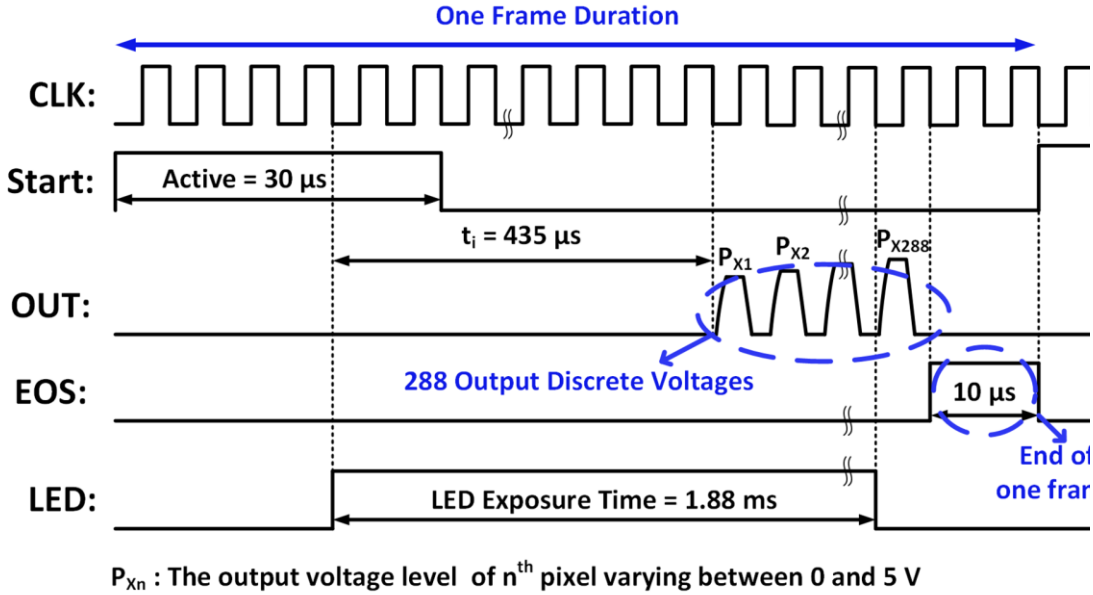

Fig. 3.10. Timing diagram of the spectrophotometer prototype.

wavelength range of 340 nm to 850 nm. These characteristics of the prototype are summarized in Table 3.3 and explained in the next section.

A photodetector along with a light-blocking filter is often conducted in fluorescence photometry systems to pass the fluorescence light and block the excitation light [21], [38]. In this design, a photodetector array combined with a diffraction grating inside the C12880MA is used. Using a mini-spectrometer similar to the C12880MA has many important advantages over the other fluorescence photometry solutions. 1) It avoids the utilization of a filter inside the emission light path to allow additional emission light power to reach the photodetector, which can improve the sensitivity of the entire prototype. The experimental results show an increase in sensitivity by a factor of 3 using this scenario compared with other solutions. 2) It decreases the concentration prediction error by measuring the entire spectrum instead of a narrow wavelength band only. In fact, the capability to detect a wide wavelength range around the peak wavelength value without saturating the sensor improves the sensitivity of the entire system by minimizing the prediction error. This improvement of the sensitivity allows the identification and the quantification of micro-volume concentrations of analytes. 3) The prototype can quantify a wide range of different concentrations within an extended linear range, with a high correlation coefficient square (R^2) between the analyte concentrations and the measured light emission intensities. 4) A low-power LED can be used to illuminate the analytes with the same performance. 5) The same device can be used with different excitation light source colors to identify multiple types of fluorophores of different wavelength bands, which provides flexibility and high selectivity.

3.6. System Design

3.6.1. Spectrometer and Excitation LED

A blue LUXEON Rebel LED, which has a spectrum range from 425 nm to 525 nm and a peak at 470 nm (Fig. 3.8 (a)), is used as the excitation light source. This LED has a narrow polar radiation pattern (Fig. 3.8 (b)) that increases the fiber coupling efficiency by directing most of the light power toward the dichroic mirror and the fiber. The prototype is efficient when an increased amount of LED light reaches the SUT. The fluorescence light emitted by the SUT is

collected by the multimode optical fiber. The optical fiber characteristics are summarized in Table 3.2. The fiber uses polymethyl methacrylate, one of the most used materials in plastic optical fibers [67]. Plastic fibers have several advantages over silica fibers, such as a high thermos-optic coefficient, which increases the stability of the measurements [68]. The fluorescence light passes through a dichroic mirror after the fiber and enters the narrow input slit of the C12880MA spectrometer before reaching the diffraction grating surface. The slit aperture size of the sensor is 50 µm × 500 µm with an NA of 0.22. The spectrometer comprises a diffraction grating and a photodetector array sealed by an opaque hermetic package to increase the reliability of the sensor output across varying humidity conditions, and to block any ambient light. All the presented results were obtained at room temperature and at standard indoor relative humidity. Fig. 3.9 shows the effect of the temperature on the measured performance of the prototype, while it was placed inside an environmental chamber (T10RC from Thermal Product Solutions), and the data were transmitted wirelessly to the base station. As can be seen, the output voltage variation of the spectrometer prototype was of only 0.1% for a temperature variation range of 20°C to 30°C. The output voltage of the spectrometer prototype changed by 1.1% when the temperature varied from 10°C to 40°C. The grating component diffracts the incoming light into its several constitutive wavelengths. The diffracted light reaches the photodetector array, which includes 288 pixels, each having a size of 14 µm × 200 µm. The photodetector array can detect the spectral response of the incident light from 340 nm to 850 nm with a resolution of 15 nm. Such a high resolution and a broad wavelength detection range are suitable for detecting most fluorophores. The spectrometer has an offset voltage of 0.5 V and a pixel conversion gain (CG) of 50 µV/e^-, which represents the electrical responsivity of the photodetector circuits considering the energy of the incoming photons. The minimum SUT exposure time to the LED excitation light is 1.88 ms to allow sufficient time for the spectrometer to retrieve the entire spectrum data. The dimensions of the entire spectrometer unit are 20.1 mm × 12.5 mm × 10.1 mm, and the weight is 5 g, which makes it suitable for utilization into an ambulatory device [69]–[71].

3.6.2. Microcontroller Unit and Wireless Transceiver

A low-power microcontroller of the MSP430 family from Texas Instruments (Dallas, TX, USA) is used to provide the control and clock signals of the spectrometer. A surface-mounted crystal oscillator (NX2520SA-16MHZ-STD-CSW-4, from NDK America Inc.) is used to set the operating frequency. The successive-approximation-register analog-to-digital converter (ADC) of the microcontroller is used to sample the output analog signal of the spectrometer and convert it into a 12-bit digital data sample with a sampling frequency of 2 MHz. The data are sent on the serial peripheral interface (SPI) bus to the radio module (NRF24L01, Nordic Semiconductors, Trondheim, Norway) and then wirelessly transmitted to a base station.

The microcontroller uses an operating frequency of 8 MHz. Fig. 3.7 presents the connections between the microcontroller and the spectrometer, including signals OUT, CLK, end-of-scan (EOS), and Start, and the description is presented as follows. Fig. 3.10 shows a timing diagram of the main input and output signals of the spectrometer. The spectrometer delivers an output sequence of 288 discrete analog voltages in series, each corresponding to the output of one pixel of the array (PX_1 to PX_{288}) varying between 0 and 5 V. A 200 kHz internal clock signal is used to determine the period of validity of each discrete output voltage. The occurrence of the EOS binary code indicates the end of each output frame, which includes 288 discrete voltages. Each frame of discrete values corresponds to a complete spectrum, including the amplitudes of all 288 wavelength bins between 340 to 850 nm. The Start signal, which remains active for six clock cycles, commands the spectrometer to start a new round of readings after each completed frame. The spectrometer then starts to accumulate the incoming light and prepare the valid output data. This integration time (t_i) requires 87 clock cycles, which takes 435 µs. Each 288 discrete voltage frame, which represents one spectral response within a time interval of 1.44 ms, takes 288 clock cycles to generate. Generating and acquiring a complete spectrum frame of 288 discrete voltages takes 381 clock cycles. Each reading from the photodetector array takes 1.905 ms. Therefore, the spectrum refresh rate is 525 Hz. Using multiple reading circuitries after 288 photodiodes, as shown in Fig. 3.7, allows parallel readout and improves the

spectrum refresh rate. The LED needs to be activated between the 4th clock cycle of the Start signal and the beginning of the last pixel reading time, which takes 376 clock cycles. Thus, the LED must be activated for a minimum time of 1.88 ms, which is called the minimum exposure time, to record a complete spectrum sequence. Continuously generating and processing spectrum data sequences using the prototype provides live and real-time monitoring of the SUT spectral response. The NRF24L01 integrated radio transceiver from Nordic Semiconductors and a chip antenna (ANT-2.45-CHP-T) from Linx Technologies Inc. (Merlin, OR, USA) are used to transmit the spectral data to a remote Internet gateway. The radio module operates at a 2.4 GHz center frequency within an ISM band. The 8 MHz SPI bus of the microcontroller passes control and configuration data to the transceiver. The maximum transmission rate in air is 2 Mbps, within 10 m from the base station. The ultra-low-power feature of this radio transceiver and the small quad-flat no-leads 4 × 4 mm package allow for a compact PCB and an optimized design.

3.6.3. Power Management Unit and LED Driver

Fig. 3.7 presents the block diagram and circuit schematic of the power management unit. Two 3.7 V, 100 mAh, and 2.1 g lithium-ion batteries, which have a lifespan of three years or 500 charge cycles, supply the energy to the entire device, providing a lifetime of 14 h. Two low-dropout voltage regulators (MC78PC Series from ON Semiconductor, Phoenix, Arizona, USA) are used to generate two supply voltages: a 5 V (V_5) supply voltage is used to power up the C12880MA spectrometer, and a 3.3 V ($V_{3.3}$) supply voltage is used to power up the LED driver, the microcontroller, and the radio module. These high-precision regulators present a high ripple rejection ratio (70 dB at 1 kHz), which attenuates any artifact and improves the measurement accuracy. Each regulator occupies only 2 mm × 2.5 mm.

The LED driver uses the BCR420U from Diodes Incorporated (Plano, TX, USA), as shown in Fig. 3.7. This driver provides the current to activate the excitation light source LED. The LED driver operates as a constant current regulator to drive the LED linearly. The two integrated diodes in this design provide a constant voltage to the internal resistor (R_{int}), typically 95 Ω. The BJT transistor is turned on when the supply voltage $V_{3.3}$ is above 1.4 V, and the constant

voltage across R_{int} provides a constant collector current. Any variation of the supply voltage cannot affect the voltage across R_{int} because it is fixed by internal integrated diodes. The current of the LED driver is set by adjusting the value of an external resistor (R_{ext}). A 10 kΩ potentiometer, which is used to implement R_{ext}, is placed in parallel with the R_{int} of the LED driver. Therefore, the LED forward current and the output power can be adjusted by varying the value of R_{ext}. The LED driver can provide a minimum current of 5 mA and support a maximum current of 350 mA. As mentioned above, the minimum SUT exposure time to the LED excitation light is 1.88 ms to meet the spectrometer requirement of t_i. The supply voltage of the LED driver is controlled by a switch located above R_{bias} in the circuit schematic, and a pulse-width modulated signal generated by the microcontroller at a maximum frequency of 25 kHz, and used to dim the LED.

3.6.4. Base station, Firmware, and User Interface

The base station includes an NRF24L01 receiver module controlled by an MSP430 microcontroller and is connected to an Internet gateway, such as a Raspberry Pi, or a computer host in this case, through a USB port. The base station collects and displays the spectral responses and stores the data inside the local memory or in the cloud. The stored data, which is called a raw spectral response, correspond to the multiple spectral responses emitted from the same SUT at different time intervals. After storing the data, different data processing steps are applied to the raw spectral response to assess the linearity and sensitivity of the prototype. First, the saved multiple spectral responses that correspond to the same experiment are averaged to minimize the errors. Afterward, the DC offset level, which is caused by the spectrometer and the signal conditioning circuitry, is removed from the averaged spectral response, and the results are normalized between 0 and 1 to eliminate the data redundancy and facilitate the data analysis. These steps can be performed in MATLAB, which runs on the host computer, to improve the quality of data. Different criteria are then calculated to assess the performance of the prototype [72].

Table 3.4 Summary of Measured Performance

Parameter	Value
Power consumption	
Microcontroller and data transceiver	31 mW
Analog interface circuits	2 mW
Photodetector	55 mW
LED and driver circuits	15 mW
Total power consumption	103 mW
Autonomy	14 h
LED output optical power	2.9 mW
Output optical power intensity (@ D)	8.37 µW/cm^2
Minimum detectable power (P_{min}) @ 519 nm	117 fW
Responsivity @ 519 nm	85 mV/nW

3.6.5. 3D-printed Housing

A lightweight 3D-printed plastic housing holds together all the necessary passive optical components such as the optical fiber, the excitation filter, the dichroic mirror, and the LED. All components are enclosed inside the 3D-printed housing, which comprises a photopolymer black resin from Formlabs (Somerville, MA, US), to prevent unwanted light deflection and leakage into the spectrometer. The details associated with the fabrication of the 3D-printed housing are provided in [21]. The plastic cover contains a hole at the bottom for holding the fiber used for transferring/retrieving the excitation and fluorescence

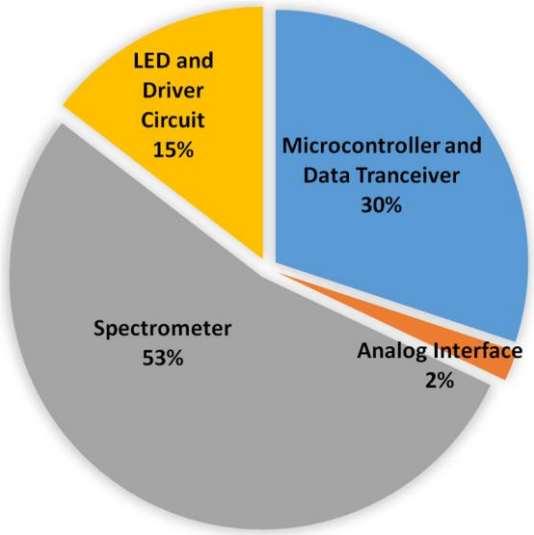

Fig. 3.11. Power consumption breakdown of the prototype. The total power consumption is of 103 mW.

light, and three other cavities are connected together through narrow tunnels to implement the optical paths of the incident and reflected lights. These cavities hold the LED, the LED driver, the dichroic mirror, and the excitation filter and require careful design to guide the light toward the fiber or the sensor with high efficiency [21].

3.7. Experimental Results and Discussion

3.7.1. Measured Performance

Table 3.4 summarizes the measured performance of the fiber-spectrophotometer prototype. The total electrical power consumption of the prototype is 103 mW, from which only 2 mW is consumed by the analog interface circuits, while 31 mW is used for digitization, control, and wireless data transmission. The LED consumes 15 mW to excite the sample, while the C12880MA spectrometer and associated circuits consume 55 mW. Fig. 3.11 shows the breakdown of the total power consumption of the presented prototype, which is less than that of other ambulatory cell spectrophotometer prototypes [17], [21], [28], [31]. An optical power meter (PM100D) and a slim photodiode power sensor (S130C), which are both obtained from Thorlabs (Newton, NJ, USA), were used to determine the light intensity and output power of the LED. The optical power meter was adjusted to measure the light power at the wavelength of 470 nm and calibrated in a dark room prior to the measurements. A light power of 2.9 mW was measured when the LED was placed tangential to the optical power meter and supplied with a nominal forward current of 5 mA. This power was experimentally deemed appropriate to excite fluorophores through the fiber at a distance of D = 2 mm, as demonstrated in the following sections. The output light intensity of the LED was adjusted by changing the value of R_{ext} (Fig. 3.7) through a potentiometer mounted on the prototype electronic board. Fig. 3.12 presents the output irradiance at the tip of the fiber, for D = 2 mm, against the LED current. The nominal output light power at the tip of the fiber for a forward current of 5 mA was 9 µW, which provides an intensity (or irradiance) of 10 µW/cm^2, corresponding to an attenuation of 25 dB compared with the direct LED output

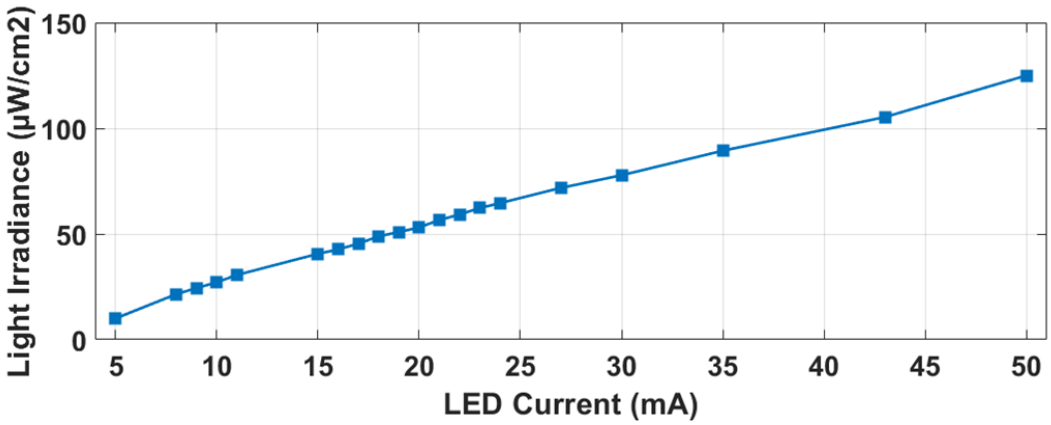

Fig. 3.12. Light irradiance at the tip of the fiber versus the LED current.

power. This attenuation is caused in part by the excitation filter, which narrows down the excitation light bandwidth before its entry to the fiber. The coupling of the filtered light source into the fiber and the fiber loss also cause attenuation. The fiber presents a 0.15 dB/m loss, which causes a slight attenuation of 3 mdB in a 20 mm length fiber. The irradiance of the excitation light at the recommended distance from the tip of the fiber (D = 2 mm) was 8.37 µW/cm^2. For comparison, an output light power of 30 µW was used in [21] to excite 2.5 µg of cholera toxin-subunit B conjugated with Alexa Fluor 488, a fluorophore utilized to detect different types of cancer cells. Thanks to a higher responsivity in the presented prototype, using a lower nominal output light power of 9 µW contributes to increasing the battery life. Fig. 3.13 shows the output voltage of the spectrometer with respect to the incident light power at the tip of the fiber, which is measured with the above-mentioned optical power meter and the slim photodiode power sensor. To derive the responsivity of the prototype at different wavelengths, blue and green LEDs are utilized as light sources because they contain emission peaks at 461 and 519 nm, which correspond to DAPI and Alexa Flour 488 center emission wavelengths, respectively. After illuminating the fiber's tip with each LED and measuring the corresponding output voltages, the ratio of output voltage over the measured light power for each wavelength provides the responsivity of the prototype. As can be seen in Fig. 3.13, the prototype presents responsivities of 85 and 90 mV/nW at 519 and 461 nm, respectively, which are three times higher than other ambulatory prototypes using an emission filter in front of the photodetector [21].

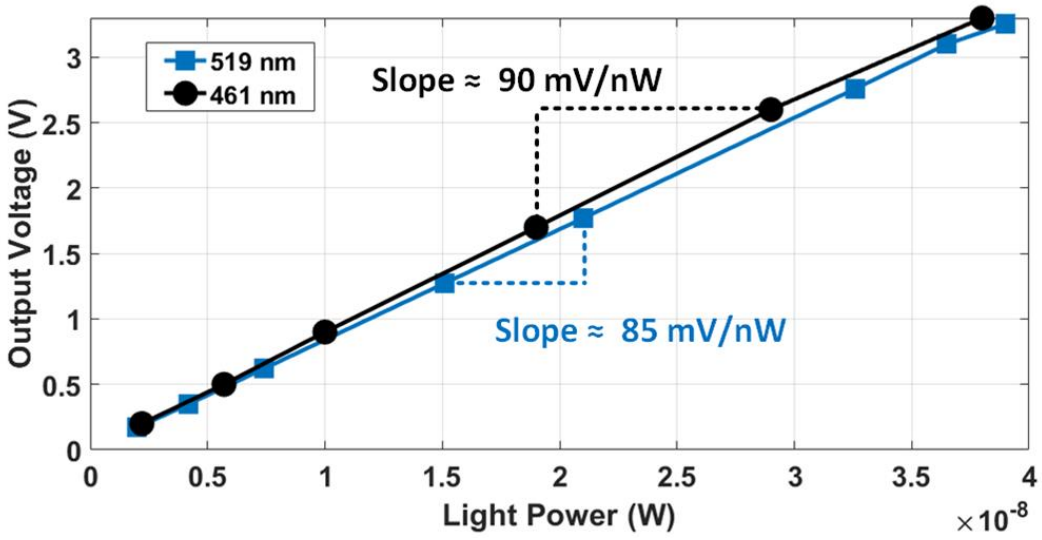

Fig. 3.13. Measured Responsivity (R): the measured output voltage against the input incident light power at the tip of the fiber, at 461 nm and 519 nm, the center emission wavelengths of DAPI and Alexa Fluor 488, respectively, which are two fluorophores used to validate the presented prototype *in vitro*.

To derive the noise performance of the prototype, the output voltage is first recorded in the dark (without input light) with an oscilloscope. The output noise voltage of each pixel is then measured by dividing the recorded output noise voltage into 288 sections, each of which corresponds to the response of a photodiode. The 288 sections of the output noise voltage provide the noise density for the prototype wavelength range, as shown in Fig. 3.14. The noise equivalent power (NEP) of a photodetector represents the minimum detectable power (P_{min}) produced by a signal, which has a power equal to that of noise [73]. Eq. 3.7 shows the relation between the output noise (V_n) and P_{min}.

Table 3.5 Summary of the prototype cost*

PARAMETER	Value
C12880MA Spectrometer	$245
Off-the-shelf electronic components	$15
Battery	$5
Printed circuit board fabrication	$5
Optical components (fiber, mirror, etc.)	$10
3D-printed Housing	$5

*The cost is in US dollars.

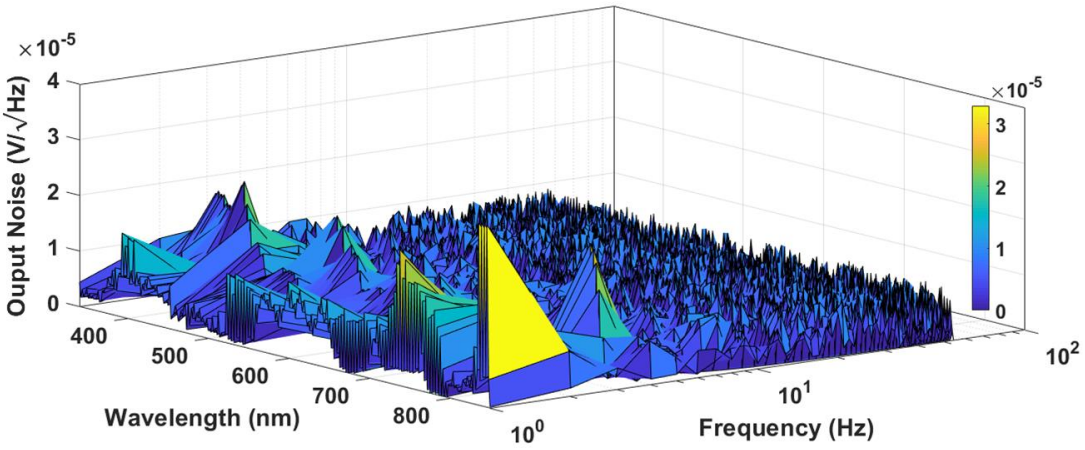

Fig. 3.14. Measured output noise voltage (V_n) for a dark input at different wavelengths.

$$P_{min}(\lambda) = \frac{v_n}{CG \times R(\lambda)} \times \sqrt{BW}, \tag{3.7}$$

where *BW* is the measurement bandwidth, *R(λ)* is the responsivity of the photodiode at a specific wavelength, and *CG* is the conversion gain. The spectrometer has the following parameter values: *CG* = 50 μV/e^- and R(600 nm) = 4.5 × 10^{16} counts/sec·W, and a minimum detectable power of P_{min} = 50 fW at 600 nm [74]. However, the sensitivity experiments of the prototype were performed at the peak frequency of 519 nm, which is the center emission wavelength of Alexa Fluor 488. Therefore, the P_{min} is measured at 519 nm to assess the sensitivity performance of the prototype. The output noise at 519

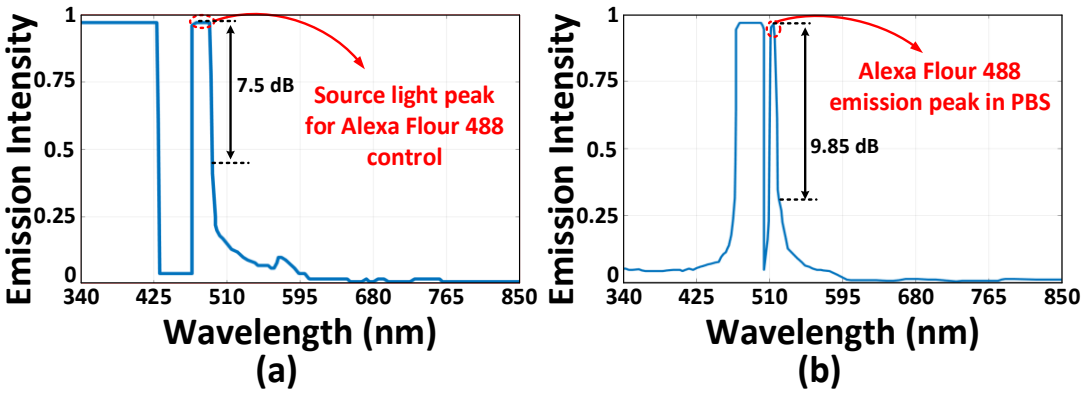

Fig. 3.15. (a) Spectral response of Control Alexa Fluor 488 (b) Spectral response of Control DAPI.

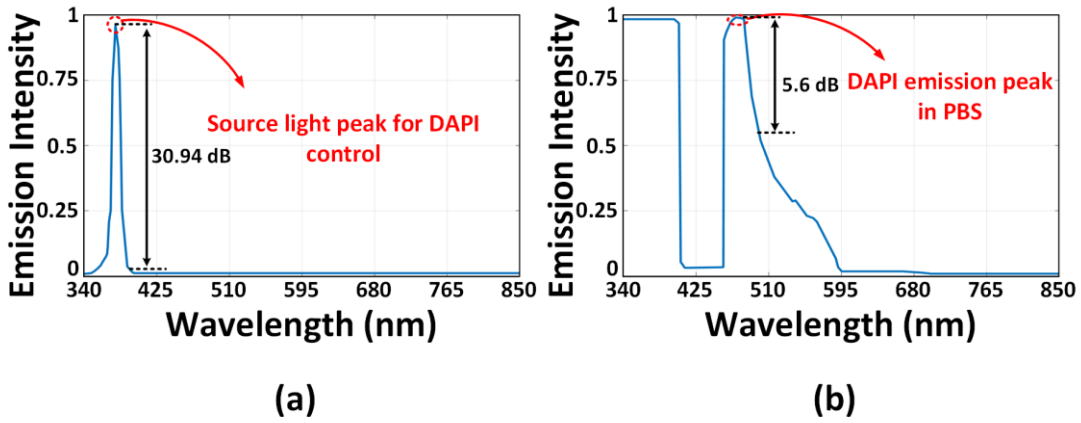

Fig. 3.16. (a) Spectral response of Alexa Fluor 488 diluted in PBS. (b) Spectral response of DAPI diluted in PBS.

nm is equal to 10 µV at 1 Hz. Considering the measured prototype responsivity of 85 mV/nW, which includes the CG and the responsivity of the spectrometer, the measured P_{min} of the prototype is equal to 117 fW. This result lies within the same order of the minimum detectable power of the spectrometer alone (50 fW). An attenuation of 1.5 dB is measured from the fiber tip to the input slit of the spectrometer, which represents light coupling losses. As shown in Eq. 3.7, changes in wavelengths can contribute to increasing the P_{min} of the prototype compared with the spectrometer alone. As shown in Eq. 3.6, the sensitivity of the prototype could be further increased by raising t_i (set to 435 µs in this design), which would, in turn, enhance the responsivity of the entire prototype by decreasing the P_{min} value. Moreover, to calculate the P_{min} at 461 nm, the measured V_n at 1 Hz, which was 17 µV, is divided by 90 mV/nW, giving P_{min} =188 fW. The prototype weighs 19 g, and its dimensions are 30 mm × 24 mm × 43 mm, which makes it smaller than previous solutions [37]. The fiber has a length of 20 mm and a diameter of 1 mm, which circumscribes the detection area to the irradiance surface of 8.8 mm^2 at an approximate distance of D = 2 mm under the tip of the fiber, allowing the device to collect the emission light from small confined samples. These performance characteristics enable the prototype to detect micro-volume concentrations of analytes with reproducible results at a reasonable limit of quantification (LOQ), as shown by *in vitro* results

reported in the next section. Table 3.5 provides a summary of the cost of the prototype in US dollars, the overall cost of which is around $285, well below any commercially available benchtop spectrophotometers such as the FLAME-T-UV-VIS-ES from Ocean Optics and C13985-20 from Hamamatsu, which cost above $4000 and $1000, respectively.

3.7.2. Measured *in vitro* Results

VERO E6 cells (African green monkey) provided by Dr. Gary Kobinger's Lab (Université Laval, Quebec City, Quebec, Canada) and two fluorescent dyes were used to validate the fiber-spectrophotometer prototype. VERO E6 cells contain tubulin, a structural protein of mammalian cells. Tubulin can be used as a biomarker to detect several types of cancers. To tag the tubulin protein, an antibody is required as an interface between the protein and the fluorescent dyes. Anti-tubulin antibody (Cat. No. ab4074) was purchased from Abcam (Cambridge, MA, USA) to function as the primary antibody against tubulin protein. Alexa Fluor 488 (Cat. No. A-11059) conjugated as the secondary antibody to carry fluorescent signals and 4′, 6-diamidino-2-phenylindole-DAPI

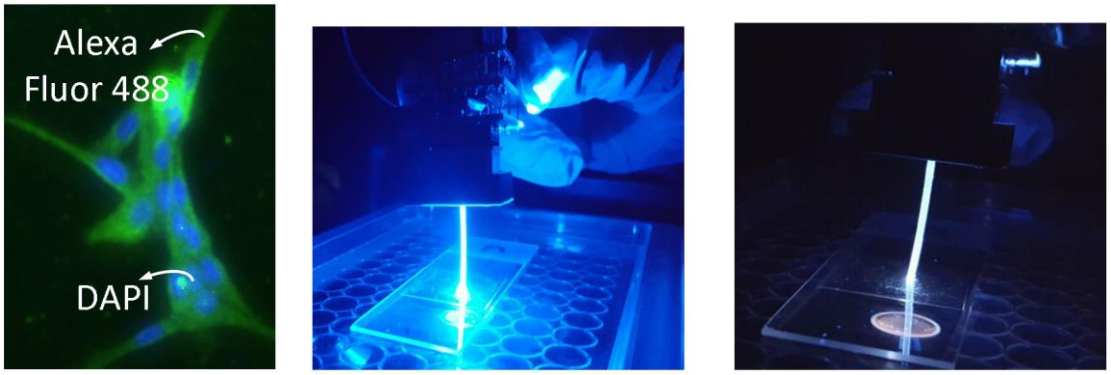

Fig. 3.17. (a) Cells are tagged with Alexa Fluor 488 and DAPI, which are respectively shown in green and blue. Image taken with an Olympus IX81 microscope from Vero E6 cells tagged by Alexa Fluor 488 and DAPI. The Image shows that different tags allow marking of the core and the body of the cells. (b) Picture of the experimental setup used to detect the Alexa Fluor 488 fluorescence emission of the tagged cells. (c) Picture of the experimental setup used to detect the DAPI fluorescence emission of the tagged cells.

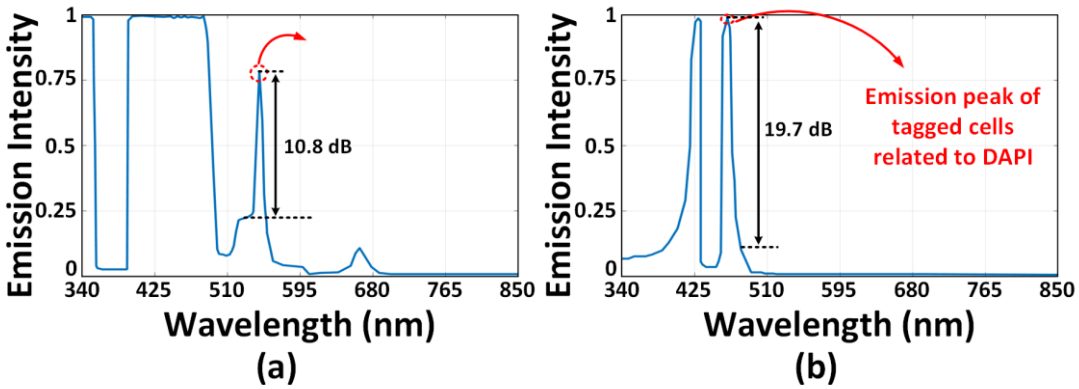

Fig. 3.18. (a) Spectral response of stained VERO E6 cells illuminated with blue light. (b) Spectral response of stained VERO E6 cells illuminated with ultraviolet light.

(Cat. No. D1306) for nucleus staining, which was both provided by Thermo Fisher Scientific (Waltham, MA, USA), were used as fluorescent dyes. The Synergy H1 Hybrid Reader spectrophotometer from BioTek (Winooski, VT, US) was used to validate the performance of the prototype. The extremely small protein size requires the spectrophotometer to resolve micro volumes. The measured light emission spectrum of the micro-volume SUTs can be used by physicians to support and improve the precision of diagnostics. The performance is assessed using two main types of spectrophotometry tests: 1) selectivity performance and 2) sensitivity performance. The selectivity experiments were designed to verify the capability of the prototype to discriminate between different fluorophores. These fluorophores were excited using the blue and ultraviolet lights of the Olympus IX81 microscope, and their fluorescence emissions were measured with the fiber-spectrophotometer prototype. In order to use the different wavelengths of the microscope as excitation sources, the embedded excitation LED of the prototype was disabled, while the excitation filter and the dichroic mirror were bypassed to assess the selectivity of the prototype. Using this setting allowed the evaluation of the capability of the prototype to discriminate between different light wavelengths within the range of 340 nm to 850 nm. As shown in Figs. 3.17 (b) and (c), the sample was placed on a glass slide above the microscope light source to generate fluorescence emission light. This emission light, along with the source

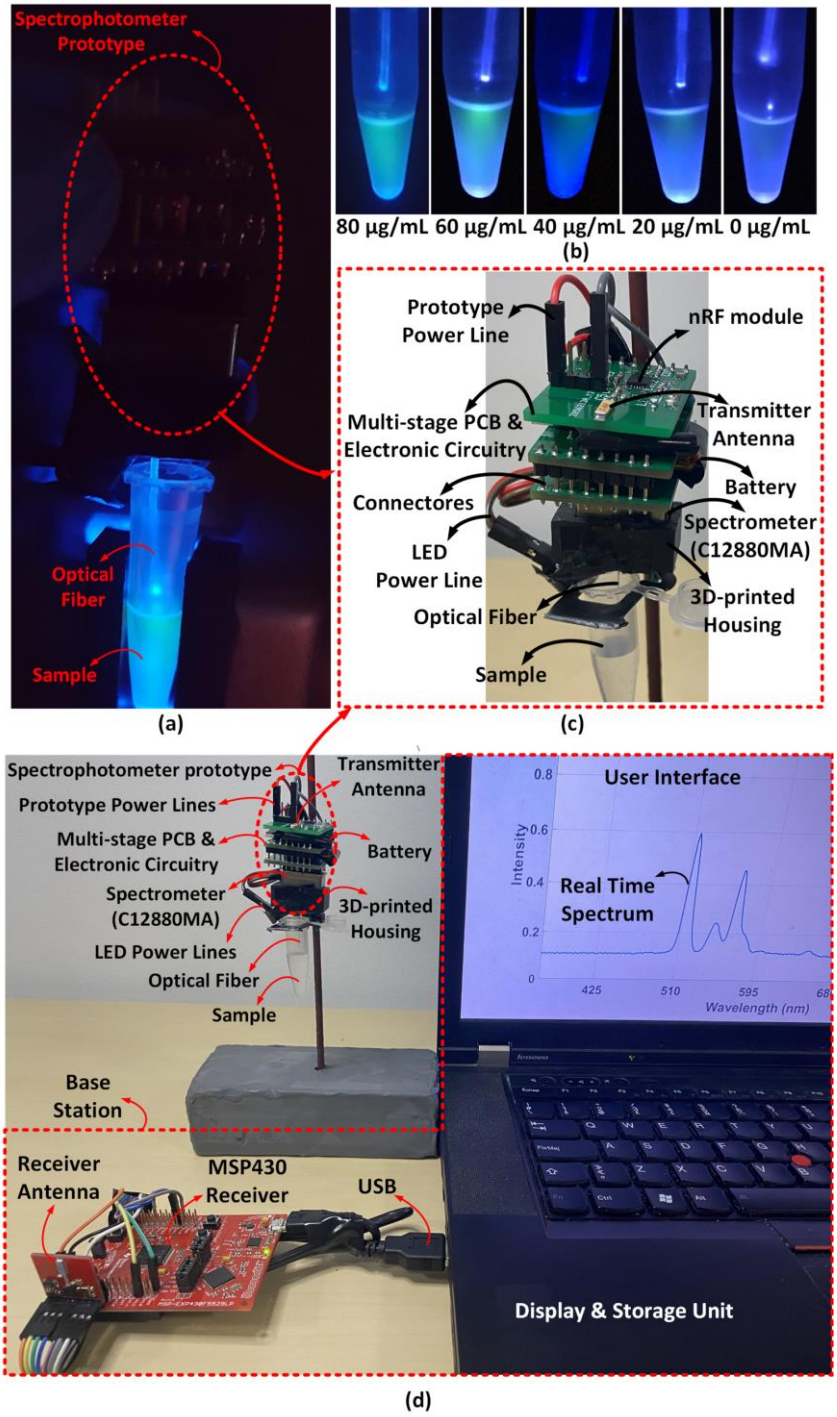

Fig. 3.19. (a) Experimental setup used to measure the sensitivity of the prototype. (b) Measured fluorescence response of different concentrations of Alexa Fluor 488. (c) The cell fiber-spectrophotometer prototype used for these tests. (d) The whole experimental setup, including the sample, the spectrophotometer prototype, the base station, and the user interface.

light, passed through the sample and reached the prototype fiber tip and placed on top of the sample. The prototype was held with a 3D-printed plastic holder

above the sample to collect the emission and source light. The sensitivity of the prototype was assessed by measuring the response of the fluorophore Alexa Fluor 488. The SUT was placed at an approximate distance of D = 2 mm below the tip of the prototype fiber and illuminated by the LED through the optical fiber. The fluorescence emission of the sample was retrieved with the same fiber, as shown in Fig. 3.17. In these sensitivity tests, the LED provided constant optical output power with a peak wavelength of 470 nm, while the SUT concentration was varied. The prototype measured the change in the amount of fluorescence light emitted by the SUT when the SUT concentration was changing.

On the one hand, the selectivity test demonstrates the capability of the prototype to discriminate between the main peak wavelength of a specific fluorophore and those of other fluorophores and/or light sources. These measurements can generate qualitative results for the identification of a specific compound by showing its emission peak at a specific wavelength depending on the presence or absence of a given fluorophore, as shown in Figs. 3.18 (a) and (b). On the other hand, the sensitivity tests measure the performance of the prototype to assess the concentration of a SUT, and its fluorescence emission intensity changes with the concentration. Different criteria, including the linear dynamic range (LDR), the LOD, the LOQ, the intra-day relative standard deviation (RSD), and the inter-day RSD, are available to validate the sensitivity, precision, and stability of this prototype. The prediction error of analyte concentration is provided in the next sections to evaluate the benefit of using a photodetector array instead of a single photodiode to detect the incoming fluorescence light.

1) Selectivity Performance: The selectivity tests comprise two main steps to identify different fluorophores. First, Alexa Fluor 488 and DAPI fluorophores were diluted in a 10 mM phosphate-buffered saline (PBS) solution in various wells on a 12-well plate. A solution of 10 mM PBS also served as control. The wells were then illuminated with the blue and ultraviolet lights as the corresponding excitation lights for each fluorescent label by the microscope. As shown in Figs. 3.15 (a) and 3.26 (a), the prototype detected a peak at 470 and 358 nm when the control solution was illuminated with the blue and ultraviolet

Table 3.6 Prediction Error for different Reading States

Parameter	I_{total}	I_{max}, (I_{total}+$\mathcal{E}_{max}$*)	I519, (I_{total} +$\mathcal{E}_{519}$**)
MAE	0.854	1.352, (I_{total} + 0.498)	1.695, (I_{total} + 0.841)
MSE	1.149	2.914, (I_{total} + 1.765)	5.221, (I_{total} + 4.072)
RMSE	1.072	1.707, (I_{total} +0.635)	2.285, (I_{total} + 1.213)

*$\mathcal{E}_{max}$ = I_{max}-I_{total}, **$\mathcal{E}_{519}$ = I_{519}-I_{total}

lights, respectively. In another case, the prototype could measure two peaks, as shown in Fig. 3.15 (b) when the 470 nm excitation wavelength was used to illuminate another well containing Alexa Fluor 488. One peak is related to the excitation light at 470 nm, and the other is related to the fluorescence light emitted at 519 nm. The result of the well containing DAPI, which is illuminated at 358 nm, is shown in Fig. 3.16 (b). Two peaks were observed: one at 358 nm, which corresponds to the excitation light source, and another at 461 nm, which corresponds to the fluorescence emission of DAPI molecules. These results show the capability of the prototype to discriminate between two types of fluorescence emissions, namely the Alexa Fluor 488 emitting at 519 nm and DAPI emitting at 461 nm, during excitation by a blue and an ultraviolet light source, respectively. The signal-to-noise ratio (SNR) was calculated for both measured fluorophores to assess the prototype's selectivity performance of the prototype. The prototype resolution is 15 nm; thus, the SNR is calculated as follows: the peak light power ($P_{\lambda peak}$) is compared with P_N, which is the highest noise power measured outside the interval λ_{peak}±15 nm ranging from 340 nm to λ_{peak}-15 nm and from λ_{peak}+15 nm to 850 nm, where λ_{peak} is the wavelength of the peak power.

$$SNR = 10\,log\left(\frac{P_{\lambda peak}}{P_N}\right), \tag{3.8}$$

Figs. 3.15 (a), (b), 3.16 (a), and (b) respectively indicate that the measured SNR is 7.5, 9.85, 30.94, and 5.6 dB for the 470 nm light source, the Alexa Fluor 488 diluted in PBS, the 358 nm light source, and the DAPI diluted in PBS, respectively. These measurements demonstrate the capability of the prototype to discriminate between different light sources and fluorophores inside a SUT within the prescribed wavelength range.

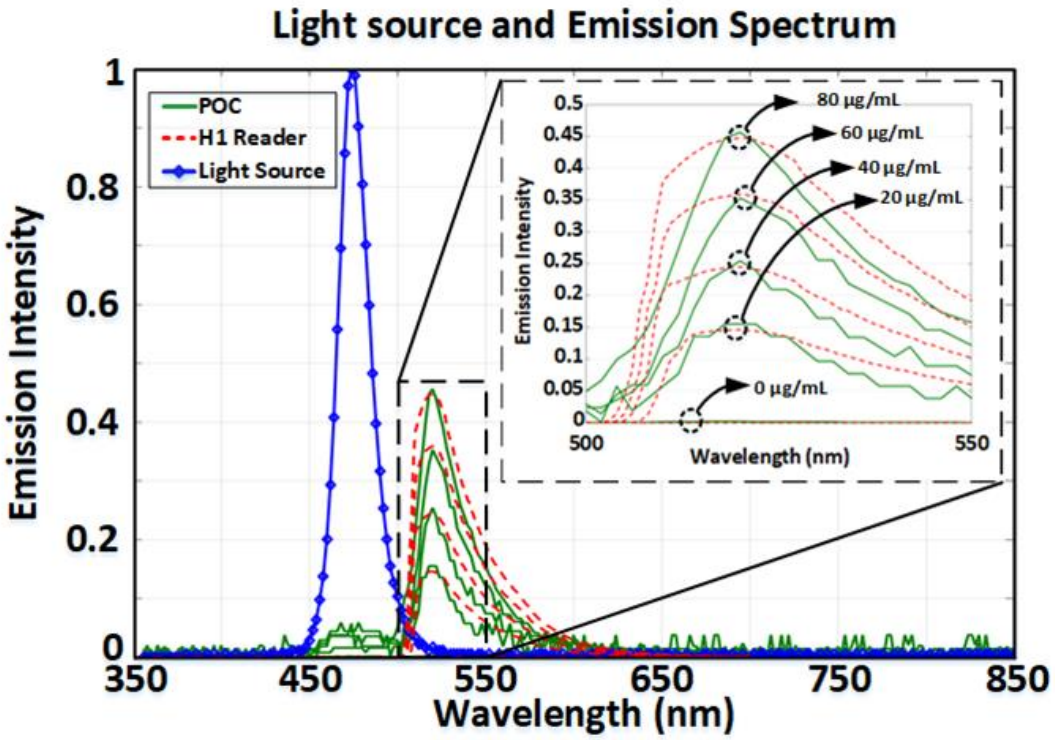

Fig. 3.20. Measured spectrum of light source and fluorescence emission. It also zoomed at the *in vitro* experimental results of the quantitative experiments for different concentrations from 0 to 80 µg/mL. The normalized spectra measured with the prototype for different concentrations of Alexa Flour 488 (green solid lines) are similar to those measured with the Synergy H1 Reader (red dashed lines), a commercial spectrophotometer. The results for each concentration obtained with the prototype and the commercial spectrophotometer are within a range of 0.9%.

Then, the selectivity test was performed *in vitro* with VERO E6 cells tagged with DAPI and Alexa Fluor 488. The DAPI labels the DNA of the cells, and Alexa Fluor 488 stains the tubulin proteins. Thus, fluorophores detection in the SUT demonstrates the presence of VERO E6 cells DNA and tubulin proteins. To prepare the sample for this experiment, VERO E6 cells were fixed on a cover slip and hybridized using an anti-tubulin antibody followed by the secondary antibody Alexa Fluor 488 for protein detection. These fixed cells were incubated with DAPI for nucleus staining. The cover slip was placed on a glass slide and observed under the Olympus IX81 microscope. The shape of the marked cells was captured by the microscope to validate the fulfilled steps of staining. Fig.

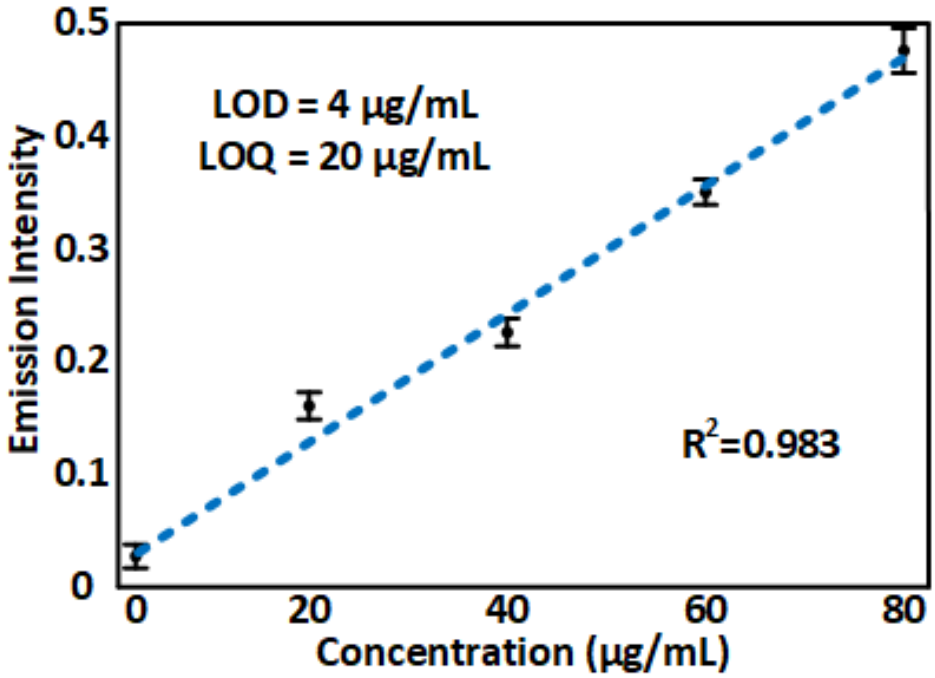

Fig. 3.21. Linear calibration plot for the measurements of the related emission intensity versus concentration levels. Each point represents the averaged value of 15,000 points measured during 30 s for a specific concentration of Alexa Fluor 488. Five concentration values were measured over three days. A regression coefficient (R^2) of 0.983 shows that more than 98% of the variation of the related emission intensity is due to the variation of the analyte concentration.

3.17 (a) presents the stained cells provided to perform the *in vitro* experiments. Figs. 3.17 (b) and (c) present the experimental configurations for detecting Alexa Fluor 488 and DAPI labeled cells, respectively. These experiments were performed with the light sources of the Olympus IX81 microscope in the absence of LED in the housing of the prototype. Figs. 3.18 (a) and (b) present

Table 3.7 Measurement Performance and Figures of Merit

Parameter	Value
LDR	0–80 µg/mL
LOQ	20 µg/mL
LOD	4 µg/mL
R^2	0.983
Precision (RSD %) Intra-day	1.5
Precision (RSD %) Inter-day	4.7

the MATLAB plots, which respectively have two peaks indicating the excitation light source and the fluorescence emission of the tagged cells. The peaks at 470 and 358 nm correspond to the wavelengths of the light sources, while the peak at 519 nm corresponds to the fluorescence emission of the Alexa Fluor 488. The peak at 461 nm corresponds to the fluorescence emission of the DAPI. Fig. 3.18 (a) shows that the prototype can detect Alexa Fluor 488 in the SUT in the presence of DAPI. The peak has a power of 10.8 dB above other wavelengths ±15 nm around the peak wavelength. Fig. 3.18 (b) shows the detection of DAPI with a peak power above other surrounding wavelengths by 19.7 dB. The selectivity experiment results obtained from the cells labeled with Alexa Fluor 488 and DAPI show that the fiber-spectrophotometer prototype can properly detect the presence of the tubulin protein stained by different fluorescent dyes.

2) Sensitivity Performance: The capability of the prototype to detect different concentrations was assessed using the experimental setup shown in Fig. 3.19 (a). The same procedure as for the selectivity experiments was used to prepare five concentrations of Alexa Fluor 488, including 0, 20, 40, 60, and 80 µg/mL, and conduct fiber-spectrophotometry experiments, as shown in Fig. 3.19 (b). An optical fiber, a blue LED, an excitation filter with a center frequency/bandwidth of 470/24 nm, and a dichroic mirror with a cut-off frequency of 495 nm were assembled together to form a complete prototype (shown in Fig. 3.19 (c)) for the aforementioned experimental measurements. The blue LED, embedded in the 3D-printed housing, is driven by the LED driver circuit mounted on the electronic board and powered by the battery to provide the excitation light of the sample. The blue light first reaches the excitation filter, which narrows the spectrum of the excitation light. Then, the dichroic mirror collimates the blue light into the fiber. The 20 mm length and 1 mm diameter fiber was placed on the top of the sample surface, as shown in Fig. 3.19 (a), to retrieve the fluorescent light. The enclosure and the passive optical components prevent the leakage of ambient light into the spectrometer and enhance the entire system for precise concentration measurements.

In these experiments, the given concentrations of analytes were illuminated by the blue LED, while the prototype measures their spectrum. The prototype

digitizes the fluorescence emission and sends the results wirelessly to the base station for data analysis, storage, and real-time display of the spectral response. Fig. 3.19 (c) shows a picture of the prototype, and Fig. 3.19 (d) presents the whole experimental setup, including the sample, the spectrophotometer prototype, the base station, and the user interface. The spectrophotometry experiments were performed with different SUT concentrations to demonstrate the capability of the prototype to measure a wide range of concentrations. Fig. 3.20 shows the fluorescence emission spectrum, the peak amplitude, the wavelengths, and the excitation source spectrum measured with the prototype for different concentrations. This figure reveals that different concentrations of SUT produce different proportional amplitudes at 519 nm. The prototype measured the spectrum data, while the sample was exposed to the excitation light for 30 s. The prototype can collect the necessary data to measure one spectrum within 1.905 ms, using a refresh rate and sampling frequency of 525 Hz and 2 MHz, respectively. The samples were measured for 30 s with the prototype to ensure the excitation of a majority of fluorophores inside the SUT and provided contributions to the measured spectrum [75]. One 30 s measurement allows the acquisition storage of around 15,000 spectral responses for each experiment while each spectral response has 288 points, and the spectral refresh rate is 525 Hz. The collected spectrum data were then averaged as commonly conducted in commercial spectrophotometers [76] to increase the reliability and precision of the measured results and decrease the variation error of each experiment. The experiments were performed three times per day and repeated for three days with the same 30 s duration. The minimum quantifiable concentration or the LOQ, the value for which the prototype can maintain a linear detection range within 1% from 0 to 80 µg/mL, was found to be 20 µg/mL. The experiments were repeated with small concentrations of less than 20 µg/mL to calculate the LOD. The results show that the prototype can resolve minimum concentration values down to 4 µg/mL, giving a LOD of 4 µg/mL.

The Synergy H1 commercial spectrophotometer from BioTek was used to further validate the performance of the prototype and compare the quantitative measurements. Fig. 3.20 shows a close view of the fluorescence emission

Table 3.8 Comparison Table

Parameter	This Work	[18], [24]	[40]	[39]	[38]
Power (mW)	103	600	100	100 [a]	7200
Resolution (nm)	15	50	-	-	-
Responsivity (mV/nW)	85	24	0.003	-	-
Weight (g)	19	3.6 [b]	-	-	5600
Size (mm^3)	30×24×43	22×8×17	-	115.2×62×22	186×274×173
LOD	25 nM, 4 µg/mL	-	1 µM	0.5 µM	20 µg/mL

[a]Only light source power
[b]w/o Battery

spectra measured with the prototype and the commercial spectrophotometer for comparison. As presented, the accuracy of the prototype is comparable with that of the commercial spectrometer for incremental concentrations of different solutions within an agreement of 0.9%. Meanwhile, the size, power consumption, and cost of the prototype are several orders of magnitude below the commercial system.

3.7.3. Data Analysis and Discussion

3.7.3.1. Performance Validation

Instead of measuring a narrow wavelength band, measuring the entire spectrum using this prototype provides enhanced precision, minimal error, and effective resolution. MAE, MSE, and RMSE metrics are evaluated to perform such a comparison to present the prediction error rates and the performance of the prototype. These metrics are then compared with the errors obtained for a single photodiode detection. Errors are calculated on the basis of predicted concentrations, while the real concentrations of SUT are known a priori and considered as ground truth. Linear regression analysis is performed on the measured spectral data set to evaluate the performance of this approach. Thus, a set of the fiber-spectrophotometry spectrum was recorded and split into training and testing data to learn and validate the regression model. The regression data set included 2350 trials for each concentration, into which 20%

of the data is used for testing. First, 80% of the entire data set is used for training, and then the remaining data are utilized to test the model and extract the prediction error. The linear regression is implemented using Python for three different measured data sets:

1) Overall Spectral response (I_{total}): represents the measured emission of Alexa Fluor 488 by the prototype from 340 nm to 850 nm during the sensitivity experiments.

2) Measured fluorescence at 519 nm (I_{519}): represents the response of a single photodiode at the emission peak wavelength of Alexa Fluor 488 recorded during sensitivity experiments.

3) Maximum measured intensity (I_{max}): represents the maximum measured value of the Alexa Fluor 488 spectral response during the sensitivity experiments.

For each of the above-measured data sets, the mean absolute error (MAE), mean squared error (MSE), and root mean squared error (RMSE) are calculated and presented in Table 3.6. These metrics assess the prediction error rates of the regression analysis. The MAE, MSE, and RMSE of I_{total} are 0.854, 1.149, and 1.072, respectively, which are less than the prediction errors of I519 and Imax. Comparing the errors of I_{total} and I_{max} indicates that even if the single photodiode always detects the maximum fluorescence value, it has more errors than for Itotal. The results listed in Table 3.7 show that estimating the concentration of analytes using the entire spectrum instead of using the single value of the narrow-band filtered (typically from 515 nm to 560 nm as in [21]) fluorescence emission light power measured with a single photodetector can improve the accuracy by as much as 78% when comparing the MSE. Table 3.6 also shows an improvement of 53.09% and 36.8% when comparing the RMSE and the MAE, respectively.

3.7.3.2. Data analysis

The selectivity tests present the discrimination capability of the prototype between different fluorophores. The measurements show 10.8 and 19.7 dB distinction capabilities for Alexa Fluor 488 and DAPI, respectively, in the presence of another fluorophore. The linearity and the precision of the prototype

were derived from the sensitivity tests. Calibration curves were measured using standard solutions of five concentration levels of Alexa Fluor 488. The measured LDR between the analyte concentration and the fluorescence emission intensities was 0–80 µg/mL with a correlation coefficient square (R^2) above 0.98. This result shows that the detected level of fluorescence emission is effectively correlated with the concentration. The LOD and LOQ of the data measured by the sensitivity tests are 4 and 20 µg/mL, respectively. Intra-day RSD of 1.5% was calculated three times with the analysis of the sample solution of 20 µg/mL. Meanwhile, the inter-day RSD of 4.7% was obtained using the same method for three consecutive days. Fig. 3.21 shows the calibration plot of the processed data. Each point represents an average value for a given concentration of Alexa Fluor 488 extracted after repeating the experiment three times with a 30 s duration each. As summarized in Table 3.7, the prototype has a precision of 4 µg/mL (or 25 nM) and can quantify the concentration of micro-volume analytes within a linear range of 0–80 µg/mL with excellent repeatability. Table 3.8 presents the detection performance and a comparison of the presented prototype with previously reported solutions. The presented approach improves the detection performance compared with other solutions by measuring the overall spectral response, which allows capturing additional fluorescence emission light power.

3.8. Conclusion

The design and measured performance of a wireless miniature cell fiber-spectrophotometer prototype, which is used to detect biomarkers based on fluorescence sensing, were presented in this chapter. Overall, the prototype can detect micro-volume analytes, while the size, cost, and power are decreased compared with previous studies. Experimental measurements performed *in vitro* show the viability of the prototype to discriminate between different fluorophores and evaluate the concentrations of analytes based on their measured fluorescence emissions. The prototype is portable and inexpensive and can be quickly interfaced with software for real-time sample monitoring. Furthermore, instead of using a single photodetector, employing a grating and a photodetector array, as performed in the C12880MA spectrometer, avoided the utilization of an excitation light emission blocking

filter in front of the photodetector. Such an approach allows the collection of additional fluorescence emission light power to increase the sensitivity down to micro-volume concentrations of analytes. The presented prototype allows for less prediction error compared with narrow-band emission measurements using a single photodetector, and its sensitivity is comparable with those of commercially available benchtop cell spectrophotometers, while providing low-power consumption, low-cost, low weight, and small dimensions. This performance holds promise for effective POC solutions in various important applications of fluorescence cell spectrophotometry, such as the rapid testing of individuals for infectious diseases, like SARS-CoV-2, or for cancer.

ACKNOWLEDGMENT

The authors would like to thank Dr. Garry Kobinger from the Department of Microbiology and Infectious Diseases at Université Laval for providing the VERO E6 cells. We acknowledge the support of the Canada Research Chair in Smart Biomedical Microsystems and CMC Microsystems.

Chapter 4

High-Precision Ping-pong Auto-zeroed Lock-in Fluorescence Photometry Sensor

4.1. Résumé

Ce chapitre présente un capteur de photométrie à fluorescence CMOS de haute précision utilisant un nouveau schéma d'amplification à verrouillage basé sur la polarisation commutée et la mise à zéro automatique ping-pong. Les capteurs CMOS comprennent deux photodiodes et un amplificateur à verrouillage fonctionnant à 1 kHz. L'amplificateur à verrouillage comprend un amplificateur de transimpédance différentiel à faible bruit utilisant un nouveau schéma de mise à zéro automatique du ping-pong à polarisation commutée, une rétroaction d'alignement de phase automatique, un amplificateur à gain programmable, un filtre passe-bande, un mélangeur et un filtre passe-bas de sortie. La conception a été fabriquée selon un processus CMOS 0,18 µm et les performances mesurées montrent que l'amplificateur à verrouillage peut récupérer des signaux d'entrée bruyants avec une réserve dynamique de 42 dB tout en ne consommant que 0,7 mW à partir d'une tension d'alimentation de 1,8 V. L'amplificateur opérationnel central de l'amplificateur de transimpédance a un gain CC de 86 dB, une bande passante à gain unitaire de 30 MHz, une consommation électrique de 263 µW et un bruit référé à l'entrée de 40,6 nV/√Hz à 1 kHz. Les résultats des tests optiques montrent que l'amplificateur à verrouillage peut détecter la lumière incidente avec une puissance optique allant de 8 nW à 24 µW, avec une sensibilité de 250 V/mW. La conception proposée a été encapsulée dans un boîtier imprimé en 3D et validée *in vitro* en effectuant une détection de biomarqueurs en temps réel. Dans cette conception, la lumière DEL traverse une fibre visant à éclairer une zone spécifique d'une culture cellulaire. Une configuration de boulon et d'écrou est conçue et mise en œuvre pour maintenir la configuration de la DEL et de la fibre et contrôler le champ de vision. Des expériences avec une solution de billes diluée dans du PBS démontrent que le capteur a une sensibilité de 1:100k. Une expérience *in vitro* a été menée avec des cellules de fibroblastes

de souris embryonnaires NIH3T3 marquées avec un colorant de membrane cytoplasmique pour montrer la capacité du prototype à détecter différentes densités de culture cellulaire. Le montage expérimental comprend deux lentilles optiques pour filtrer les lumières d'émission et d'excitation, un pilote de DEL, une DEL pour exciter les fluorophores, un microcontrôleur pour numériser et transmettre les résultats à un ordinateur avec une connexion USB, un amplificateur de verrouillage et deux photodiodes mis en œuvre sur une puce conçue sur mesure et un boîtier imprimé en 3D. La faible consommation électrique (36,7 mW) et la légèreté (120 g) du montage expérimental en font un candidat prometteur pour les applications portables.

4.2. Abstract

This chapter presents a high-precision CMOS fluorescence photometry sensor using a novel lock-in amplification scheme based on switched-biasing and ping-pong auto-zeroing. The CMOS sensor includes two photodiodes and a lock-in amplifier (LIA) operating at 1 kHz. The LIA comprises a differential low-noise transimpedance amplifier using a novel switched-biasing ping-pong auto-zeroed scheme, an automatic phase aligner with feedback, a programmable gain amplifier, a band-pass filter, a mixer, and an output low-pass filter. The design is fabricated in CMOS 0.18-µm process, and the measured performance shows that the LIA can retrieve noisy input signals with a dynamic reserve of 42 dB, while consuming only 0.7 mW from a 1.8 V supply voltage. The measured results show that the LIA can detect a wide range of incident light optical power from 8 nW to 24 µW, with a sensitivity of 250 V/mW. The proposed design is encapsulated in a 3D-printed housing allowing for real-time in vitro biomarker detection testing. This ambulatory platform uses an LED and an optic fiber to convey the excitation light to the sample and retrieve the fluorescence signal. Experiments with a beads solution diluted in PBS demonstrate that the sensor has a sensitivity of 1:1 k. Experimental results obtained *in vitro* with NIH3T3 mouse embryonic fibroblast cells tagged with cytoplasmic membrane dye show the ability of the prototype to detect different densities of cell culture. The portable prototype, which includes an optical mirror, lenses and a small 30 mm × 36 mm × 30 mm printed circuit board enclosed inside the 3D-printed housing, consumes 36.7 mW and weighs 120 g.

4.3. Introduction

Fluorescence cell photometry allows to detect and measure the concentration of various biomarkers *in vitro* or *in vivo*. These important physiological measurements are key parameters in the diagnostic and treatment of diseases, such as cancer [47], and neuropsychiatric disorders [10]. Fluorescence photometry is also instrumental to detect viral structural components of infectious diseases, such as COVID-19 [1]. As shown in Fig. 4.1, a photometry system includes multiple blocks. A source of light is used to excite the sample under test (SUT) labeled with fluorophores or expressing a fluorescent protein [33]. Optical filters and mirrors are used to direct the excitation light towards the sample, and the re-emitted fluorescent light to the sensor. A photodetector is used to convert the fluorescence light into an electrical signal. An analog front-end unit detects and amplifies the electrical signal while a data acquisition unit digitizes and transmits the raw data. Signal processing and data analysis are often performed online or offline to improve signal quality and to support diagnostics. The results can then be used to identify and quantify biological analytes, such as proteins [15], DNAs [13], and RNAs [17].

Optical fiber photometry is currently used in experimental neuroscience to assess the effect of medication on neural activity by measuring calcium fluorescence signals inside deep brain structures [10]. The development of neuropsychiatric disorders, as well as the relationship between specific neural circuits and social interactions can be studied thanks to this approach. In [11], a new photometry sensor prototype was designed to measure two fluorophores in parallel. Benchtop components and lasers were used to achieve high precision at the cost of a bulky and power-hungry prototype. A great deal of research effort has been devoted to decrease the size and the power consumption of fluorescence photometry devices. An on-chip fluorescence photometry system is presented in [19]. A nanostructured high-pass optical filter is used to fully integrate the whole photometry system inside a single chip. The filter implementation requires a lithography process having a precision of less than 100 nm. The nanoplasmonic filter fabricated in a 65-nm CMOS technology uses copper-based metals and on-chip interconnects to interact with the presented optical fields. However, the precision of detection of the system is

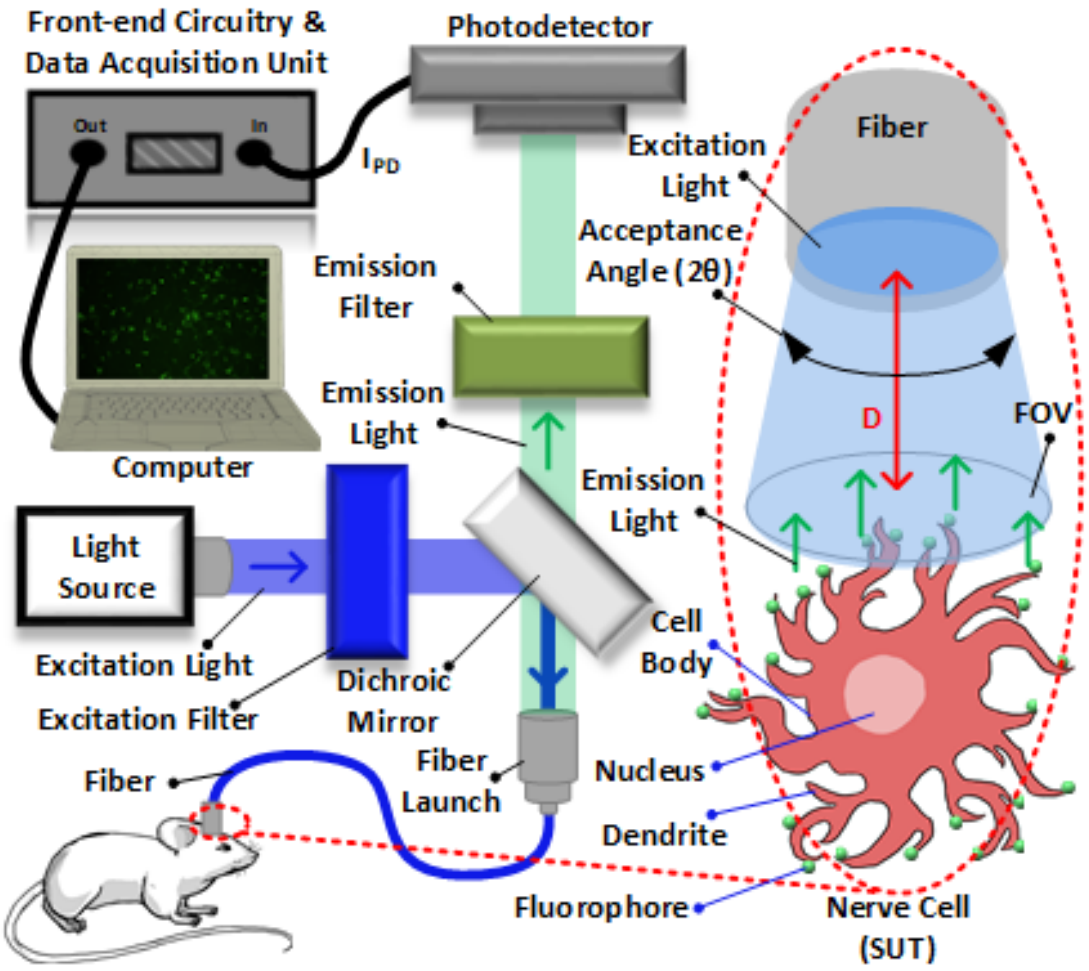

Fig. 4.1. Block diagram of a conventional fluorescence cell photometry system: The excitation light passes through a filter to narrow its emission spectrum. Then, the excitation light (blue) goes toward the SUT through the fiber to control the illumination area (FOV). The excited fluorophores re-emit fluorescence light at higher wavelength (green), which passes through the emission filter to reject any wavelength other than the emission light. The photodetector converts the light to an electrical current (I_{PD}), which is then detected, converted into a voltage signal, and amplified by the front-end circuitry. The data acquisition unit digitizes this raw voltage and delivers it to a host computer, where the data are analyzed, displayed, and stored.

limited by laser excitation noise, external stray light scattering, circuit noise, and biological noise. A miniature and wireless fiber photometry system using a capacitive transimpedance amplifier (CTIA) as front-end amplifier is presented in [21]. The utilization of a CTIA allows to convert the output current of the photodetector (I_{PD}) into a voltage with high precision while consuming low

power. However, the use of high-precision switched-capacitor (SC) circuits consuming a fair amount of power can limit the utilization of this prototype to specific applications requiring a low sampling rate. Furthermore, like in many systems, no mechanism against ambient noise and motion artifact is provided. For high-precision fluorescence measurement, an isobestic light source can be used to cancel the effect of autofluorescence and motion artefacts [65], at the cost of increasing the size and complexity of the device, as well as the power consumption [35].

In terms of precision, since the photocurrent I_{PD} is often obtained under low illumination, the signal can sometimes be buried in noise. Retrieving the fluorescence signal overshadowed by such high noise power level using conventional analog filtering can be very challenging [77]. Alternatively, lock-in amplifiers (LIAs) [78]–[84], have been used to retrieve signals at extremely low signal-to-noise ratio (SNR) by modulating the weak fluorescence signal at a known carrier frequency (f_c). This scheme was shown to eliminate both motion artifacts and ambient noise without drastically increasing the size and power consumption of a fluorescence cell photometry system [26]. In [85], an LIA with an automatic phase-alignment technique was used to improve the precision. Since fluorescence signals are measured at low-frequency, where flicker noise is dominant, especially in CMOS circuits [10], using a chopper amplification scheme can be beneficial [86]. However, using a chopper amplifier can cause more complexity and potential artifacts, like signal ripple and intermodulation distortion [87]. In [88], a chopper amplifier is used with a ripple-reduction loop to compensate for these drawbacks. Nevertheless, chopping typically requires a wideband amplifier, increases complexity and consumes more power [26].

This chapter presents a novel high-precision fluorescence photometry sensor incorporating a custom integrated LIA with two photodiodes (PDs) to realize a fully integrated sensor. The LIA exploits a fully differential switched-biasing ping-pong auto-zeroed TIA to efficiently attenuate the effect of noise and circuits imperfections. An automatic phase-alignment feedback scheme allows to increase the sensitivity of the LIA. The fabricated high-precision CMOS LIA chip is used inside a miniature ambulatory prototype and performs biomarkers detection in a cell culture *in vitro*. The results show that the proposed LIA can

successfully detect various cell densities by measuring the associated light intensities thanks to the highly precise and linear custom integrated LIA. The measured specifications of the LIA chip and the ambulatory prototype are reported, and their performances are compared with other solutions. The remaining of this chapter is organized as follows: Section 4.4 provides an overview of the proposed LIA and explains the system-level modifications. Section 4.5 covers the circuit-level designs. Section 4.6 presents the chip measurement results, Section 4.7 shows the in vitro experimental design and discussion, and Section 4.8 concludes the chapter.

4.4. System Architecture

4.4.1. System Overview

Fig. 4.2 shows the block diagram of the custom CMOS LIA chip utilized in the photometry sensor prototype. The LED driver modulates the LED current with a square-wave voltage ($V_{ref}(f_c)$) at a frequency of f_c = 1 kHz. An LED (LXML-PB02 from Lumileds, San Jose, CA, USA) with a center wavelength of 470 nm is used as an excitation light source. The excited fluorophores re-emit at a higher wavelength, called the emission light, which is near 485 nm for the cytoplasmic membrane dye used in this study. The incident fluorescence light reaches the photosensor chip consisting of two PDs connected to the inputs of a custom LIA. The sensing PD provides a photodiode current (I_{PD}) proportional to the optical power of the detected light, while the dummy PD allows to cancel the dark current using a differential TIA topology. The detected photons include the fluorescence emission light modulated at a frequency f_c as well as some ambient light and noise. The desired fluorescence signal inside I_{PD} is modulated at f_c. Any other light components, such as dark current, are considered as noise and are rejected. The LIA converts I_{PD} into a DC voltage by using several electronic building blocks, as shown in Fig. 4.2. Modulating the target signal with a reference frequency enables the LIA to differentiate between the fluorescence emission light and other additive signals of overlapping spectrum in the baseband, such as motion artifacts or ambient lights [26].

The presented LIA includes three modules: a front-end module, an output module, and an automatic phase-alignment module. The front-end module consists of a TIA, a band-pass filter (BPF), and a programmable gain amplifier

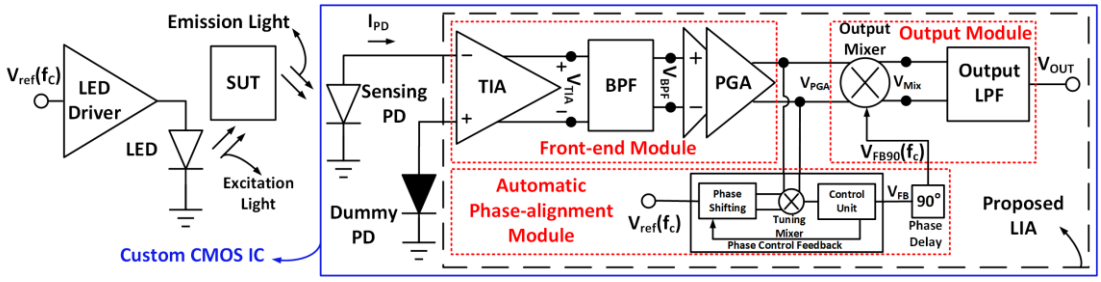

Fig. 4.2. Block diagram of the proposed custom integrated CMOS photometry sensor and its utilization in a prototype. The custom CMOS chip includes on-chip PDs and an LIA. The LIA consists of three main modules: a front-end module, an output module, and an automatic phase-alignment module. The amplitude of V_{OUT} is proportional to the intensity of the detected fluorescence emission light, which is proportional to the concentration of fluorophores inside the SUT.

(PGA). The TIA continuously amplifies I_{PD} and converts it into a voltage signal (V_{TIA}). The amplified signal passes through the BPF, which extracts the input signal from the out-of-band noise and interference to increase the SNR. The BPF is followed by the PGA, which further amplifies the input signal and increases the dynamic range. V_{PGA} is the output voltage of the PGA as shown by Eq. 4.1.

$$V_{PGA} = A_{PGA}(\, sin(2\pi f_c t + \theta_{PGA})), \tag{4.1}$$

where A_{PGA} and θ_{PGA}, and f_c are the peak, phase, and frequency of V_{PGA}, respectively. Afterward, V_{PGA} is fed to the output mixer and to the mixer of the phase-alignment module. The output mixer multiplies V_{PGA} with a square wave generated inside the feedback module (V_{FB90}). The square wave includes a fundamental sine wave (of the same frequency as the square wave) and odd harmonics of the fundamental. Eq. 4.2 shows the multiplication of V_{PGA} with the fundamental sine wave signal of the square wave that has the same frequency (f_c) and phase as V_{PGA} ($\theta_{PGA} = \theta_{FB90}$).

$$V_{Mix} = A_{FB90}(\, sin(2\pi f_c t + \theta_{FB90})) \times A_{PGA}(\, sin(2\pi f_c t + \theta_{PGA})), \tag{4.2}$$

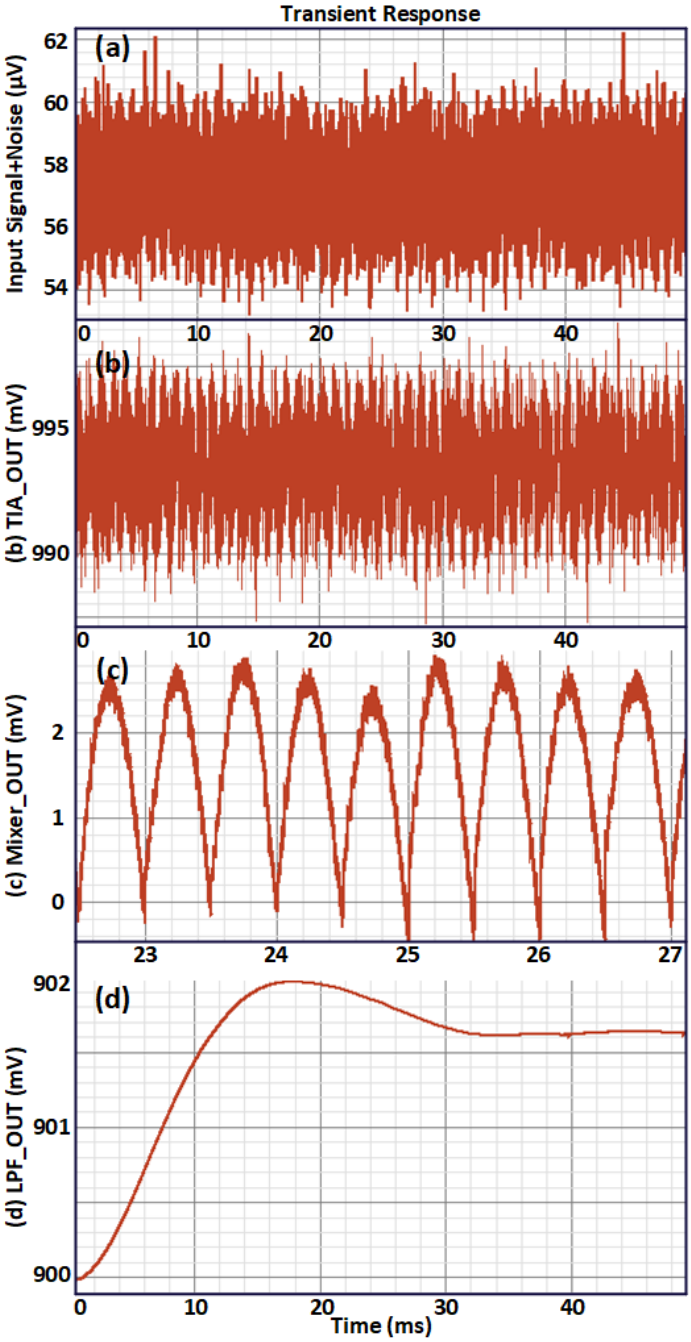

Fig. 4.3. Simulated temporal trace of the lock-in amplifier's response. (a) The input signal includes an AC signal with 10 pA amplitude and 1 kHz frequency that is overshadowed by noise. (b) The TIA amplifies this sine wave input signal that is buried in noise. (c) Then, the output of the mixer shows a rectified voltage that is the result of multiplication of the PGA's output and pulse signal coming out from the feedback. (d) Finally, the output of LPF gives a DC voltage after reaching a constant value that corresponds to the amplitude of the input sine wave signal.

The resulting signal at the output mixer is described by Eq. 4.3.

$$V_{Mix} = \frac{1}{2} A_{PGA} A_{FB90} (cos(\theta_{PGA} - \theta_{FB90}) + cos(2\pi(2f_c)t + \theta_{PGA} + \theta_{FB90})), \quad (4.3)$$

where A_{FB90} and θ_{FB90} are the peak and the phase of V_{FB90}, respectively. As shown in Eq. 4.3, multiplying the modulated input signal with the reference signal demodulates the fluorescence signal and generates two tones at the output of the mixer (V_{Mix}): one tone at 2 × f_c, which must be rejected, and another tone at 0 Hz (i.e. a DC value), which represents the measured fluorescence light signal that must be extracted from V_{Mix}. A narrowband low-pass filter (LPF) at the output module can extract the desired DC level signal and remove the tone at 2 × f_c. The filtered-out voltage (V_{OUT}) is proportional to the target emission light power modulated at f_c. Considering $\theta_{PGA} = \theta_{FB90}$, Eq. 4.3 represents V_{OUT}.

$$V_{OUT} = \frac{1}{2} A_{PGA} A_{FB90}. \quad (4.4)$$

As shown in Fig. 4.2, the automatic phase-alignment module is fed with the same modulation signal (V_{ref}). The automatic phase-alignment module detects the phase of V_{PGA}, compares it with the phase of V_{ref}, and generates a square wave signal at the phase-detection feedback output (V_{FB}). Then, a 90° phase shift is applied to V_{FB} to generate V_{FB90}, which has the same phase as V_{PGA}. The precision of the demodulation process necessitates an accurate adjustment between the phases of V_{PGA} and V_{FB90}, which is realized by the automatic phase-alignment module in this design. As shown in Fig. 4.2, this module includes several submodules that are explained in next sections. As briefly presented in Fig. 4.2, the phase alignment module generates a shifted version of V_{ref} using a phase shifting block. This phase-shifted signal is then compared with the phase of the V_{PGA} signal using a control unit and a tuning mixer. If the control unit detects a 90° phase difference between these two signals, it stops the phase shifting sub-module and delivers the phase-shifted signal to the 90° phase delay block. The result of the automatic phase-alignment module is a signal with identical phase and frequency as V_{PGA} to get the maximum accuracy. Finally, as shown in Fig. 4.1, a data acquisition block

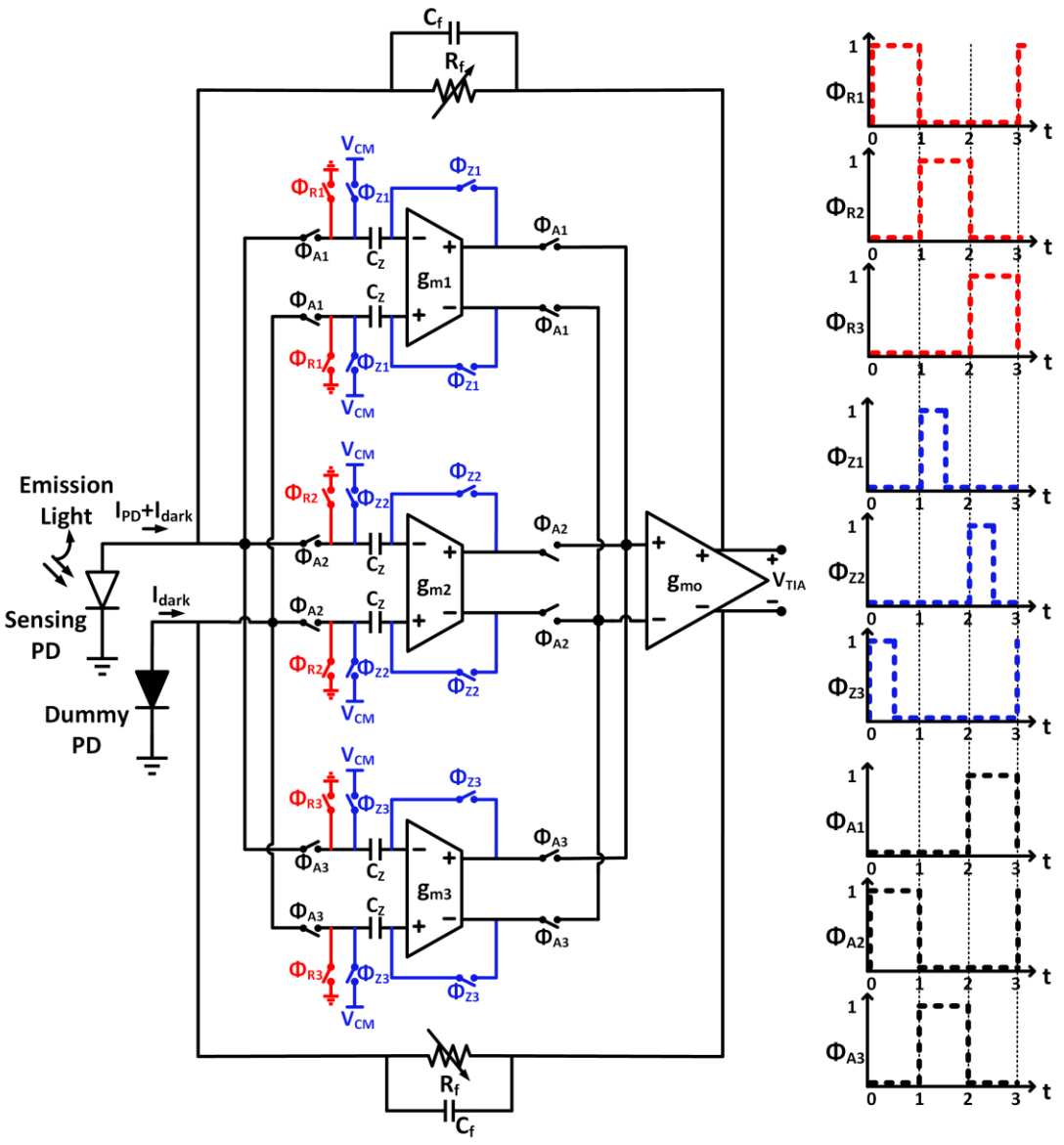

Fig. 4.4. Block diagram of the proposed TIA (left-hand side) and the conceptual timing diagram of switches (right-hand side). The switched-biasing ping-pong auto-zeroed TIA has three input stages (g_{m1-3}) and one output stage (g_{mo}). It includes three phases: 1- zeroing phase (Φ_Z), 2- amplification phase (Φ_A), and 3- reset phase (Φ_R). During the amplification phase of g_{m1} (Φ_{A1}=1), g_{m1} is connected to g_{mo} and delivers V_{TIA}, g_{m2} is storing the offset voltage on its input capacitances (Φ_{Z2}=1), and the transistors of g_{m3} are in the cutoff region to compensate for the flicker noise effect (Φ_{R3}=1). These three phases change between g_{m1-3} to decrease the 1/f noise significantly while delivering V_{TIA} continuously.

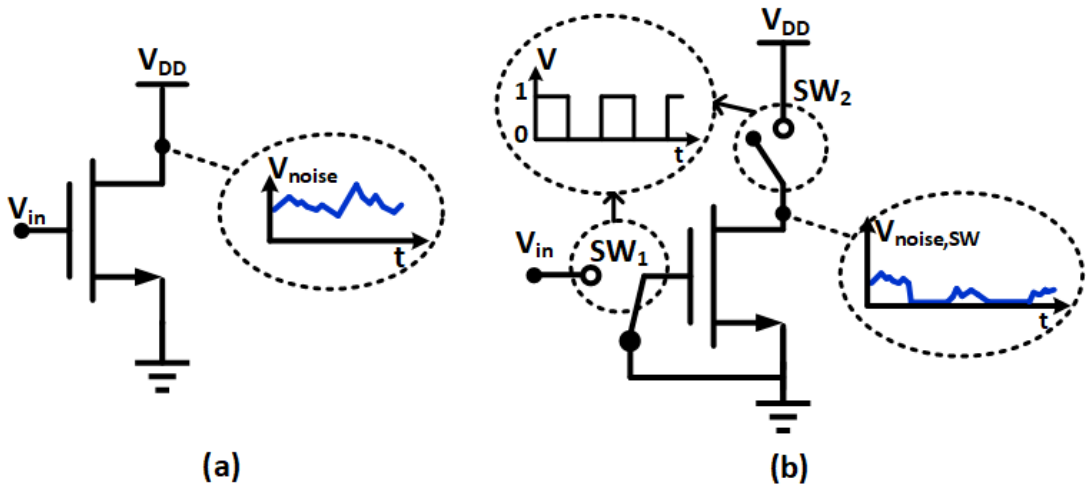

Fig. 4.5. The switched-biasing technique utilize the effect of bias history on noise: (a) Noise performance of a transistor that always works in strong inversion. (b) Noise performance of a transistor with switched-biasing technique, switching between the strong-inversion and the cut-off regions. Cycling a MOS transistor between strong inversion and the accumulation mode reduces an electron's probability of being trapped in the gate oxide and can results in significant noise power density reduction, as previously demonstrated experimentally.

receives, digitizes, and delivers the output voltage V_{OUT} to a processing unit, which analyzes, displays, and stores the fluorescence measurement.

In this work, an LIA structure is used, which is a standard method to increase detection precision in a noisy environment and in the presence of other wavelengths. An LIA can even detect a target signal with a negative SNR. Fig. 4.3 presents a transient waveform showing how the corresponding amplitude of a target signal buried in noise can be extracted with an LIA system. As shown in Fig. 4.3 (a), the input signal includes an AC signal with 10 pA amplitude and 1 kHz frequency overshadowed by noise. The TIA amplifies the input signal buried in noise, as shown in the next waveform (Fig. 4.3 (b)). Then, the output of the mixer demonstrates the demodulated signal (Fig. 4.3 (c)). Finally, the last waveform (Fig. 4.3 (d)) presents the output of the LPF. It shows a DC voltage that corresponds to the amplitude of the input sine wave signal.

4.4.2. Front-end Module: High-precision TIA

As shown in Fig. 4.4, the sensing PD collects the incoming emission photons and delivers the corresponding current (I_{PD}) plus the dark current (I_{dark}) caused by randomly generated electrons in the depletion region of the PD, in the absence of emission light. The TIA then converts I_{PD} into a voltage signal, which is limited by the input-referred noise, the offset of the amplifier, and the dark current of the PDs. In a high-gain single-ended TIA, a small dark current can cause a large offset voltage at the output [21]. In the proposed design, a differential TIA is utilized to interface with one sensing and one dummy PD. The dummy PD has the same dimensions and shape as the sensing PD and is covered with metal layers to block the emission light. Therefore, the dummy PD does not sense the incident light, but rather generates a dark current similar to that of the sensing PD. The two dark currents cancel out each other's effect within the differential input stage of the TIA. The low-amplitude target signal in low luminescence applications is often overshadowed in large noise and offset signals. Therefore, a high precision amplifier must be used in the input stage to address this issue and to retrieve the incoming input signal. In order to address these drawbacks, noise and offset cancellation techniques such as chopping and auto-zeroing are often employed [89]–[92]. Chopper modulation pushes the signal to high frequencies to mitigate the effect of the flicker noise. However, such a technique necessitates designing a wideband amplifier. Instead, a fully differential front-end TIA based on a switched-biasing ping-pong auto-zeroed technique is used in this design to degrade the input-referred noise and imperfections of the detector. Since the combined ping-pong and switched-biasing schemes do not transfer the target signal to higher frequencies, the proposed structure does not require a wideband amplifier in the front-end, thereby saving power [26]. The performance of the core amplifier is improved using high-performance circuit techniques, such as adaptive biasing and current recycling [93]. As shown in Fig. 4.4, the TIA uses a switched-biasing ping-pong scheme to decrease the 1/f noise and the offset significantly. The TIA includes three identical transconductance amplifiers in the input stage (g_{m1-3}) and one in the output stage (g_{mo}). The input stage has three phases. During each time interval, the output of one input transconductance is connected to

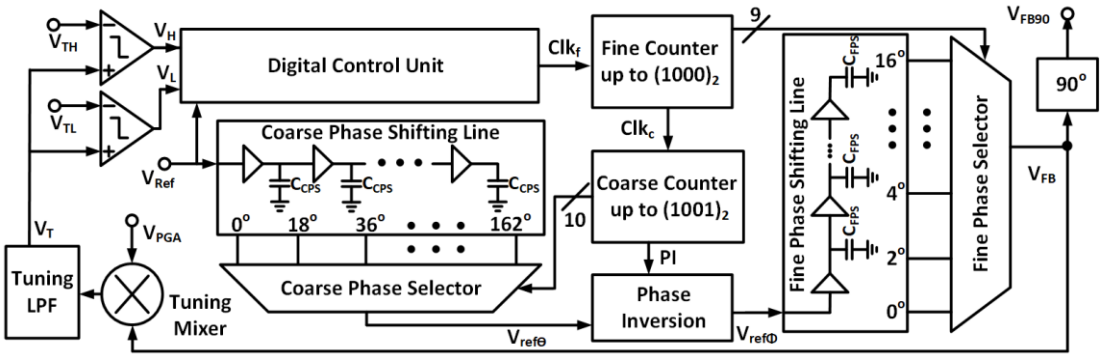

Fig. 4.6. Block diagram of the phase detection feedback module, which samples the output signal of the PGA and then compares its phase with the phase of the reference signal (V_{ref}) by using two comparators and the DCU. Two coarse and fine phase shifting lines then generate a signal that has the same phase and frequency as V_{PGA}, which is called V_{FB90}.

g_{mo}. Connecting one specific input transconductance to the output stage with resistive feedback (R_f) forms a TIA circuit that delivers an output voltage corresponding to the sensed I_{PD}. Placing a capacitor (C_f) in parallel with R_f improves the phase margin of the TIA to ensure stability [31], [94]. Switching between the three identical input stages, at different complementary phases, allows the TIA to continuously deliver V_{TIA}, while providing switched-biasing to mitigate the effects of the 1/f noise and offset. The presented circuit utilizes the ping-pong auto-zeroing and switched-biasing techniques elaborated in the following subsections.

4.4.2.1. Ping-pong Auto-zeroing

Auto-zeroing is a high-precision technique that compensates for the offset voltage of an amplifier and includes two phases: 1- zeroing phase (Φ_Z) and 2- amplification phase (Φ_A) [26], [95]. To explain the employed auto-zeroing scheme, two out of the three phases shown in Fig. 4.4 must be considered. First, in the zeroing phase, the capacitors at the input nodes of the amplifier (C_Z) sample the amplifier's offset. During the offset sampling phase of one input transconductance (g_m), the corresponding Φ_Z switches are on. This way, g_m, which is in the zeroing phase, has a unity gain, and its input nodes are connected to the bias voltage (V_{CM} = 900 mV). The amplification phase follows the zeroing phase. In the amplification phase, the offset stored in C_Z during the

previous zeroing phase is subtracted from the input nodes' voltage to cancel the effect of the input offset voltage [91]. During the amplification phase of g_m, the corresponding switches (Φ_A) are on. Φ_A switches connect one of the input gm to the output stage (g_{mo}) and PDs. Auto-zeroing is a discrete-time technique and cannot be applied to a single stage for continuous-time applications. Providing a continuous V_{TIA} at the output of the TIA requires the utilization of two input stages, namely, transconductances g_{m1} and g_{m2} (Fig. 4.4), which are forming a ping-pong structure [96]. A ping-pong structure includes two input g_m. Whereas, one transconductance (g_{m1}) is in the zeroing phase, the other stage (g_{m2}) is in the amplification phase. That is, $\Phi_{Z1} = 1$, $\Phi_{A2} = 1$, $\Phi_{Z2} = 0$, and $\Phi_{A1} = 0$, which mean that the Φ_Z switches of the first stage (Φ_{Z1}) are closed, while the other switches of the first stage (Φ_{A1}) are opened; at the same time, the Φ_A switches of the second stage (Φ_{A2}) are closed, and the other switches of the second stage (Φ_{Z2}) are opened. In the next phase, Φ_{Z2} switches are closed to sample the input offset of the second stage (g_{m2}), and Φ_{A1} switches are closed to put the first stage (g_{m1}) in the amplification phase. Such switching between the zeroing phase and amplification phase, in which one input g_m samples the offset and the other cancels the stored offset from the input signal, compensates for the transconductances input DC offset, while the signal is continuously delivered to the output transconductance g_{mo} [95].

4.4.2.2. Switched-biasing

Fig. 4.4 represents the switches and related timing diagram of the three stages. Implementing two stages (i.e. g_{m1} and g_{m2}) realizes a ping-pong structure that can compensate for the effect of the offset voltage. However, the TIA needs to mitigate the ping-pong structure's low-frequency fluctuations and flicker noise. Chopper modulation is a high-precision technique that can compensate the low-frequency noise effect [92], [97]. A chopper-stabilized amplifier first transfers the signal of interest to higher frequencies before it enters the amplifier, and then down-converts the signal after the amplifier. Such an approach can compensate for the flicker noise effect at the cost of more hardware. Pushing

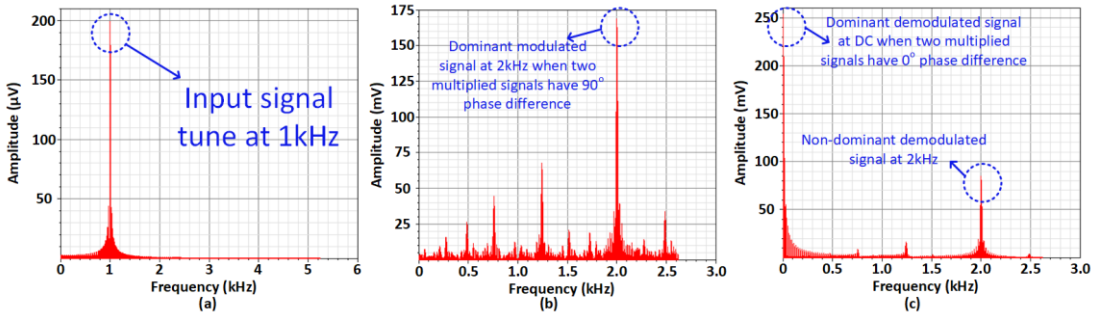

Fig. 4.7. Working concept of the feedback module with simulation results: (a) DFT of the input signal. (b) DFT of the output signal of the tuning mixer when the phase difference is 90° between V_{FB} and V_{PGA}. (c) DFT of the output signal of the output mixer when V_{TIA} and V_{FB90} have 0° phase difference.

the target signal to a higher frequency necessitates the design of a wideband amplifier, which increases the power consumption. Chopping can also add a ripple to the output voltage, which requires further filtering using more circuits [98]–[100]. Thus, a switched-biasing technique is used in this design to efficiently eliminates flicker noise with minimal circuit resources.

The basic concept of this technique is based on switching the input transistors between active and inactive states to eliminate the 1/f noise. As shown in Fig. 4.5 (a) and (b), a transistor alternating between strong inversion (active state) and the cutoff region (inactive state) with a 50% cycle, generates less 1/f noise than a transistor continuously working in strong inversion [101]. Such a switching scheme affects the 1/f noise mechanism inside the transistors physically. Low-frequency noise results from charges trapping in the gate oxide of MOSFETs [102]–[104]. Cycling a MOS transistor between strong inversion and accumulation mode reduces an electron's probability of being trapped and can result in a noise power density reduction of more than 3 dB, as modeled in [102], [104], and observed in [101], [105]. A transistor that continuously works in strong inversion adds continuous noise power to the drain current. In contrast, using switched-biasing resets any additional noise in the drain current by erasing the occupied traps inside the transistor's channel, which decreases the flicker noise itself at the source rather than its effect. Other flicker noise compensation techniques, such as chopper modulation, decrease the flicker noise's effects by using additional signal processing blocks leading to more

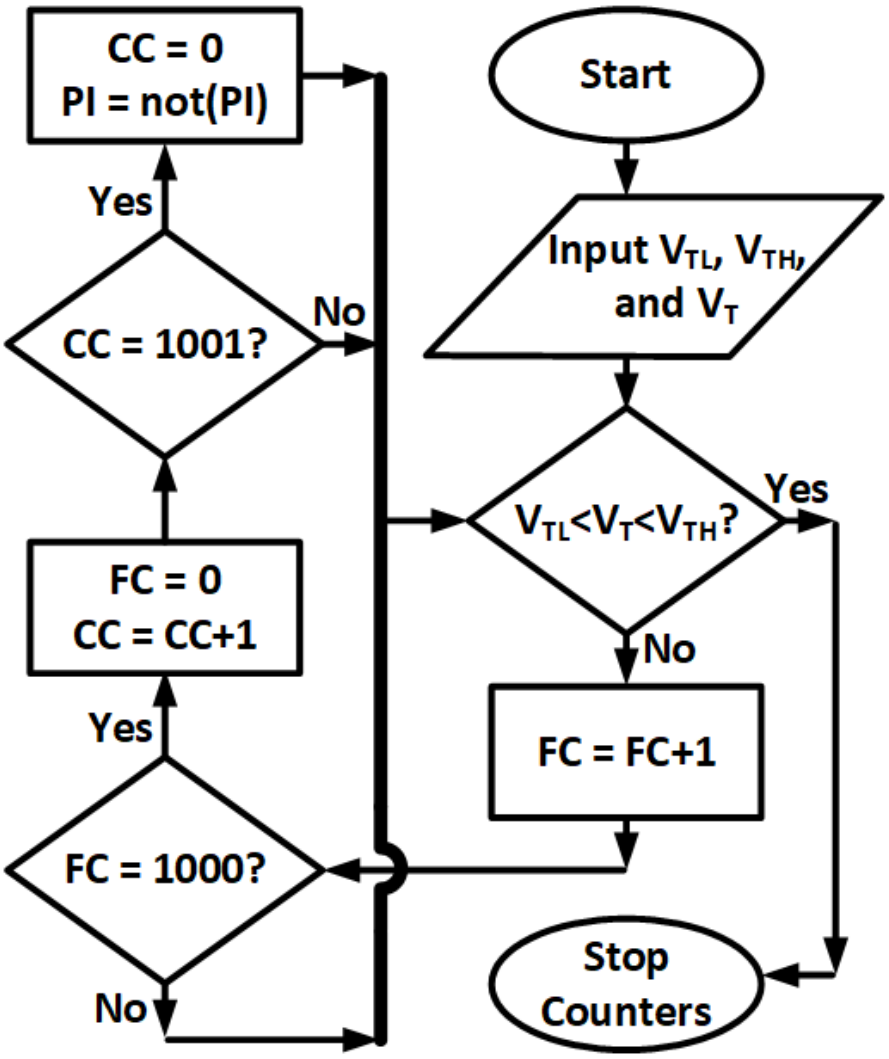

Fig. 4.8. Flowchart of the DCU and counters. Comparators compare the threshold voltages (V_{TL} and V_{TH}) with the output of the tuning filter (V_T). Then, the outputs of the comparators (0 or 1 digital values) go to the DCU. The DCU lets FC and CC count as presented in the flowchart. Once V_T reaches between V_{TH} and V_{TL}, the DCU stops counters and keeps their numbers. These numbers correspond to a delay that is added to V_{ref} to generate V_{FB}.

power consumption, whereas switched-biasing removes the flicker noise itself without using additional signal processing blocks [101]. The switched-biasing technique is utilized in this TIA design as a reset phase (Φ_R), during which all transistors are off, and capacitors are discharged to remove all possible traps, and eliminate flicker noise.

To provide a continuous reading, a third input stage is added to the design in Fig. 4.4. While the first two stages (g_{m1-2}) are put in the amplification and zeroing phases, the third stage (g_{m3}) is put in the reset phase, and all Φ_{R3} switches are closed. This way, the transistors of g_{m3} are disconnected from the source voltage and connected to the ground. The reset phase cycles between different input stages (g_{m1-3}) to remove the flicker noise of each input stage. As shown in Fig. 4.4, g_{m1} starts in the reset phase (Φ_{R1} = 1), while g_{m2} is in the amplification phase (Φ_{A2} = 1) and g_{m3} is in the zeroing phase (Φ_{Z3} = 1). Then, in the second round, g_{m1}, g_{m2}, and g_{m3} turn to the zeroing phase (Φ_{Z1} = 1), reset phase (Φ_{R2} = 1), and amplification phase (Φ_{A3} = 1), respectively. In the third round, g_{m1}, g_{m2}, and g_{m3} are put in the amplification phase (Φ_{A1} = 1), zeroing phase (Φ_{Z2} = 1), and reset phase (Φ_{R3} = 1), respectively. As shown with a timing diagram in Fig. 4.4, such a scheme is provided for all three input stages sequentially to realize a continuous response (V_{TIA}) while removing low-frequency imperfections i.e. offset, distortion and flicker noise.

4.4.2.3. Automatic phase-alignment module

To ensure the LIA can process a weak input signal buried in noise with maximum sensitivity and high SNR, a high-precision phase adjustment strategy is provided to synchronize the reference signal and the modulated input signal together. This design is using a low-power phase-detection feedback scheme that receives both V_{PGA} and V_{ref} and compares their phases to deliver the output feedback signal (V_{FB}). Next, a 90° delay shifts the phase of V_{FB} to generate V_{FB90}, the phase of which is identical to the phase of V_{PGA}. The phase-detection feedback follows the semi-digital automatic phase-alignment feedback scheme reported in [26], [77], operated at 1 kHz. As shown in Fig. 4.6, it consists of a tuning mixer, a tuning LPF, a digital control unit (DCU), two comparators, a fine counter (FC), a coarse counter (CC), a fine phase-shifting line (FPSL), a fine phase selector (FPS), a coarse phase-shifting line (CPSL), a coarse phase selector (CPS), and a phase inversion.

The tuning mixer multiplies V_{PGA} with the feedback signal (V_{FB}), and the resulting voltage goes to the tuning LPF. Similar to Eq. 4.3, such a multiplication generates two tones at the output of the mixer. The one at 2 × f_c adds up together the phases of V_{PGA} and V_{FB}, whereas the one at 0 Hz subtracts the

two phases. The tuning LPF extracts the DC part, which includes the subtracted phases of V_{PGA} and V_{FB}. Once the output DC voltage of the tuning LPF is at zero level, the two multiplied signals are orthogonal. Then, a 90° phase shift is applied to V_{FB} to generate another signal (V_{FB90}), the phase of which is identical to V_{PGA}. According to Eq. 4.3, having an identical phase provides a maximum DC level at the LIA's output (V_{OUT}) and in turn, a maximum sensitivity. Fig. 4.7 presents the working concept using the discrete Fourier transform (DFT) simulation results. As shown in Fig. 4.7 (a), the DFT of the input signal of the LIA has a dominant tone at 1 kHz. Fig. 4.7 (b) presents the DFT of the output signal of the tuning mixer when the phase difference between V_{FB} and V_{PGA} is 90° (quadrature). In this case, the output of the tuning mixer has only one dominant value at 2 kHz, and no DC component exists. The output value of the tuning LPF is zero in this situation. Fig. 4.7 (c) shows the DFT of the output signal of the output mixer when V_{TIA} and V_{FB90} are in-phase. The output mixer has the maximum value at 0 Hz, and another tone at 2 kHz. The output LPF then extracts the DC component.

This design uses a two-step strategy to generate V_{FB} using a coarse and a fine phase shifting applied to V_{ref}. First, the CPSL provides 10 shifted versions of V_{ref}. Given that V_{ref} has a period of 1 ms, every two consecutive outputs of the CPSL have a 100-µs time difference corresponding to an 18° phase shift. The CPS connects the input of the phase inversion block to one of the CPSL's outputs ($V_{ref\theta}$). θ represents the value of the shifted phase in V_{ref} and can be 0°, 18°, 36°, 54°, 72°, 90°, 108°, 126°, 144°, and 162°. The phase inversion block receives $V_{ref\theta}$ at the input and delivers $V_{ref\Phi}$ at the output. When PI = 0, $V_{ref\theta}$ and $V_{ref\Phi}$ are considered to be equal, and to have identical phases. After delivering all 10 versions of $V_{ref\theta}$ from θ = 0° to θ = 162° to the phase inversion block, PI changes from 0 to 1. When PI = 1, the phase inversion block inverts the next $V_{ref\theta}$ and delivers to $V_{ref\Phi}$, which means they have a 180° phase difference. This approach allows the feedback to cover all possible 360° phase differences between V_{PGA} and V_{ref}.

The FPSL generates nine phase-shifted versions of $V_{ref\Phi}$. The output signals of the FPSL have phase shifts from 0° to 16° with a precision of 2°, which means the minimum time difference of the FPSL is 5.55 µs. The FPS connects one of

the outputs of the FPSL to the tuning mixer to compare the phases of V_{FB} and V_{PGA}. If the DCU confirms that V_{FB} and V_{PGA} are in quadrature, then the feedback locks and delivers the corresponding V_{FB} to the output module. Else, if V_{FB} and V_{PGA} do not have a 90° phase difference, the phase selector connects the next output of the FPSL to V_{FB}. If all the FPSL's outputs do not have an orthogonal phase with V_{PGA}, then the following output of the CPSL connects to $V_{ref\theta}$ to generate the subsequent nine outputs of the FPSL. This loop continues until covering all the 10 outputs of the CPSL, representing 180° of the total phase shift. Then, the phase inversion unit inverts the following output from the CPSL and continues the same scheme for all the subsequent 10 outputs of the CPSL. That is, PI is a one-bit digital signal that controls the phase inversion unit. When $V_{ref\Phi}$ reaches the 0° or 162° boundaries, PI changes between 1 and 0. Then, the phase inversion inverts the next $V_{ref\theta}$. Such an approach covers a phase shift interval of 360° with a precision of 5.55 µs in the time domain.

A 2-bit quantizer is responsible for finding the ground level (900 mV) of the tuning LPF [106]. The extracted voltage of the tuning LPF (V_T) is fed to a 2-bit quantizer that includes two comparators made of high-gain op-amps. The comparators compare V_T with high (V_{TH}) and low (V_{TL}) threshold voltages, and drive the DCU with the results. This way, the proposed feedback can recognize when the output DC voltage of the tuning LPF is in the range of the ground level. The DCU stops the counters from counting once the DC voltage reaches a value between V_{TH} and V_{TL}. From the dynamic model of the loop, increasing the difference between V_{TH} and V_{TL} improves the locking time, but causes a high phase error [77]. Designing a low-offset comparator and a voltage difference of 80 mV between V_{TH} and V_{TL} results in a phase error of less than 2° [77], which is the precision of our phase-detection feedback module.

As shown in Fig. 4.6, the counters derive the phase selectors and change the V_{FB} signal. Based on the comparators' results, the DCU enables the FC to count up to $(1000)_2$ by the rising edge of the Clk_f (fine clock) signal. Each time FC reaches $(1000)_2$, a Clk_c signal (coarse clock) enables the CC to add to its previous value. The CC goes to zero and inverts the PI value when it reaches $(1001)_2$. A flowchart describing such a digitally controlled feedback is presented in Fig. 4.8.

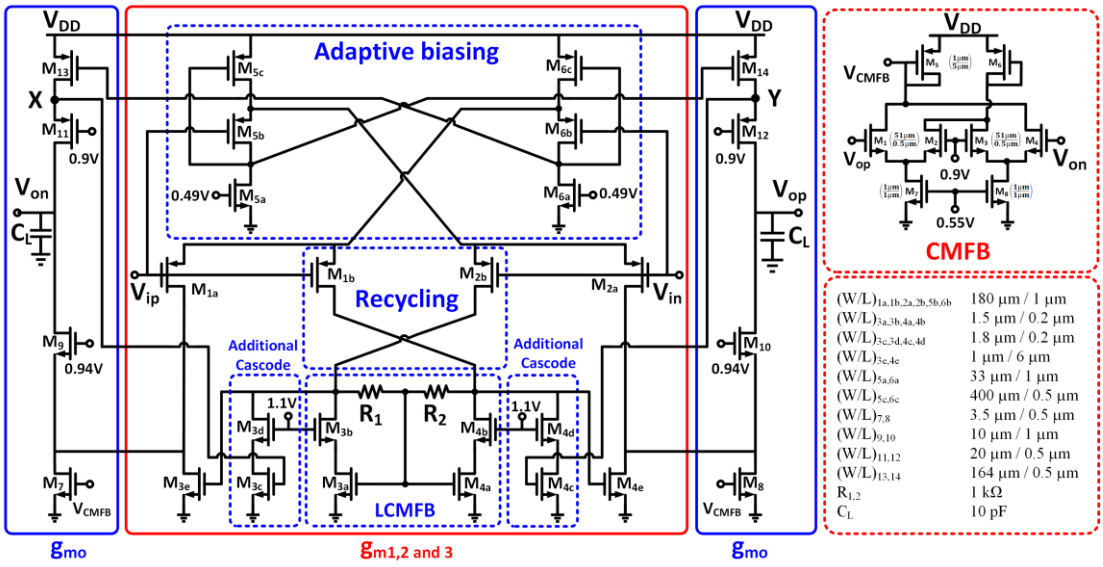

Fig. 4.9. Schematic of the transconductance used for $g_{m1\text{-}3}$ and g_{mo}. The transconductance uses a modified folded-cascode op-amp with adaptive biasing and current recycling, and with an additional cascode stage to improve the output impedance and gain. The right-hand side of the figure includes the schematic of the CMFB circuit and a summary of the sizes and values of all components.

4.5. Circuit Design

4.5.1. Linearized Folded Cascode Amplifier

Low-power OTAs are effective signal conditioning building blocks widely used in battery-operated sensing devices [107]–[111]. The folded cascode OTA is a widely used OTA topology, either as a single-stage amplifier or as the first stage in multistage systems [112]. This topology offers a good trade-off between gain and signal swing [93]. Folded-cascode OTAs using PMOS differential input transistors are often preferred over the NMOS differential inputs due to their lower flicker noise, higher nondominant poles, and lower input common-mode level compatible with single NMOS switches in SC applications [113]. A differential input pair can robustly reject common-mode and power-supply noise [114]. The selection of an appropriate OTA topology is dictated by the requirements of our application. When performing optical measurements, a wide input common-mode range (ICMR) is necessary to accommodate different light's beam power and keep the OTA in the linear range. Various techniques,

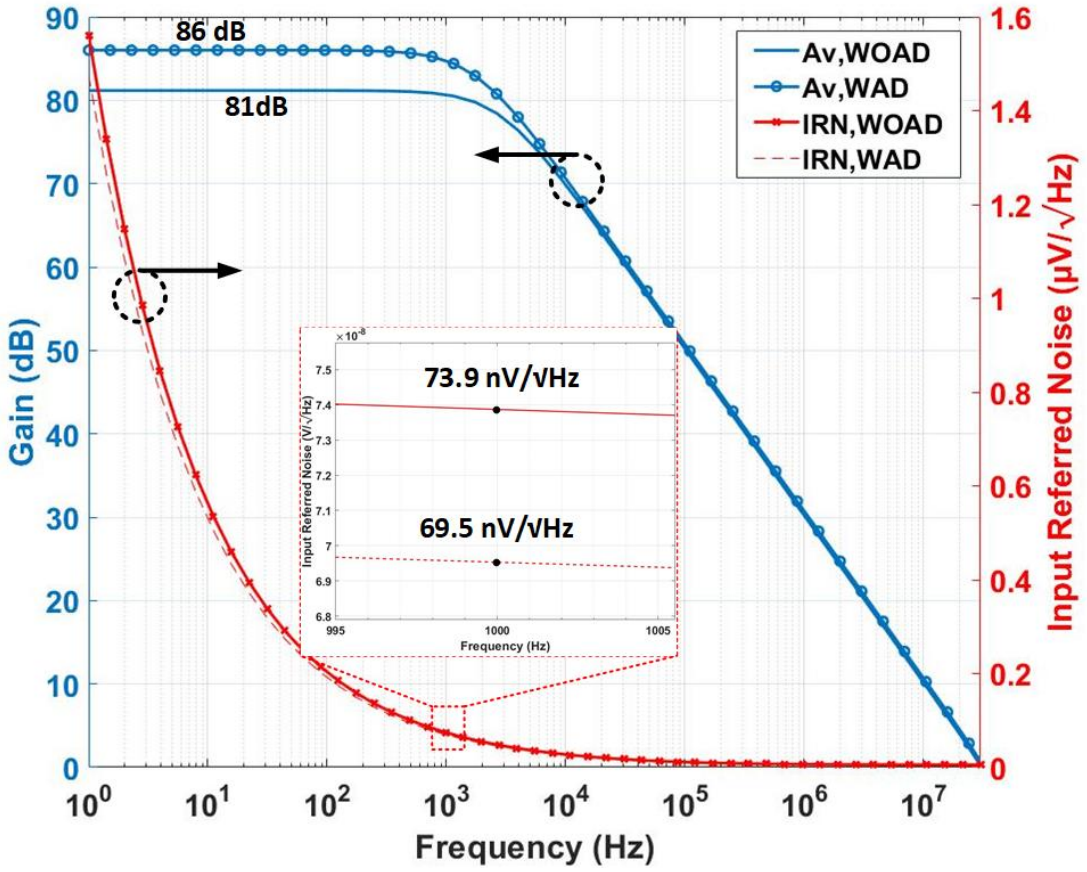

Fig. 4.10. Comparison between the simulation results of the OTA circuit without and with ADs. The former as less input-referred noise and more gain.

such as multipath active current mirrors [115], [116], current boosting [117], self-cascode transistors [118], cross-coupling topology [119], adaptive biasing [119], [120], source degeneration [120]–[122], and bulk-driven techniques [123], [124], have been used to improve the transconductance linearity of the input transistors. In [120], the authors combined a source degeneration approach with an adaptive biasing technique to improve the linearity. The power-hungry current sources at the folding stage can drive large currents without providing any transconductance for the OTA and limiting the slew rate (SR) [113]. To address this issue, recycling folded cascode (RFC) OTA can improve GBW and SR [113], [125]. In the presence of large AC signals, variations in bias currents in the recycling stage make the RFC topology nonlinear. To troubleshoot the problem, a super class-AB topology was proposed to separate DC and AC currents via local common-mode feedback (LCMFB) [126]. Adaptive biasing benefits from a flipped voltage follower (FVF)

circuit, which is providing a high ICMR by increasing the headroom voltage. Given two FVFs in Fig. 4.9, ICMR is calculated as follows:

$$V_{DD} - (\alpha) < V_{cm,i} < V_{DD} - (\beta), \tag{4.5}$$

where α and β are defined as follows:

$$\alpha = \left|V_{thp,5b,6b}\right| + \left|V_{thp,5c,6c}\right| + \sqrt{\frac{2I_{D,5c,6c}}{K_p\left(\frac{W}{L}\right)_{5c,6c}}}, \tag{4.6}$$

$$\beta = \left|V_{thp,5b,6b}\right| + \sqrt{\frac{2I_{D,5b,6b}}{K_p\left(\frac{W}{L}\right)_{5b,6b}}} + \sqrt{\frac{2I_{D,5c,6c}}{K_p\left(\frac{W}{L}\right)_{5c,6c}}}, \tag{4.7}$$

where K_p and V_{thp} denote the parameter $\mu_p C_{ox}$ and the threshold voltage of PMOS transistors, respectively. Substituting Eqs. 4.6 and 4.7 in Eq. 4.5 gives the minimum value of the supply voltage ($V_{DD,min}$).

$$V_{DD,min} = \left|V_{th,5b,6b}\right| + V_{SD,5b,6b} + V_{SD,5c,6c}. \tag{4.8}$$

The role of the current recycling sub-circuit made of M_{1b} and M_{2b} is to provide an auxiliary path to utilize standard folded transistors (M_{3e} and M_{4e}) as an active current source. LCMFB is applied to increase the linearity of transistors M_{3e} and M_{4e} in the presence of large input signals at their gates [93]. Resistors R_1 and R_2 remove the AC signal from the drain current of M_{3a} and M_{4a} by generating an associated common-mode voltage at their gates. Therefore, in the presence of large AC signals, the drain currents of M_{1b} and M_{2b} remain constant. The utilization of adaptive biasing, recycling, and LCMFB improve the linearity and enhance the performance of the transconductor in terms of SR and GBW. In addition to the aforementioned techniques, two additional cascode (AD) circuits are used in the design presented in Fig. 4.9, in parallel with the LCMFB circuit to increase the gain. Sampling the signals at nodes X and Y, creates a differential auxiliary path to the output via amplification of the in-phase signals. Eqs. 4.9 and 4.10 can be used to compare the OTA gains with and without the ADs:

$$A_{v,WOAD} = -2.\, g_{m,1a}\left(1 + A_{v,Recycling}\right)R_{out}, \tag{4.9}$$

$$A_{v,WAD} = A_{v,WOAD} + A_{v,cascode}, \tag{4.10}$$

where $A_{v,WOAD}$, and $A_{v,WAD}$ are the gains of the OTA without and with ADs, respectively. The values of R_{out} and $A_{v,recycling}$ are given by [93]:

$$R_{out} \approx r_{o13} r_{o11} g_{m11} || g_{m9} r_{o9} r_{o7}, \tag{4.11}$$

$$A_{v,Recycling} = g_{m3e}(r_{o2b} || R_{1,2}), \tag{4.12}$$

where $R_{1,2} \ll r_{o2b}$. The value of $A_{v,cascode}$ is a function of V_x:

$$V_x = \frac{A_{v,WAD} V_{ip}}{g_{m11} R_{out}}, \tag{4.13}$$

where $V_{on} = A_{v,WAD} V_{ip}$. Thus, $A_{v,cascode}$ can be calculated as follows:

$$A_{v,cascode} = \left(\frac{A_{v,WAD}}{g_{m11} R_{out}}\right)\left(g_{m3c}(r_{o2b} || R_{1,2} || (r_{o3c} r_{o3d} g_{m3d}))\right)\left(g_{m3e} R_{out}\right), \tag{4.14}$$

$$A_{v,cascode} = \left(\frac{A_{v,WOAD} + A_{v,cascode}}{g_{m11} R_{out}}\right)\left(g_{m3c} R_{1,2}\right)\left(g_{m3e} R_{out}\right), \tag{4.15}$$

$$A_{v,cascode} \approx A_{v,WOAD} \times \frac{g_{m3c} g_{m3e} R_{1,2}}{g_{m11}}. \tag{4.16}$$

Hence, the total gain of the presented OTA is doubled as follows:

$$A_{v,WAD} \approx A_{v,WOAD}\left(1 + \frac{g_{m3c} g_{m3e} R_{1,2}}{g_{m11}}\right). \tag{4.17}$$

As shown in Fig. 4.10, the $A_{v,WOAD}$ and $A_{v,WAD}$ are about 81 and 86 dB, respectively, which corresponds to a gain improvement of 77%. A DC analysis of the circuit shows that the DC voltages at nodes X and Y are large, making transistors M_{3c} and M_{4c} entering the triode region. In consideration of the large voltage at their gates, the dimensions of M_{3c} and M_{4c} must be selected to allow sinking large currents. Accordingly, the ADs can sink DC currents of 15 μA, which represents only 6% of the total power consumption. According to the noise simulation, as demonstrated in Fig. 4.10, the input-referred noise (IRN)

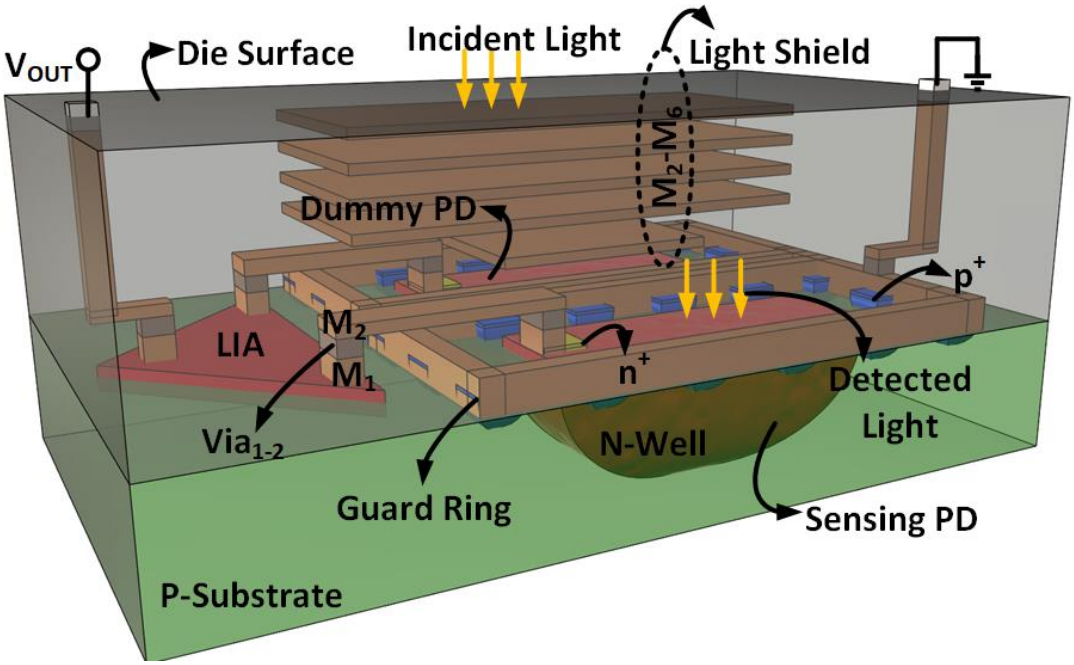

Fig. 4.11. Isometric view of the implemented sensing and dummy PDs.

at 1 kHz shows an improvement of 4.4 nV/√Hz, or 6%. On the contrary, the noise seen at nodes X and Y is added to the output.

4.5.2. Dummy and Sensing PDs

In this design, two integrated PDs are utilized to provide a fully differential structure, as shown in Fig. 4.11. The dummy PD is covered with different layers of metal (M_2–M_6) to block the incident light from reaching the surface of the dummy PD, while the other PD can detect the incident light. Such a differential structure minimizes the effect of dark current and removes the resulting DC offset effect, which increases the sensitivity. The implemented PD employs an n-well and a p-substrate to make a reverse-biased diode, the incident light power of which results from the movement of the electrons and generates a current proportional to the incident light. Such PD design benefits from a deep n/p junction, which improves the light collection efficiency, and provides small parasitic capacitance, which results in an enhanced charge for the voltage conversion ratio [21]. The parasitic capacitance of the PD (C_{PD}), which directly determines the size of the feedback capacitance (C_f) [31], consists of a bottom plate junction capacitance (C_j) and a sidewall capacitance (C_{jsw}). Assuming that

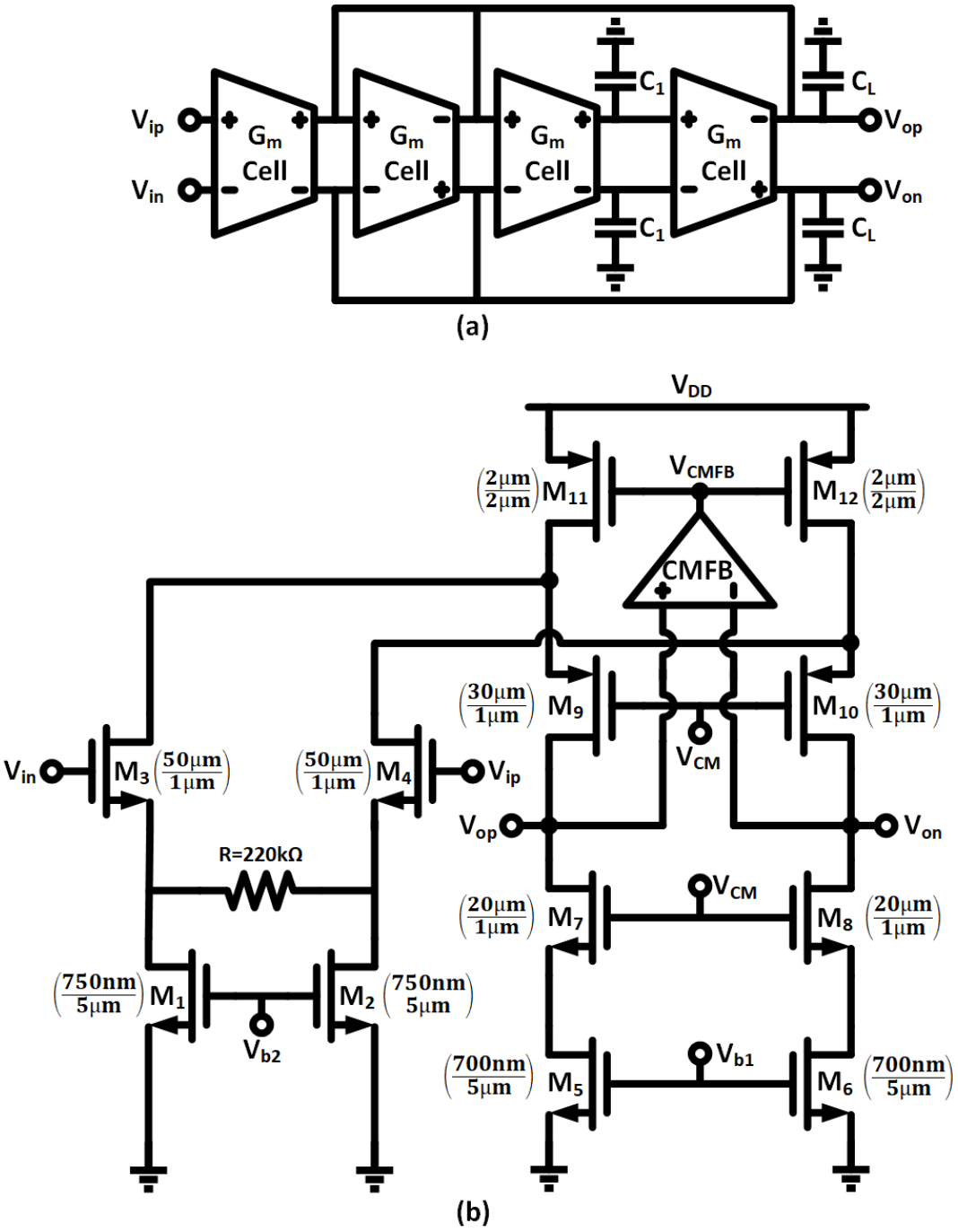

Fig. 4. 12. (a) Block diagram and (b) Gm-cell schematic of BPF.

the PD has an area of A_{PD} and a perimeter of P_{PD}, the total parasitic capacitor can be calculated as follow:

$$C_{PD} = C_j A_{PD} + C_{jsw} P_{PD}. \tag{4.18}$$

Considering C_j = 1.34104 F/m^2 and C_{jsw} = 5.331010 F/m values in 0.18-µm CMOS technology [38], the designed PD with a dimension of 200 µm × 200 µm

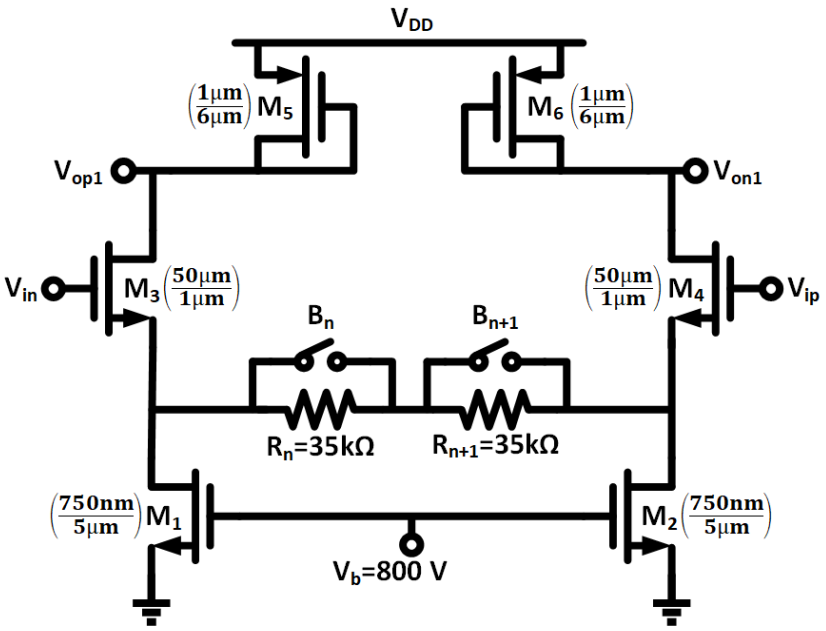

Fig. 4.13. One-stage PGA unit with switches B_n and B_{n+1}.

has an approximate capacitance of C_{PD} = 0.6 pF. Finally, the generated current goes to the input blocks of the LIA through multiple n+ connections and the second metal layer (M_2). The two PDs are placed side by side and are each supported with a grounded guard ring that uses the first metal layer (M_1) connected to p-substrate with p^+ connections in order to avoid any digital

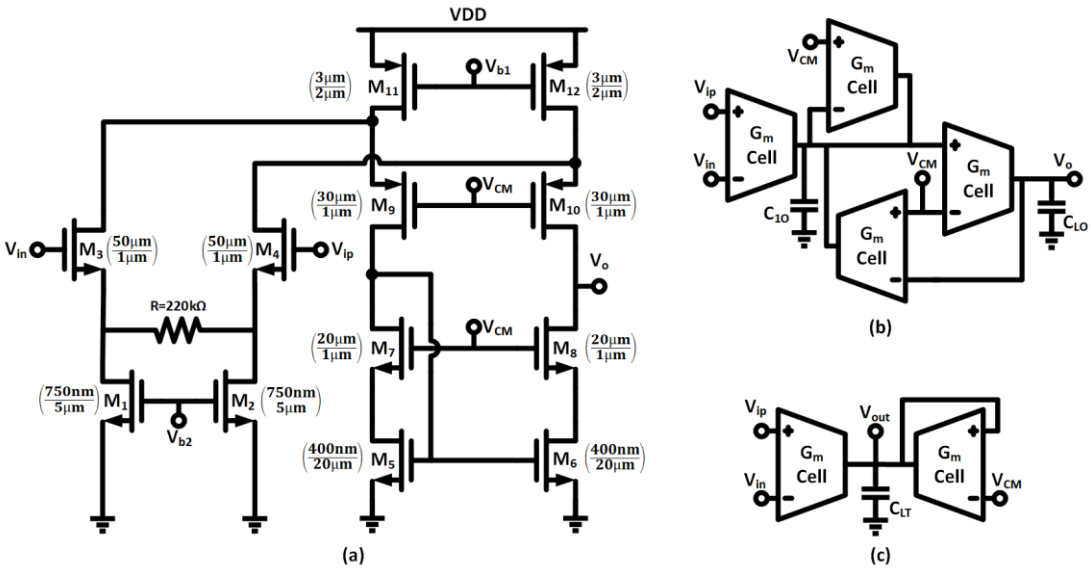

Fig. 4.14. (a) Gm-cell schematic of LPFs. (b) Block diagram of the output LPF. (c) Block diagram of the tuning LPF.

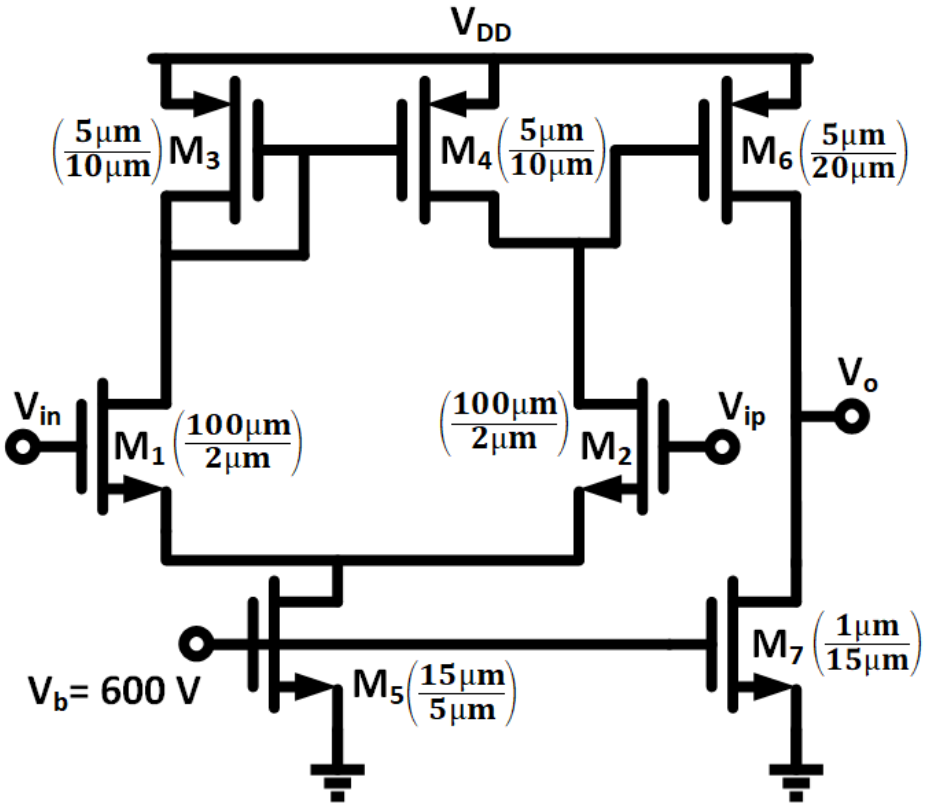

Fig. 4.15. Comparator schematic.

spikes, supply noise, substrate-induced noise, and light diffusion to the dummy PD [21], [127].

4.5.3. BPF, Tuning LPF, and output LPF

The BPF attenuates the high-frequency noise and offset from the input signal of interest. The block diagram of the designed BPF is shown in Fig. 4.12 (a). Fig. 4.12 (b) presents the Gm-cell schematic of the BPF, and the size of each transistor is shown besides each MOSFET. The simulation results show that the designed BPF has a center frequency of 1 kHz with 0 dB gain when C_1 = C_{LBPF} = 800 pF.

Fig. 4.13 (a) presents the Gm-cell schematic of the utilized transconductance for the LPFs, and the size of all transistors. The output LPF is a second-order LPF, as shown in Fig. 4.13 (b), to extract the output DC voltage of the LIA. The tuning LPF, as depicted in Fig. 4.13 (c), is a first-order LPF to extract the phase difference between V_{PGA} and V_{FB}. C_{1O} and C_{LO} are both equal to 25 nF, and the load capacitance of the tuning LPF (C_{LT}) is equal to 150 nF; they are all off-chip

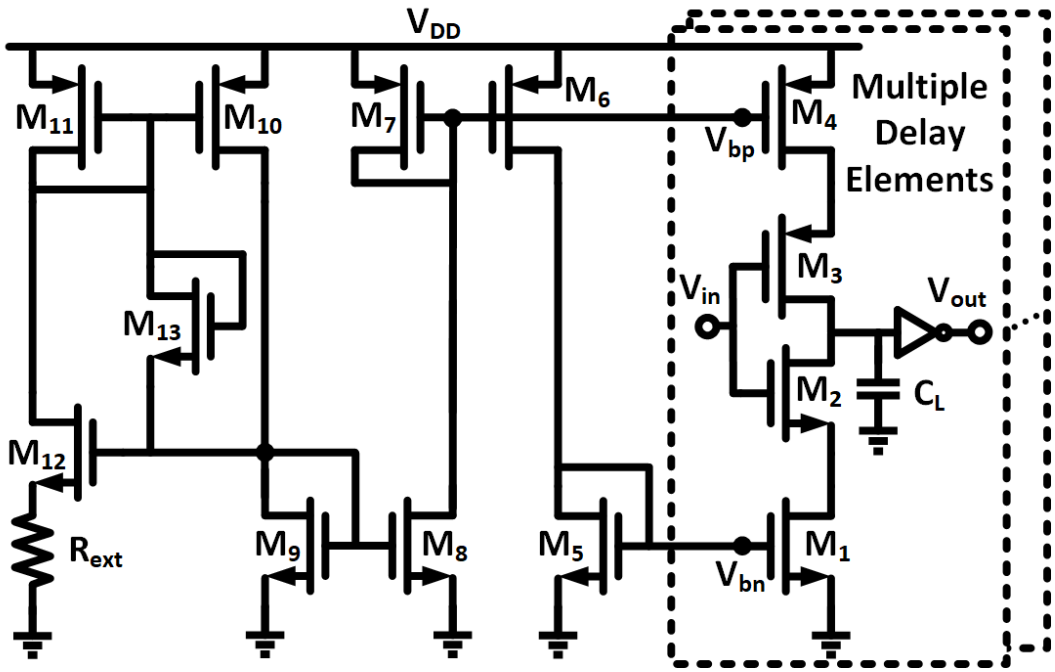

Fig. 4.16. Schematic of delay elements tuned using control transistors (M_1 and M_4) and current mirrors for controlling the current of M_1 and M_4.

capacitors. Fig. 4.13 (a) presents the G_m-cell schematic of the utilized transconductance

4.5.4. Programmable gain amplifier (PGA)

The PGA consists of two different gain stages in series that are added to the design to increase the dynamic range of the incoming signal. The schematic of the core amplifier of each stage and the size of all transistors are shown in Fig. 4.14. Given B_n and B_{n+1}, each stage has a 2-bit programmable switch. Therefore, the two PGA stages in series have five different gain levels, varying from 8 dB to 70 dB.

4.5.5. Comparator and Digital Units

The schematic of the comparators, which includes an open-loop two-stage OTA, and the size of the transistors, are shown in Fig. 4.15. Each comparator is also followed by an inverter chain to drive the digital gates of DCU. The input-referred offset voltage of the comparator is designed to be less than 1 mV. The comparators compare the output value of the tuning LPF (V_T) with two threshold voltages, i.e. V_{TH} and V_{TL}. The DCU includes digital gates (NAND, NOR, and

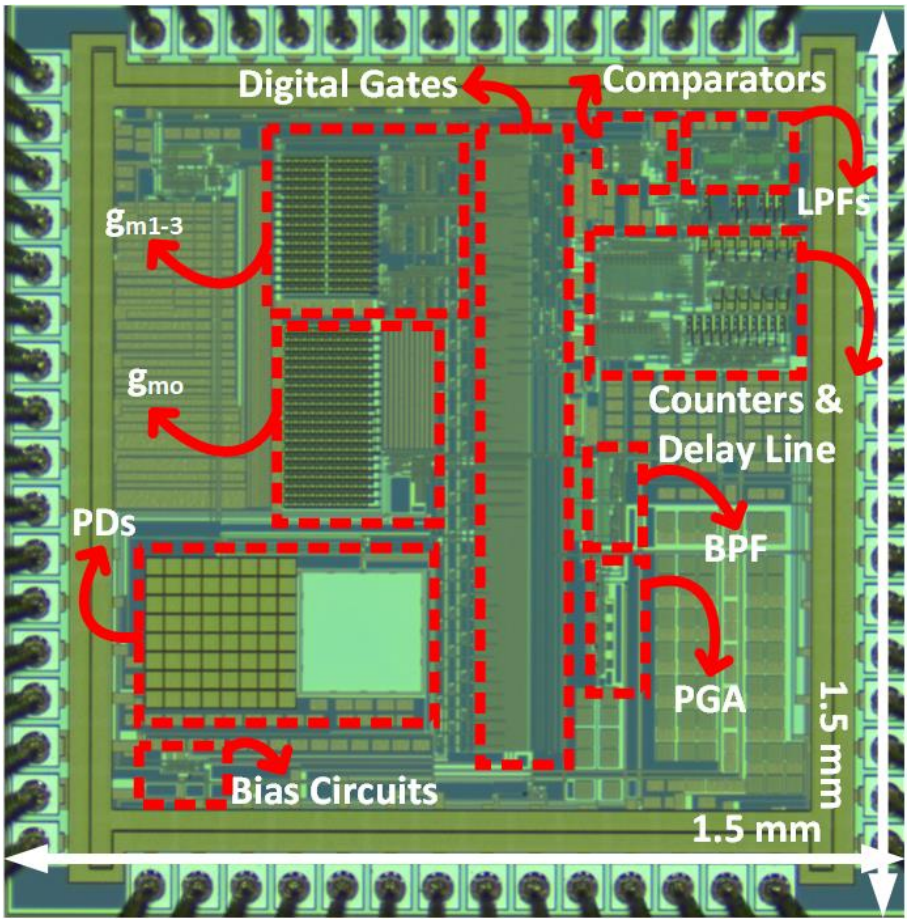

Fig. 4.17. Chip picture showing the layout of different building blocks of the presented LIA fabricated in 0.18 µm CMOS technology with dimensions of 1.5 mm × 1.5 mm.

XOR gates) to detect ones or zeros at the output of the comparator, and to decide to continue or to stop counting. The counters include flip-flops to count up to $(1000)_2$ in FC and $(1001)_2$ in CC. Fig. 4.8 presents a flowchart of the DCU and counter.

4.5.6. Delay elements

The delay can be generated using an inverter followed by a tunable capacitor [128]–[131]. The multiplication of the inverter's output resistance and load capacitance generates the required delay. Targeting 5.5 µs delay in this work necessitates a large capacitor, promoting the utilization of an off-chip capacitor. Multiple delays inside the FPSL and the CPSL blocks require multiple off-chip capacitors, consuming large areas. Another approach to precisely control the delay of an inverter is to add two extra transistors to control the output current

Table 4.1 Performance Summary and Comparison of OTA

Reference/Year	JSSC'00 [104]	JSSC'05 [115]	TCAS'12 [100]	TCAS'13 [114]	TCAS'16 [101]	JSSC'18 [82]	TCAS'21 [102]	This Work
Technology (µm)	0.8	0.18	0.5	0.35	0.18	0.5	0.18	0.18
Supply Voltage (V)	2	0.5	±1.25	1	0.7	±1	±0.75	1.8
Load Cap. (pF)	1000	20	12	15	20	70	100	20
SR^+/ SR^- (V/µs)	0.36*	-	2.7/3.3	2.53/1.37	1.8/3.8	13.2/25.3	4/4.5	4/3.5
Positive/ Negative Settling Time (ns)	3.6*	-	-	224	1300/1000	120/100	9.5/1.6	48.7/47.2
DC Gain (dB)	>100	62	63.4	88.3	57.5	76.8	46	81
PM	51˚	60˚	83˚	66.1˚	60˚	75.1˚	90˚	60˚
GBW (MHz)	1	10	4.9	11.67	3	3.4	0.038	32.5
CMRR (dB)	-	74.5	80	40	19	112	106	165
PSRR (dB)	-	81.4	67.3	40	52.1	92	47	100
Power (µW)	0.43	75	437.5	197	25.4	100	1.8	263
Input Referred noise (nV/√Hz)	-	225 @10 kHz	-	<60 @1 MHz	100 @1 MHz	23 @1 MHz	71.4 @38 kHz	40.6 @1 kHz
FOM (MHz.pF/mW)**	2347	923	134	889	2361	2380	2111	2471

*Average value

**FOM = GBW × (Load Cap. / Power)

(as shown with M_1 and M_4 in Fig. 4.16). The technique is also known as the current starving method. Lowering V_{bn} and increasing V_{bp} increase the effective drive resistance of the inverter, and thus increase the delay. Such a method can help reducing the size of the capacitor, so it can be implemented on-chip. To control these transistors, a current mirror, which is controlled by a reference voltage, is designed, as shown in Fig. 4.16. Lowering the current of the delay element and increasing the output resistance, which allows the design to use a smaller capacitor to provide the required delays.

4.5.6.1. CPSL

This building block receives the reference signal and then generates and delivers 10 different versions of V_{ref}, each delayed by 18° from each other, and provided to the next section through a multiplexer unit (CPS). The selector module chooses the required delay on the basis of the output number of the CC. The coarse delay unit includes nine delay elements in cascade. The first delay element receives V_{ref} with 0° delay and delivers the subsequent output with 18° delay. Afterward, each delay element receives the previously delayed

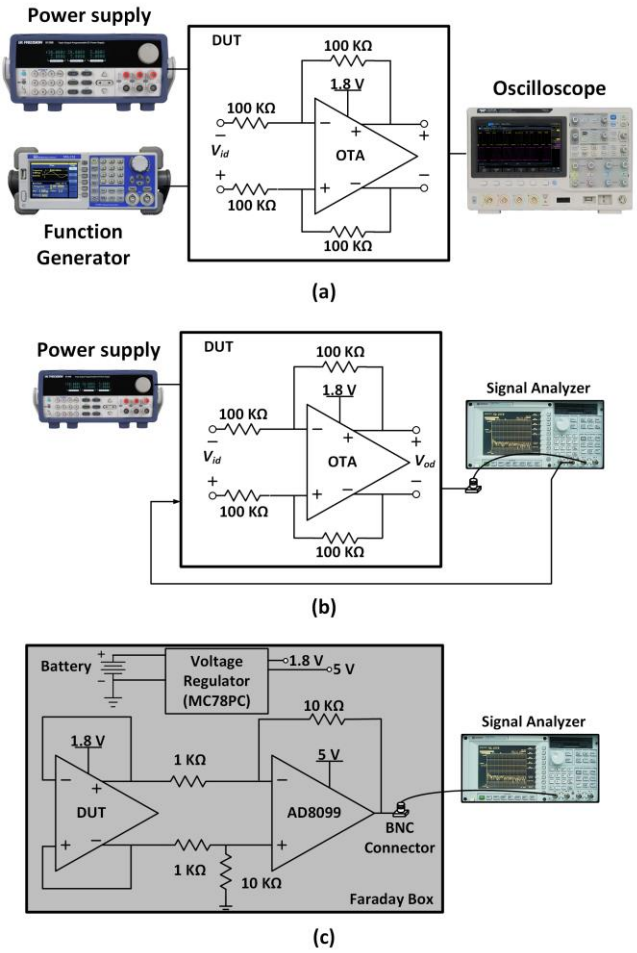

Fig. 4.18. Test setups for the DUT: (a) Time-domain measurements (b) Frequency response measurements (c) Noise measurements.

signal and provides the next delayed signal of the CPSL's output. All delay elements have a CL equal to 150 fF.

4.5.6.2. FPSL

This building block receives the output of the phase inversion at each time and applies smaller delays. These fine delayed signals are each separated by a 2° phase difference and provide a precise signal to be multiplied with V_{PGA}. The C_L of all delay elements in the FPSL block equals 250 fF.

4.5.6.3. 90° Delay

This unit uses the same CPSL circuit to apply a 90° delay to the V_{FB} of the phase-detection feedback and providing V_{FB90}.

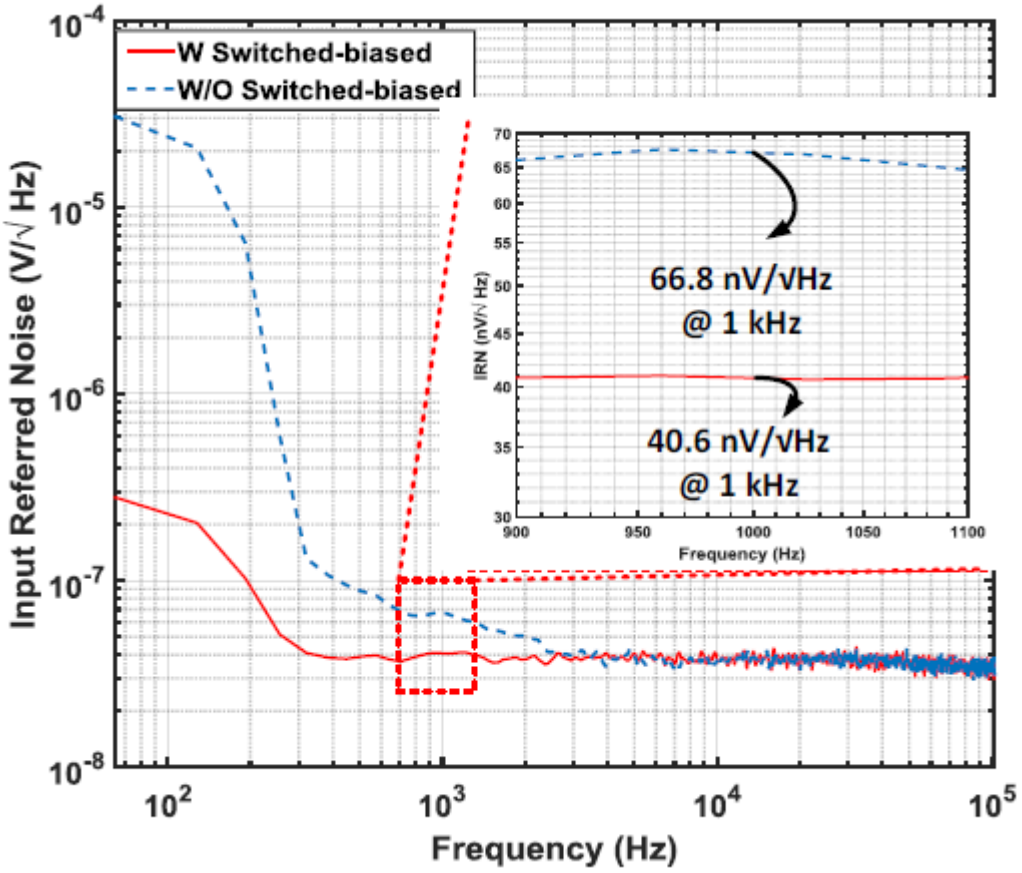

Fig. 4.19. Effect of Switched-biasing technique on low-frequency noise.

4.6. Chip Measurement Results

The proposed LIA and PDs are designed and fabricated in a 0.18-µm CMOS technology. Fig. 4.17 shows a microphotograph of the fabricated chip, which has an area of 2.25 mm^2, including the PDs, LIA circuits, fillers, and pads. The two PDs have an area of 0.15 mm^2, and the sensing area of each PD has a dimension of 200 µm × 200 µm. The pads with ESD protection circuits have an approximate area of 0.96 mm^2. The main circuits, as depicted in Fig. 4.17, occupy an area of 0.6 mm^2, and the rest of the area is occupied by fillers. The joint area of the LIA and PDs that forms a fully integrated fluorescence cell photometer is 0.75 mm^2. This area includes the $g_{m1\text{-}3}$ and g_{mo} of the proposed switched-biasing ping-pong auto-zeroed TIA. The layout also includes LPFs, BPF, bias circuits, digital gates, comparators, delay lines, and PGA. To show the design performance, all blocks are first tested and measured individually in

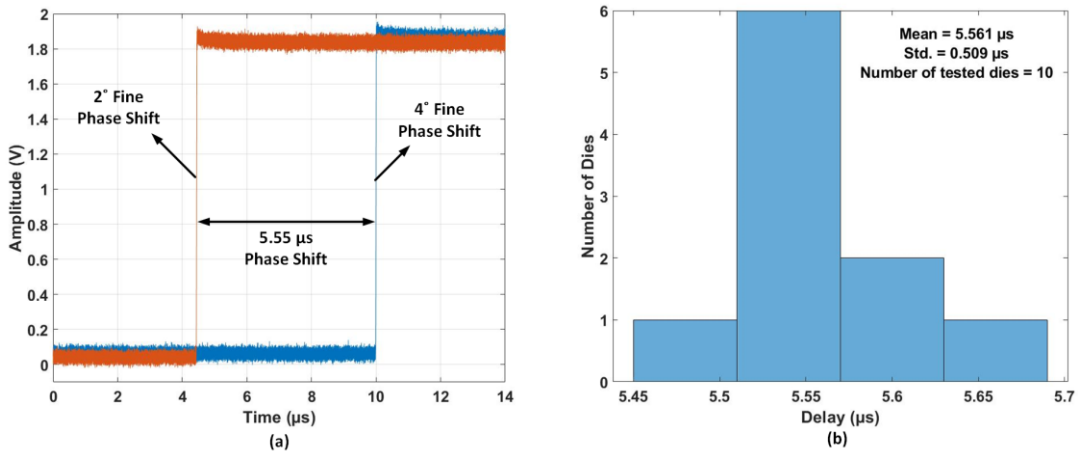

Fig. 4.20. (a) Result of two consecutive outputs of fine phase shifting. (b) Histogram of the measured fine delays for 10 dies, presenting an average value of µs and standard deviation of µs.

the lab. Then, the overall electrical and optical performance of the LIA is measured.

Table 4.1 shows the performance summary of the OTA and a comparison with other designs. For the time-domain measurements of the core amplifier [93], as shown in Fig. 4.18 (a), a power supply is utilized to power up the circuit, a function generator provides the input pulse or sine wave, and an oscilloscope measures the output signal. First, the amplifier's positive and negative SR, as well as the settling time, are measured with a unity gain amplifier in response to an input pulse wave at 1 kHz. As mentioned in Table 4.1, the core amplifier consumes 263 µW, the SR+ and SR− are 4 and 3.5 V/µs, respectively, and the settling time is 48.7 ns, which is adequate for low-frequency fluorescence measurement applications [132]. Fig. 4.18 (b) shows the measurement setup for frequency-domain measurements [133]. The results indicate that the proposed amplifier has a CMRR of 110 dB and a PSRR of 89 dB at 1 kHz. To measure the input-referred noise, the fabricated chip mounted on a test PCB and powered up with a battery, is placed in a shielded box, isolated from EMI, as shown in Fig. 4.18 (c) [134]. Then, the output signal of the device under test (DUT) is amplified with a gain of 20 dB and captured with a signal analyzer (35670A from Keysight, Santa Rosa, CA, US). The measured input-referred noise of the amplifier at 1 kHz is 40.6 nV/√Hz, as shown in Fig. 4.19 and listed in Table 4.1. Then, the amplifier's noise with and without the switched-biasing

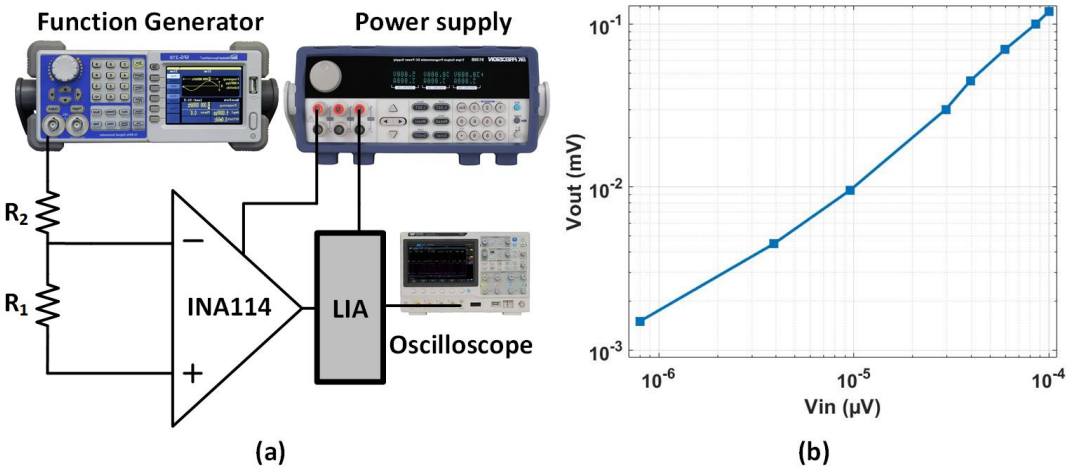

Fig. 4.21. (a) Electrical measurement setup of the LIA, (b) Output voltage versus input voltage.

technique is measured (Fig. 4.19), showing the effectiveness of the utilized method to attenuate the low-frequency noise. The utilized technique decreases the low-frequency input-referred noise by 26.2 nV/√Hz at 1 kHz, which

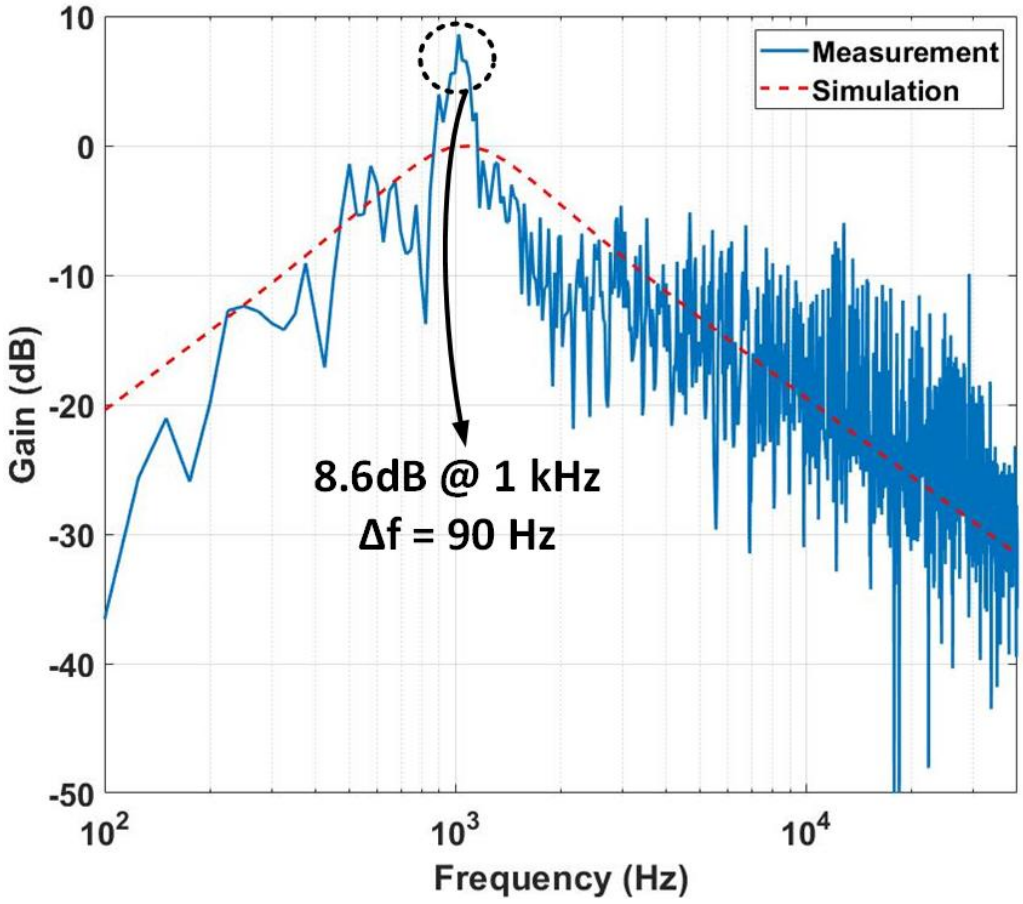

Fig. 4.22. Measured and simulated frequency response of the BPF.

Table 4.2 Performace Summary and Comparison of LIA

Reference/Year	TBCAS'10 [69]	Sensors'16 [71]	JSSC'16 [72]	Sensors'17 [73]	JSSC'21 [75]	This Work
Supply Voltage (V)	3.3	1.8	3.3	±12	3.3	1.8
Technology (µm)	0.35	0.35	0.35	Discrete Components	0.35	0.18
Silicon Area (mm^2)	1.5	8	6	-	4.5	0.65
Frequency (kHz)	20	2.5-25	200	1000	1000-10000	1
Input Range	500 nA-3 µA	35-700 nV	1–30 µm	25 µV–10 mV 1.15 mW*	50-600 µW*	8 nW-24 µW*
Sensitivity	100 mV/µW	124 kV/V	-	40 V/V 450 mV/mW	0.5A/W	250 mV/µW
Power Consumption (mW)	12.79	2	84	840	277	0.7
Resolution	-	12.5 nV	65 zF	25 µV 2.2 µW*	25 µW*	36 nW*
Dynamic Reserve (dB)	1.31	34	-	-	-	42

*Optical Power

corresponds to an improvement of 39%, without increasing the power consumption, and while slightly increasing the area by 15%, which is mainly due to the addition of the auto-zeroing capacitors (CZ = 200 fF). In addition, the conventional FOM [51], as reported in Table 4.1, compares the performance of the OTA with other reports.

The FPSL provides an accurate delay to generate precise V_{FB90}. A delay of 5.5 µs between two consecutive pulse waves is measured as expected (Fig. 4.20 (a)). The capacitor array is implemented with the centroid layout technique to decrease the effect of process variations [38]. To show the effect of mismatch on the delay lines performance, 10 different dies are tested, and the result is presented in a histogram (Fig. 4.20 (b)), which indicates an average delay value of 5.561 µs with a standard deviation of 0.509 µs for the outputs of the FPSL.

The BPF works with a center frequency of 1 kHz, and the LPFs function with a cutoff frequency of 5 Hz. Fig. 4.21 shows the measured BPF frequency response and compares it with the simulation result, which has the same center frequency at 1 kHz. The measurements show a 3 dB bandwidth of 90 Hz for the BPF. The output LPF, tuning LPF, and BPF consume 18, 9.3, and 14 µW power, respectively.

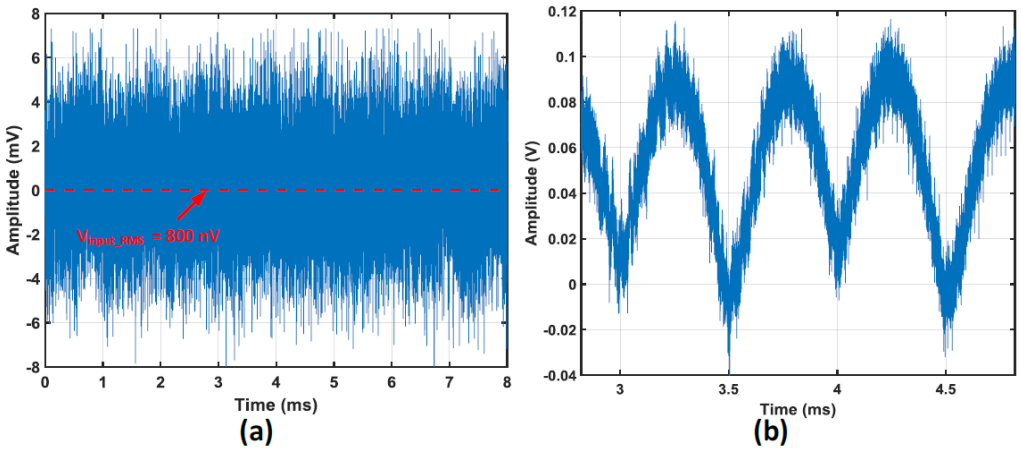

Fig. 4.24. (a) 800 nV input signal buried in 36 µV RMS noise. (b) Mixer's output.

To test the electrical functionality of the proposed LIA, an experimental setup, as shown in Fig. 4.22, is utilized [77], [79], [80]. Two Keysight waveform generators (33600 A) and a resistor divider (R_2 = 40 MΩ and R_1 = 1 kΩ) are used to generate both noise and target signal. An instrumentation amplifier (INA114 from Texas Instruments, Dallas, TX, USA) with a gain of one is used to feed the generated noise and signal into the LIA input. The generated input signal has the same frequency as V_{ref}, which is 1 kHz. In this test, the input

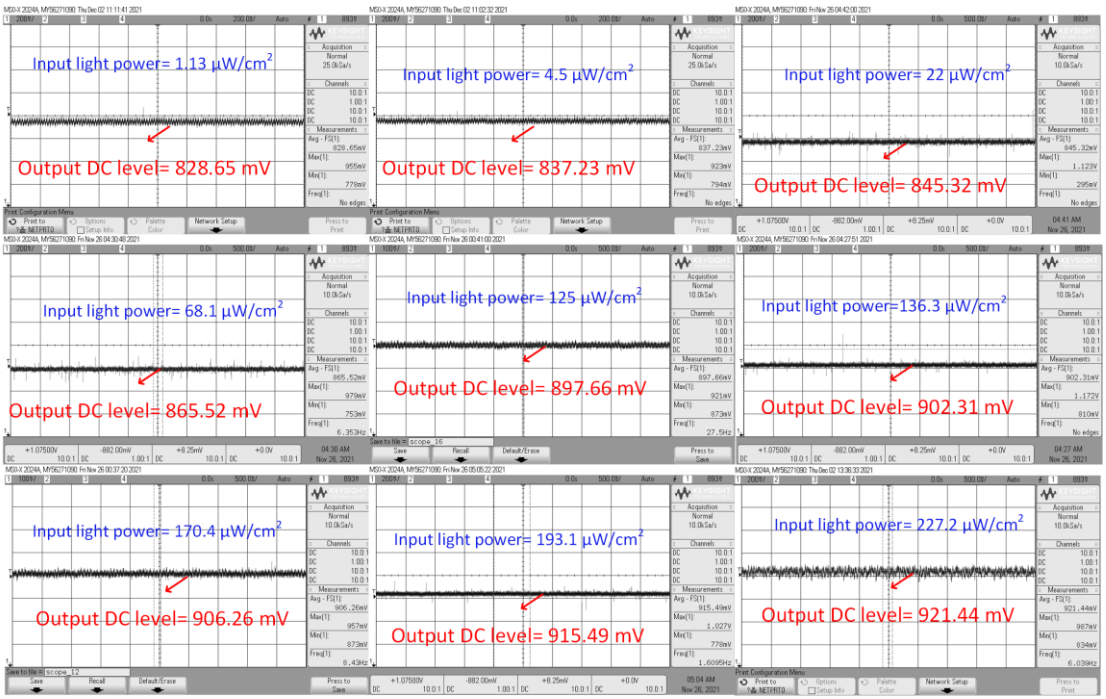

Fig. 4.23. Different measured output DC voltages corresponding to different amplitudes of input light.

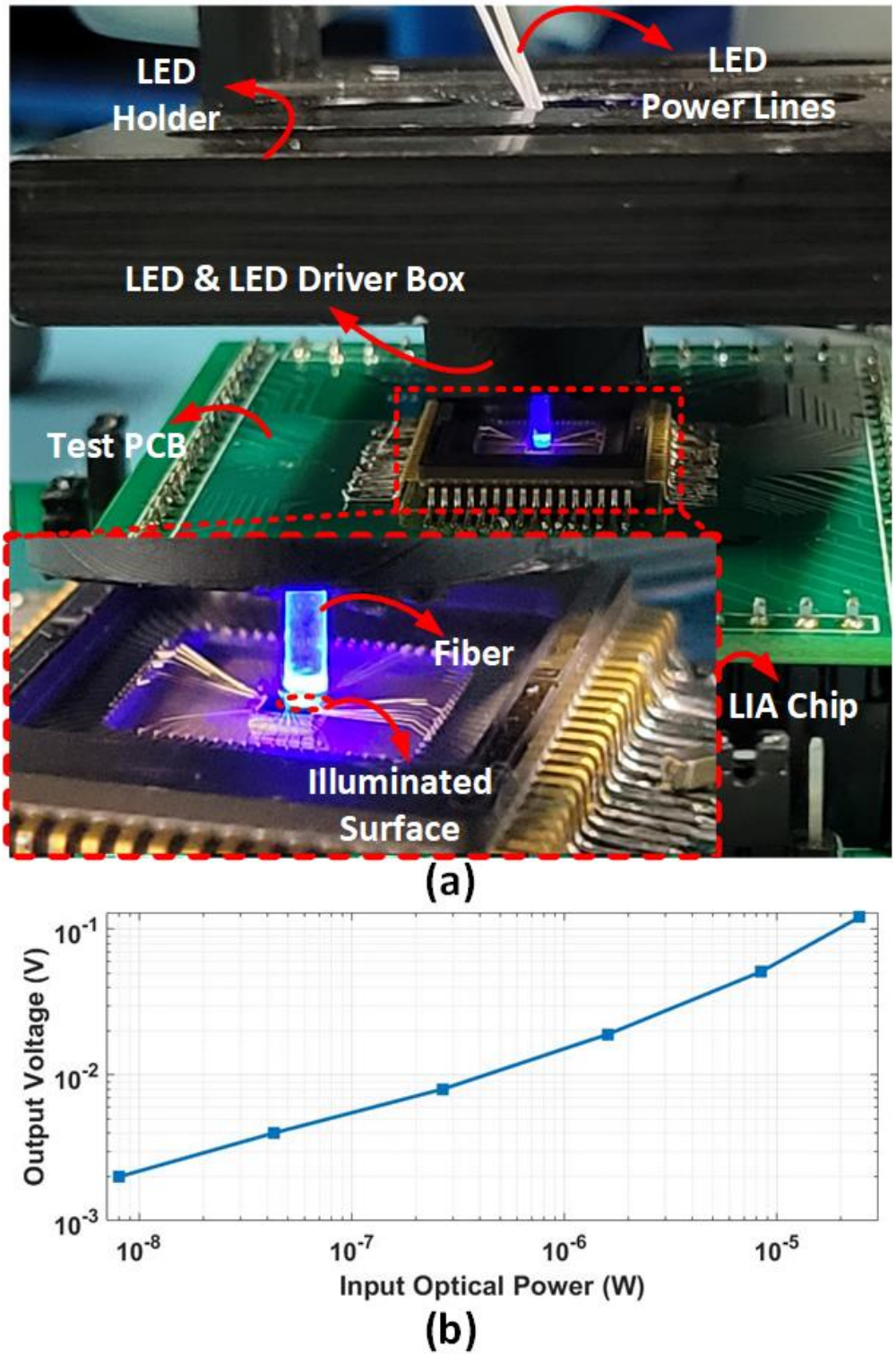

Fig. 4.25. (a) Optical measurement setup of the LIA chip and (b) Output voltage of the LIA versus the input optical power.

signal and the generated noise are fed into the input front-end amplifier with a resistive feedback gain of 20 dB. The input signal then passes through the BPF, PGA, and the mixer and finally generates a DC voltage at the LPF output. This

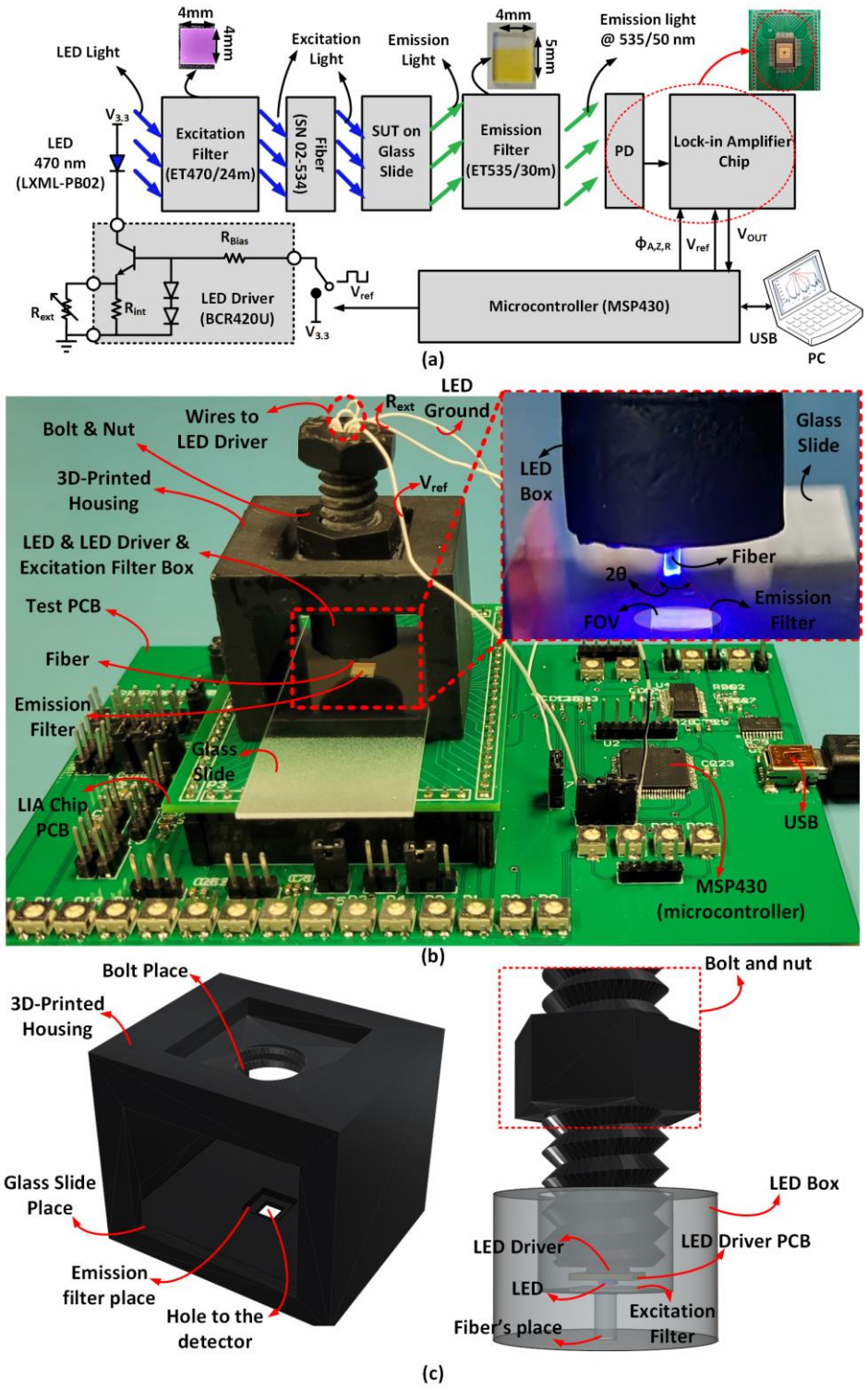

Fig. 4.26. (a) Block diagram of the experimental setup. (b) Photo of the experimental setup. (c) Details of the 3D-Printed housing and LED box.

test setup characterizes the LIA's performance when a small input signal is buried in considerable noise power. Fig. 4.23 shows the input signal of 800 nV buried in 36 µV RMS noise and the rectified voltage at the input of the output

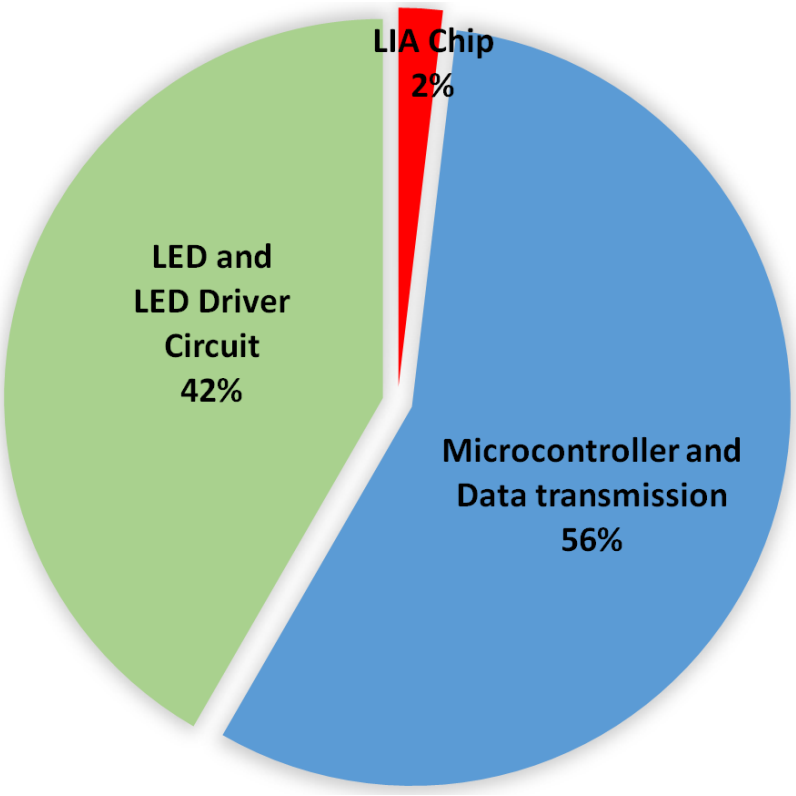

Fig. 4.27. Power consumption breakdown of the experimental setup. The total power consumption is of 36.7 mW.

LPF, which shows that V_{FB90} and V_{PGA} have a 90° phase difference. The output voltage is a DC voltage that changes from 2 mV to 120 mV, while the input signal changes from 800 nV to 100 µV, as shown in Fig. 4.23 (b). The minimum SNR of the output signal (with 0.7 mV_{rms} noise) is 9 dB, and the minimum SNR of the input is −33 dB, which results in a dynamic range of 42 dB for the LIA.

Fig. 4.24 shows different measured output DC voltages corresponding to different powers of the incoming light at the output of the LPF. It shows the ability of the lock-in amplifier to recognize and differentiate between different values of the input signal. To test the optical capability of the LIA, as shown in Fig. 4.25 (a), an LED is placed at a fixed distance from the LIA chip with an LED holder. The LED is powered with a function generator, providing a pulse wave signal with a 1 kHz frequency. Changing the amplitude of the pulse wave signal from 2 V to 2.8 V changes the optical power of the LED from 8 nW to 24 µW, and the LIA can differentiate between 8 and 44 nW, which means the LIA has roughly a resolution of 36 nW. To measure the light intensity at the fiber tip at

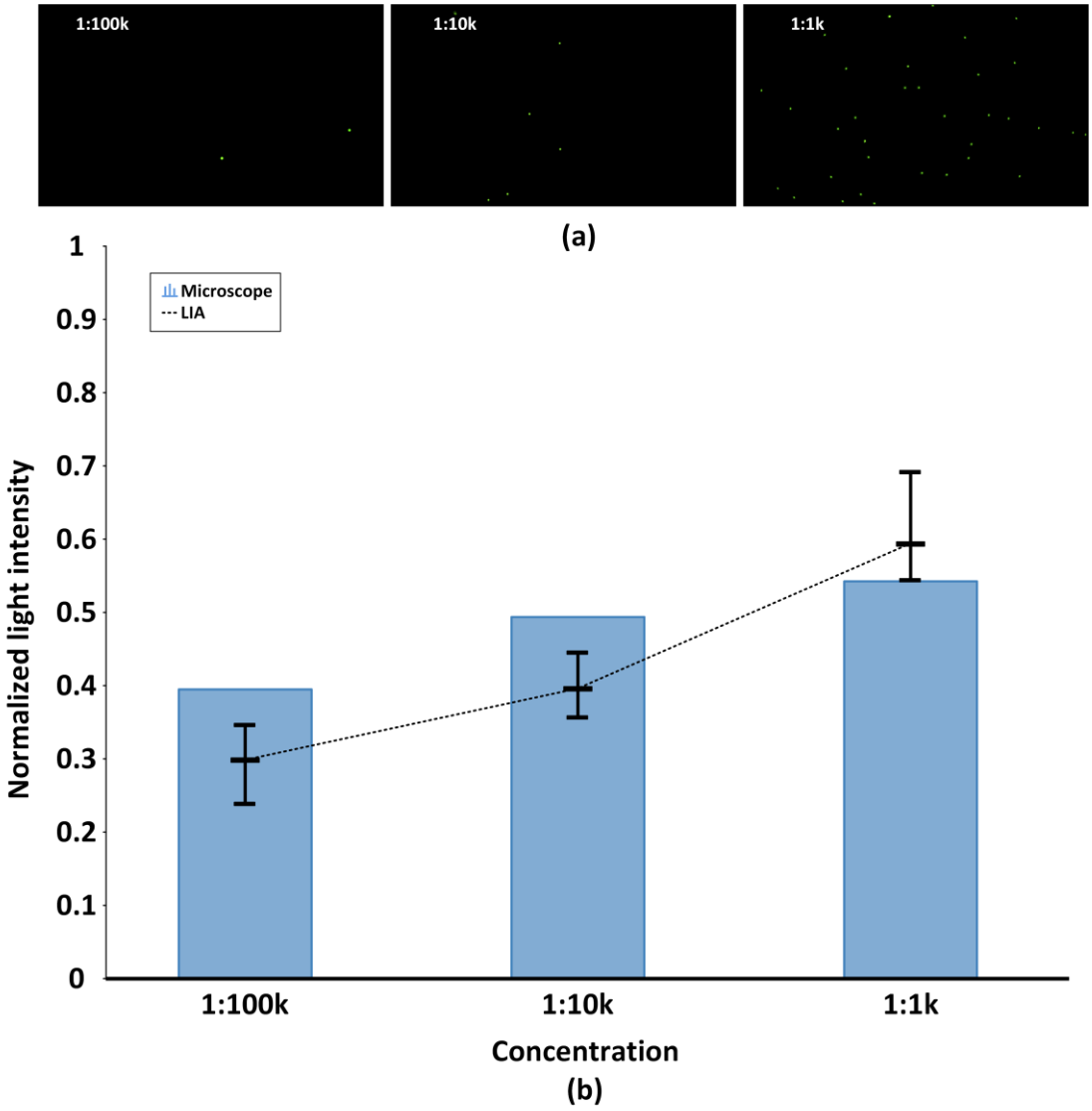

Fig. 4.28. (a)The images of measured samples (beads diluted in PBS) for three different concentrations including 1:1k, 1:10k, and 1:100k. (b)The measurement results of microscope (blue bars), and LIA chip (black lines).

different pulse wave amplitudes, the LED is placed approximately at the same distance with a slim PD power sensor (S130C) connected to an optical power meter (PM100D, Thorlabs, Newton, NJ, USA). Fig. 4.25 (b) shows the output voltage of the LIA versus the input optical power. The results of the LIA are summarized in Table 4.2 and compared with other reports. Based on these measurements, the sensitivity of the proposed LIA is calculated to be 250 mV/μW, while the LIA consumes only 0.7 mW. In addition, measurement results obtained in a dark room without any input light, show that the LIA has a

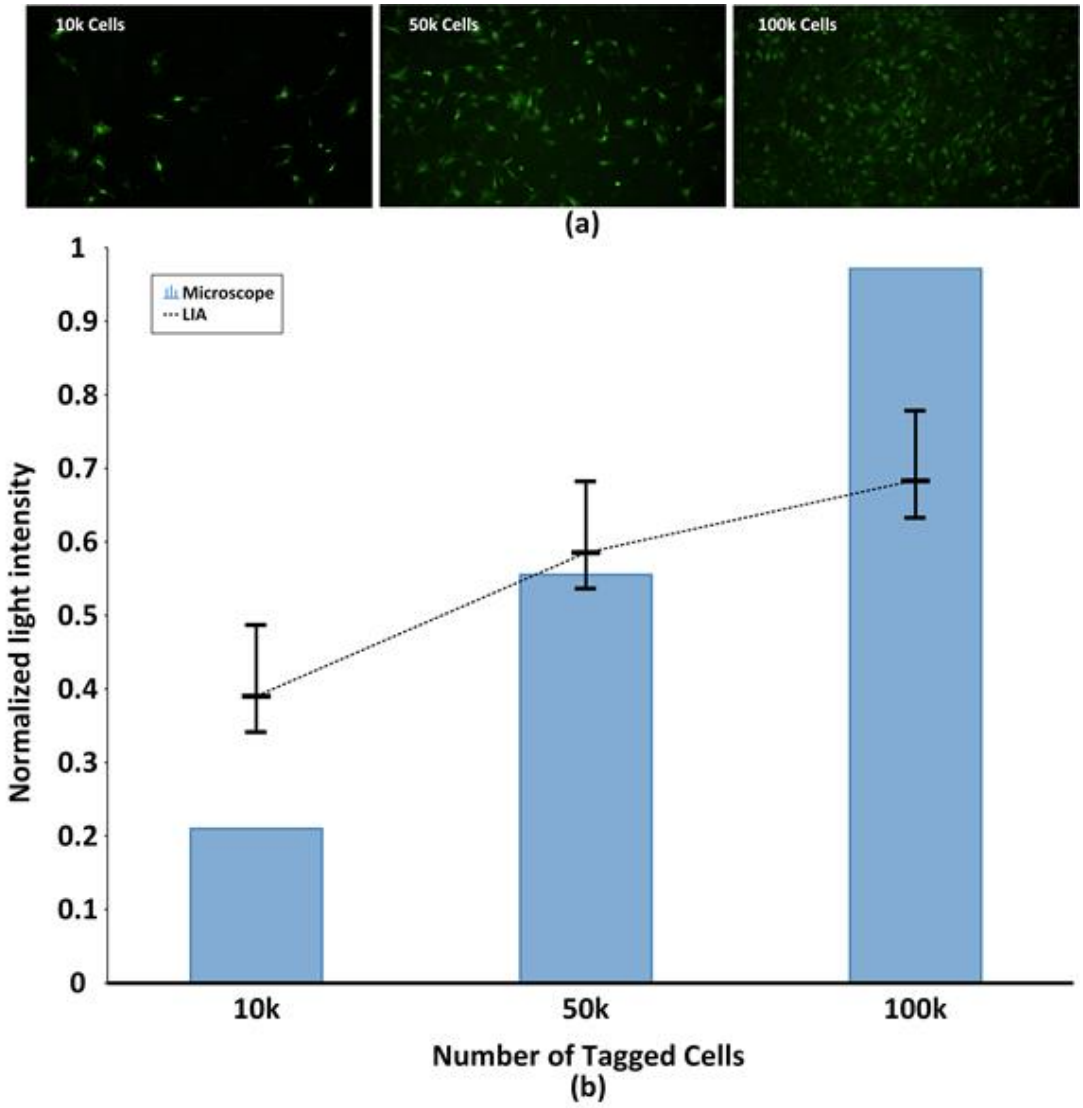

Fig. 4.29. (a) The images of three cell (NIH3T3) densities stained by Green Cytoplasmic Membrane Dye, taken with microscope. (b) The measurement results of emitted light intensities with microscope (blue bars) and LIA chip (black) for three different cell densities.

minimum detectable input current of 50.3 fA, while the TIA utilizes R_f = 1 GΩ and C_f = 1 pF.

4.7. Experimental Design and Discussion

An experimental setup is designed to investigate further the performance of the proposed LIA as a POC system. The design is first tested with fluorescent beads to confirm the functionality of the setup, and then utilized to perform in vitro measurements with labeled cells. Fig. 4.26 presents the block diagram of

the experimental setup and the setup's picture, including a 3D-printed housing, a test board, and a PC. In this setup, the LED illuminates the measured sample, and the PC displays the measured sample response proportional to its concentration. The microcontroller on the test board provides the clocks for the LED and the LIA. It also transmits the output DC voltage of the LIA chip to the computer through a USB connection. A MATLAB interface running on the computer shows the real-time output, and saves the result for further processing. The whole test prototype weighs 120 g and consumes 36.7 mW, which is consumed by the LED, the LIA chip, and the microcontroller transmitting the data. Fig. 4.27 shows a pie chart presenting the measured power consumption of each building block. In terms of price, the chips were manufactured at subsidiary cost through CMC Microsystems in Canada at approximately $1000 for 40 loose dies. The 3D-printed housing costs around $5, the off-the-shelf electronic components approximately $35, the optical filters, fiber, and LED around $30, and the PCB costs $25. Therefore, the total price for producing one prototype is of around $105. The prototype is energy-efficient, economical, and lightweight, which are key characteristics of POC systems.

In the proposed experimental setup, a 3D-printed enclosure is placed on top of the photodetector to hold a glass slide and an LED box. The glass slide holds the sample between the LED and the photodetector of the LIA. The box has a 4-mm^2 hole at the bottom side to pass the emission light toward the photodetector. An emission BPF, ranging from 510 nm to 560 nm, is placed on top of the 4-mm^2 hole to filter out the source light and allow only the emission light to pass. A small 3D-printed housing with a 5-mm radius is also designed to hold a tiny PCB (4 mm × 4 mm) including a blue LED and an LED driver (BCR420U from Diodes Incorporated, Plano, TX, USA). The LED housing also consists of an excitation BPF in front of the LED, narrowing the light source spectrum to 24 nm ranging from 458 nm to 482 nm. This LED light passes through a fiber with a numerical aperture (NA) of 0.51 to illuminate a specific area, which is also called the field of view (FOV), and can be calculated with the following formula:

$$FOV = \pi \left(\frac{NA \cdot D}{cos\,\theta} + \frac{d_1}{2} \right)^2, \quad (4.19)$$

where D is the distance between the fiber tip and the glass slide, d_1 is the diameter of the fiber's core, and θ represents half of the fiber's acceptance angle. The LED housing is attached to the end of a bolt, which is placed on the upper side of the 3D-printed enclosure and fixed with a nut. The bolt can move up and down to change D, which maximizes or minimizes the FOV. In this design, regarding the surface and NA of the fiber and a 4 mm^2 hole, the FOV can be changed from 0.75 mm^2 to 4 mm^2.

The following experiments are designed to present the LIA's ability to 1- detect the emitted light, and 2- discriminate between the emission lights of different sample concentrations. First, multiple concentrations of beads (Fluoresbrite® YG Microspheres 10.0 µm cat#18140-2 Polysciences, Inc., Warrington, PA, USA) that can absorb blue light (peak at 441 nm) and re-emit green light (peak at 485 nm) are placed on a glass slide. In this step, 1 µL of the bead solutions is dissolved in 1, 10, and 100 mL final volumes of PBS. The bead solutions are diluted to obtain 0.1%, 0.01%, and 0.001% of beads in PBS. This way, three different solutions with different bead concentrations are prepared. Then, a Nikon ECLIPSE Ti2-E motorized microscope with an CMOS Iris 15 camera and an X-Cite XYLIS Xt720L fluorescence light source, in which the objective is a CFI Plan Apochromat Lambda 10x (NA = 0.45; WD = 4.0 mm), is used to visualize the three bead solutions, as shown in Fig. 4.28 (a). The microscope also measures the mean intensity of each solution, as shown with blue bars in Fig. 4.28 (b). Afterward, the re-emitted fluorescence light intensity of each concentration is measured and recorded with the LIA chip. The real-time measurement fluctuations show an error rate of 15% for each concentration. The average value over the recorded data, as indicated in Fig. 4.28 (b), presents the LIA ability to detect and differentiate between the three bead concentrations of 1:1 k, 1:10 k, and 1:100 k. Each mean value of the LIA measurements in Fig. 4.28 (b) shows an average value of 2000 points measured during 500 ms that are normalized in amplitude between 0 and 1 to eliminate data redundancy and facilitate data analysis.

Finally, to test the LIA chip's capability to identify and quantify biomarkers attached to cells, in-vitro experiments on mouse fibroblast cells labeled with a cytoplasmic membrane dye are designed and performed. NIH3T3 embryonic mouse fibroblast cells (ATCC® CRL-1658TM) are seeded on 18 mm coverslips coated with Matrigel (C354277, Corning™) at a density of 10, 50, or 100 k per well. The cells are kept in a high-glucose DMEM (10-017-CV, Corning™) supplemented with 10% bovine calf serum (97068-085, VWR) for 12–24 h at 37 °C in a humidified atmosphere of 95% air and 5% CO2. The cells are then fixed with 4% paraformaldehyde (J19943-k2, Thermo Fisher Scientific) and washed in PBS thrice. Only 1 h before imaging, the fixed cells are incubated with 5 µL/mL of Biotracker 490 Green Cytoplasmic Membrane Dye (SCT106, EMD Millipore) for 30 min at 37 °C and then washed with PBS before being placed on a glass slide, which is then observed under the microscope. Three different samples containing 10, 50, and 100 k cells are stained and tested during these in vitro experiments. Fig. 4.29 (a) shows an image of cell density for each sample taken with the microscope. The microscope measures the mean intensity of the emitted fluorescent light of each sample, as shown with blue bars in Fig. 4.29 (b). Then, the emitted light intensity of each sample is measured with the LIA chip. The results are presented in Fig. 4.29 (b), demonstrating that the LIA chip can identify the fluorescent light intensity and follow the increasing fluorescent light that comes from different cell densities.

As shown in Fig. 4.29 (a), the cell distribution is not uniform, which can have different reasons.

First, it is hard to give an absolute value for biological experiments since cells can behave differently and have different morphology and size depending on external conditions such as stress.

Secondly, adherent cells like to grow nearby other cells. Hence, lower concentrations of cells are not uniformly distributed all over the slide and are found in clusters. Such characteristics result in non-linear behavior, as shown in Fig. 4.29 (b). To overcome this issue, the number of readings can be increased.

It should be mentioned that this was a proof of concept experiment, and these experiments were designed to verify the capability of the prototype to discriminate between different concentrations, which is well presented.

4.8. Conclusion

We presented a new fluorescence cell photometry system based on custom integrated LIA circuits. Circuits and photodetectors are integrated on a single CMOS chip designed in 180 nm CMOS technology. Circuit- and system-level modifications are applied to the LIA design to improve the performance. Such modifications result in a dynamic range of 42 dB and a sensitivity of 250 mV/μW, while the power consumption of the LIA is 0.7 mW. Lastly, a 3D-printed housing is designed to make a POC fluorescence fiber photometry system weighing 120 gr and consuming 36.7 mW power. Different experiments were performed to assess the system's detection capability, like in a POC device. In conclusion, the POC system designed around the LIA chip has a sensitivity of 1:1 k, while detecting beads in a PBS solution and can detect a minimum density of 10 k tagged cells in in vitro experiments. Moreover, the in vitro results show that the proposed device can differentiate between 10, 50, and 100 k tagged cells. Such characteristics present the designed system as a promising candidate to identify and quantify biomarkers, result in fast detection and treatment of diseases, such as COVID-19.

ACKNOWLEDGMENT

We acknowledge the support of the Canada Research Chair in Smart Biomedical Microsystems and CMC Microsystems.

Conclusion and Future Work

Conclusion

This project has designed and implemented a high-precision and low-power fluorescence cell photometry system, which is portable and cost-effective. Such a system can aid physicians in the early diagnosis, prognosis, prevention, and treatment of various diseases such as COVID-19. Increasing the approachability of such devices for all people worldwide by providing them with a cost-effective, lightweight, and battery-operated device is the other main contribution of this thesis. The introduction of the thesis demonstrated the critical role of such research studies in raising the public's life expectancy in the world.

The Introduction of this thesis briefly explains the basic principle of light-sample interactions and fluorescence-based methods. Then, chapter 1 reviews the current research studies published in major scientific journals and presents the last commercial devices available on the market. Finally, some initial results are presented to observe the preliminary performance of the fabricated CMOS photodiode and the implemented design based on cost-effective components available in the market. The second chapter then explain the methodology of this thesis.

The third chapter presents a miniature cell fiber-spectrophotometer to sense the fluorescence emission for the real-time detection of biomarkers. The effectiveness of the proposed method is demonstrated by its measured electrical performance and the *in vitro* experimental validation. We have measured the noise, the responsivity, the minimum detected light power, and the power consumption of the prototype. We have provided a comparison of the measured performance with other solutions. This chapter also describes the *in vitro* validation and summarizes the obtained results. Two fluorophores, namely DAPI and Alexa Fluor 488, are measured with the presented prototype to assess and measure the selectivity and sensitivity of the prototype. The prototype was used to measure different concentrations of Alexa Fluor 488. All measurements were performed several times over three days to demonstrate

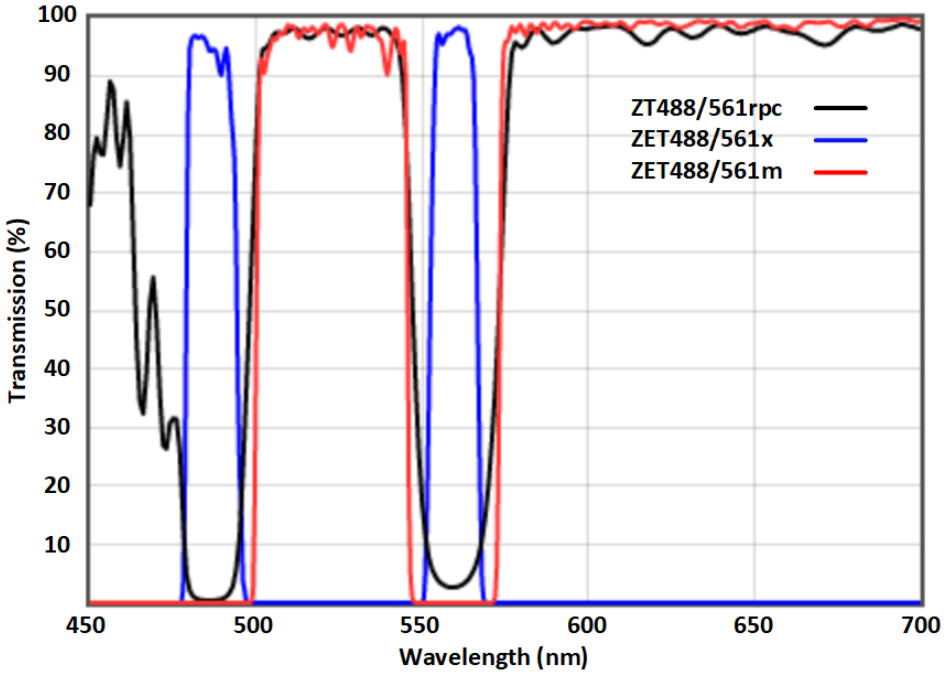

Fig. 5.1. Transmission spectrum of a dual band set of optical lenses for use with lasers between 486-492nm and 556-563nm, adapted from chroma.com.

the reliability and reproducibility of the results. Rigorous analysis and scientific discussion are provided to conclude this chapter.

The fourth chapter describes the implementation of a die that includes both photodiodes and lock-in amplifier circuits. Such integration can drastically decrease the size of the final product to be an ideal candidate for a POC system. The circuit solutions decrease the noise and the power consumption, which are the main challenges to improving the performance of such a high-precision device. The proposed system is compared with other reports to show the effectiveness of the proposed solutions. Finally, the system is tested with LEDs, beads, and tagged cells to show the electrical and optical characteristics of the proposed design.

The last chapter concludes the thesis and provides the future work.

Future Work

For future work, any scheme that decreases the size and power consumption, including the circuit ideas, could be helpful. In addition, integrating all-optical components on a silicon photonic chip and then packaging both optical and electrical chips on an interposer could drastically improve the size of the final

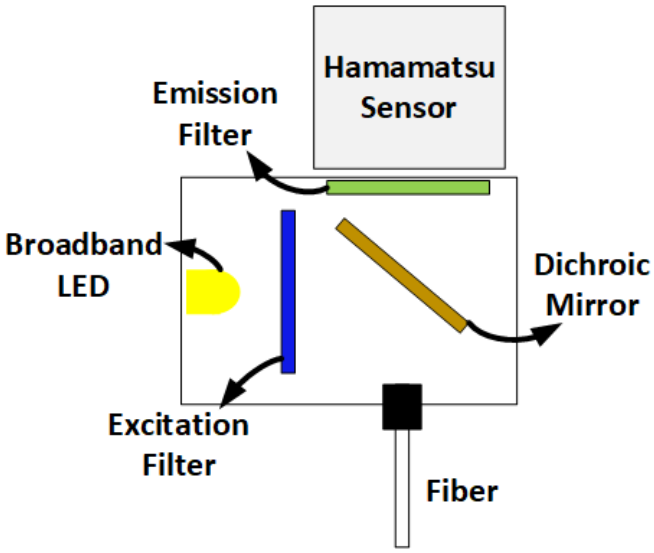

Fig. 5.2. Suggested multi-color fluorescence spectrophotometry design.

design. In terms of application, utilizing different lenses simultaneously for two fluorophores can contribute to the performance of the final design. Fig. 5.1 shows the spectral transmission response of the proposed emission filter, excitation filter, and dichroic mirror. The light source in this design includes a broadband spectrum such as white light, which could be an LED to save power. The excitation filter (ZET488/561x) only lets the wavelengths around 488 nm and 561 nm center frequencies pass. The emission filter (ZT488/561) is valid for reflection light resulting from lasers between 486-492 nm and 556-563 nm. Finally, the dichroic mirror (ZET488/561m) only lets the emission light pass and reflects the source light into the fiber. The suggested miniaturized setup is presented in Fig. 5.2. As mentioned earlier, such a device can extract the fluorescence response of two tags simultaneously, expanding the application area while almost consuming the same power consumption and weight.

Publication Lists

Journals papers:

- **V. K. Lazarjan**, A. B. Gashti, M. Feshki, A. Garnier, and B. Gosselin, "Miniature Fiber-Spectrophotometer for Real-Time Biomarkers Detection," in IEEE Sensors Journal, vol. 21, no. 13, pp. 14822-14837, 1 July1, 2021.
- **V. K. Lazarjan**, M. Crochetière, M. N. Khiarak, S. GH. Aarani, S. N. Hosseini, P. Marquet, B. Gosselin. " High-Precision Ping-pong Auto-zeroed Lock-in Fluorescence Photometry Sensor." Submitted to IEEE Journal of Solid-State Circuits (JSSC 2022).

Conferences papers:

- **V. K. Lazarjan**, M. N. Khiarak, A. B. Gashti, A. Garnier, and Benoit Gosselin. "Miniaturized Wireless Cell Spectrophotometer Platform in Visible and Near-IR Range." In 2018 IEEE Life Sciences Conference (LSC), pp. 29-32. IEEE, 2018.
- **V. K. Lazarjan**, S. N. Hosseini, M. N. Khiarak, and B. Gosselin. "CMOS Optoelectronic Sensor with Ping-pong Auto-zeroed Transimpedance Amplifier." In 2020 IEEE 63rd International Midwest Symposium on Circuits and Systems (MWSCAS), pp. 17-20. IEEE, 2020.
- S. N. Hosseini, **V. K. Lazarjan**, M. M. Akram and B. Gosselin, "CMOS Multi-Frequency Lock-in Sensor for Impedance Spectroscopy in Microbiology Applications," 2022 20th IEEE Interregional NEWCAS Conference (NEWCAS), 2022, pp. 129-133.

References

[1] J. P. Broughton *et al.*, “CRISPR–Cas12-based detection of SARS-CoV-2,” *Nature Biotechnology*, vol. 38, no. 7, Art. no. 7, Jul. 2020, doi: 10.1038/s41587-020-0513-4.

[2] N. Rabiee *et al.*, “Point-of-Use Rapid Detection of SARS-CoV-2: Nanotechnology-Enabled Solutions for the COVID-19 Pandemic,” *International Journal of Molecular Sciences*, vol. 21, no. 14, Art. no. 14, Jan. 2020, doi: 10.3390/ijms21145126.

[3] V. K. Lazarjan, A. B. Gashti, M. Feshki, A. Garnier, and B. Gosselin, “Miniature Fiber-Spectrophotometer for Real-Time Biomarkers Detection,” *IEEE Sensors Journal*, pp. 1–1, 2021, doi: 10.1109/JSEN.2021.3072578.

[4] E. Morales-Narváez and C. Dincer, “The impact of biosensing in a pandemic outbreak: COVID-19,” *Biosensors and Bioelectronics*, vol. 163, p. 112274, Sep. 2020, doi: 10.1016/j.bios.2020.112274.

[5] G. Kallergi, M. A. Papadaki, E. Politaki, D. Mavroudis, V. Georgoulias, and S. Agelaki, “Epithelial to mesenchymal transition markers expressed in circulating tumour cells of early and metastatic breast cancer patients,” *Breast Cancer Res*, vol. 13, no. 3, p. R59, Jun. 2011, doi: 10.1186/bcr2896.

[6] C. Li, C. J. Lee, and D. M. Simeone, “Identification of Human Pancreatic Cancer Stem Cells,” in *Cancer Stem Cells: Methods and Protocols*, J. S. Yu, Ed. Totowa, NJ: Humana Press, 2009, pp. 161–173. doi: 10.1007/978-1-59745-280-9_10.

[7] Y. Meng, S. Kang, J. So, S. Reierstad, and D. A. Fishman, “Translocation of Fas by LPA prevents ovarian cancer cells from anti-Fas-induced apoptosis,” *Gynecologic Oncology*, vol. 96, no. 2, pp. 462–469, Feb. 2005, doi: 10.1016/j.ygyno.2004.10.024.

[8] S. M. Dhanasekaran *et al.*, “Delineation of prognostic biomarkers in prostate cancer,” *Nature*, vol. 412, no. 6849, pp. 822–826, Aug. 2001, doi: 10.1038/35090585.

[9] G. Keiser, *Biophotonics: Concepts to Applications*. Springer Singapore, 2016. Accessed: Sep. 27, 2019. [Online]. Available: https://www.springer.com/gp/book/9789811009433

[10] L. A. Gunaydin *et al.*, “Natural Neural Projection Dynamics Underlying Social Behavior,” *Cell*, vol. 157, no. 7, pp. 1535–1551, Jun. 2014, doi: 10.1016/j.cell.2014.05.017.

[11] C. Meng, J. Zhou, A. Papaneri, T. Peddada, K. Xu, and G. Cui, “Spectrally Resolved Fiber Photometry for Multi-component Analysis of Brain Circuits,” *Neuron*, vol. 98, no. 4, pp. 707-717.e4, May 2018, doi: 10.1016/j.neuron.2018.04.012.

[12] J. Peloquin, Y. Komarova, and G. Borisy, “Conjugation of fluorophores to tubulin,” *Nat Methods*, vol. 2, no. 4, pp. 299–303, Apr. 2005, doi: 10.1038/nmeth0405-299.

[13] S. Ding, X. Qiao, J. Suryadi, G. S. Marrs, G. L. Kucera, and U. Bierbach, “Using Fluorescent Post-Labeling To Probe the Subcellular Localization of DNA-Targeted Platinum Anticancer Agents,” *Angewandte Chemie International Edition*, vol. 52, no. 12, pp. 3350–3354, 2013, doi: 10.1002/anie.201210079.

[14] M. J. Selleck, M. Senthil, and N. R. Wall, “Making Meaningful Clinical Use of Biomarkers,” *Biomark Insights*, vol. 12, p. 1177271917715236, Jan. 2017, doi: 10.1177/1177271917715236.

[15] K. Ruksha *et al.*, “Over-Expression of βII-Tubulin and Especially Its Localization in Cell Nuclei Correlates with Poorer Outcomes in Colorectal Cancer,” *Cells*, vol. 8, no. 1, p. 25, Jan. 2019, doi: 10.3390/cells8010025.

[16] C. F. Fronczek, T. S. Park, D. K. Harshman, A. M. Nicolini, and J.-Y. Yoon, “Paper microfluidic extraction and direct smartphone-based identification of pathogenic nucleic acids from field and clinical samples,” *RSC Adv.*, vol. 4, no. 22, pp. 11103–11110, Feb. 2014, doi: 10.1039/C3RA47688J.

[17] A. Manickam *et al.*, “A Fully Integrated CMOS Fluorescence Biochip for DNA and RNA Testing,” *IEEE Journal of Solid-State Circuits*, vol. 52, no. 11, pp. 2857–2870, Nov. 2017, doi: 10.1109/JSSC.2017.2754363.

[18] T. Songjaroen, T. Maturos, A. Sappat, A. Tuantranont, and W. Laiwattanapaisal, “Portable microfluidic system for determination of urinary creatinine,” *Analytica Chimica Acta*, vol. 647, no. 1, pp. 78–83, Aug. 2009, doi: 10.1016/j.aca.2009.05.014.

[19] L. Hong, H. Li, H. Yang, and K. Sengupta, “Fully Integrated Fluorescence Biosensors On-Chip Employing Multi-Functional Nanoplasmonic Optical Structures in CMOS,” *IEEE Journal of Solid-State Circuits*, vol. 52, no. 9, pp. 2388–2406, Sep. 2017, doi: 10.1109/JSSC.2017.2712612.

[20] V. K. Lazarjan, M. N. Khiarak, A. B. Gashti, A. Garnier, and B. Gosselin, “Miniaturized Wireless Cell Spectrophotometer Platform in Visible and Near-IR Range,” in *2018 IEEE Life Sciences Conference (LSC)*, Oct. 2018, pp. 29–32. doi: 10.1109/LSC.2018.8572252.

[21] M. N. Khiarak et al., “A Wireless Fiber Photometry System Based on a High-Precision CMOS Biosensor With Embedded Continuous-Time Sigma Delta Modulation,” IEEE Trans. Biomed. Circuits Syst., vol. 12, no. 3, pp. 495–509, Jun. 2018, doi: 10.1109/TBCAS.2018.2817200.

[22] J. Senarathna *et al.*, “A miniature multi-contrast microscope for functional imaging in freely behaving animals,” *Nat Commun*, vol. 10, no. 1, p. 99, Dec. 2019, doi: 10.1038/s41467-018-07926-z.

[23] A. A. Kisomi, H. Landari, M. Boukadoum, A. Miled, and B. Gosselin, “Towards a multi-wavelength spectroscopy platform for blood characterization and analysis,” in *2016 38th Annual International Conference of the IEEE Engineering in Medicine and Biology Society (EMBC)*, Aug. 2016, pp. 2994–2997. doi: 10.1109/EMBC.2016.7591359.

[24] D. Aharoni and T. M. Hoogland, “Circuit Investigations With Open-Source Miniaturized Microscopes: Past, Present and Future,” *Front. Cell. Neurosci.*, vol. 13, 2019, doi: 10.3389/fncel.2019.00141.

[25] K. K. Ghosh *et al.*, “Miniaturized integration of a fluorescence microscope,” *Nat Methods*, vol. 8, no. 10, pp. 871–878, Oct. 2011, doi: 10.1038/nmeth.1694.

[26] V. K. Lazarjan, S. Nazila Hosseini, M. N. Khiarak, and B. Gosselin, “CMOS Optoelectronic Sensor with Ping-pong Auto-zeroed Transimpedance Amplifier,” in *2020 IEEE 63rd International Midwest Symposium on Circuits and Systems (MWSCAS)*, Aug. 2020, pp. 17–20. doi: 10.1109/MWSCAS48704.2020.9184520.

[27] Y. Chen *et al.*, “Design of a high-resolution light field miniscope for volumetric imaging in scattering tissue,” *Biomed. Opt. Express, BOE*, vol. 11, no. 3, pp. 1662–1678, Mar. 2020, doi: 10.1364/BOE.384673.

[28] C. C. Jung, E. W. Saaski, D. A. McCrae, B. M. Lingerfelt, and G. P. Anderson, “RAPTOR: A fluoroimmunoassay-based fiber optic sensor for detection of biological threats,” *IEEE Sensors J.*, vol. 3, no. 4, pp. 352–360, Aug. 2003, doi: 10.1109/JSEN.2003.815775.

[29] H. Wang, Y. Qi, T. J. Mountziaris, and C. D. Salthouse, “A portable time-domain LED fluorimeter for nanosecond fluorescence lifetime measurements,” *Review of Scientific Instruments*, vol. 85, no. 5, p. 055003, May 2014, doi: 10.1063/1.4873330.

[30] J. Kissinger and D. Wilson, “Portable Fluorescence Lifetime Detection for Chlorophyll Analysis in Marine Environments,” *IEEE Sensors Journal*, vol. 11, no. 2, pp. 288–295, Feb. 2011, doi: 10.1109/JSEN.2010.2054078.

[31] M. N. Khiarak, S. Martel, Y. D. Koninck, and B. Gosselin, “Wireless Optoelectronic Fiber Photometry Headstage for Deep Brain Structures Monitoring,” in *2018 IEEE Life Sciences Conference (LSC)*, Oct. 2018, pp. 9–12. doi: 10.1109/LSC.2018.8572276.

[32] L. Lu *et al.*, “Wireless optoelectronic photometers for monitoring neuronal dynamics in the deep brain,” *PNAS*, vol. 115, no. 7, pp. E1374–E1383, Feb. 2018, doi: 10.1073/pnas.1718721115.

[33] Y. Sunaga, Y. Ohta, Y. M. Akay, J. Ohta, and M. Akay, “Monitoring Neural Activities in the VTA in Response to Nicotine Intake Using a Novel Implantable Microimaging Device,” *IEEE Access*, vol. 8, pp. 68013–68020, 2020, doi: 10.1109/ACCESS.2020.2985705.

[34] E. Rustami *et al.*, “Needle-Type Imager Sensor With Band-Pass Composite Emission Filter and Parallel Fiber-Coupled Laser Excitation,” *IEEE Transactions on Circuits and Systems I: Regular Papers*, vol. 67, no. 4, pp. 1082–1091, Apr. 2020, doi: 10.1109/TCSI.2019.2959592.

[35] M. L. Rynes *et al.*, “Miniaturized head-mounted microscope for whole-cortex mesoscale imaging in freely behaving mice,” *Nature Methods*, vol. 18, no. 4, Art. no. 4, Apr. 2021, doi: 10.1038/s41592-021-01104-8.

[36] L. Hong, H. Li, H. Yang, and K. Sengupta, “Nano-plasmonics and electronics co-integration in CMOS enabling a pill-sized multiplexed fluorescence microarray system,” *Biomed. Opt. Express*, vol. 9, no. 11, p. 5735, Nov. 2018, doi: 10.1364/BOE.9.005735.

[37] M. Kim *et al.*, “Miniaturized and Wireless Optical Neurotransmitter Sensor for Real-Time Monitoring of Dopamine in the Brain,” *Sensors*, vol. 16, no. 11, p. 1894, Nov. 2016, doi: 10.3390/s16111894.

[38] M. Noormohammadi Khiarak, S. Martel, Y. De Koninck, and B. Gosselin, “High-DR CMOS Fluorescence Biosensor With Extended Counting ADC and Noise Cancellation,” *IEEE Trans. Circuits Syst. I*, vol. 66, no. 6, pp. 2077–2087, Jun. 2019, doi: 10.1109/TCSI.2019.2895652.

[39] K. Morimoto *et al.*, “Megapixel time-gated SPAD image sensor for 2D and 3D imaging applications,” *Optica, OPTICA*, vol. 7, no. 4, pp. 346–354, Apr. 2020, doi: 10.1364/OPTICA.386574.

[40] B. Zambrano, S. Strangio, T. Rizzo, E. Garzón, M. Lanuzza, and G. Iannaccone, “All-Analog Silicon Integration of Image Sensor and Neural Computing Engine for Image Classification,” *IEEE Access*, vol. 10, pp. 94417–94430, 2022, doi: 10.1109/ACCESS.2022.3203394.

[41] W. Gao, Z. Xu, X. Han, and C. Pan, “Recent advances in curved image sensor arrays for bioinspired vision system,” *Nano Today*, vol. 42, p. 101366, Feb. 2022, doi: 10.1016/j.nantod.2021.101366.

[42] “FAB Technologies – CMC Microsystems.” https://www.cmc.ca/technologies/ (accessed Oct. 20, 2022).

[43] C. H. Woo, S. Jang, G. Shin, G. Y. Jung, and J. W. Lee, “Sensitive fluorescence detection of SARS-CoV-2 RNA in clinical samples via one-pot isothermal ligation and transcription,” *Nature Biomedical Engineering*, pp. 1–12, Sep. 2020, doi: 10.1038/s41551-020-00617-5.

[44] N. Goossens, S. Nakagawa, X. Sun, and Y. Hoshida, “Cancer biomarker discovery and validation,” *Transl Cancer Res*, vol. 4, no. 3, pp. 256–269, Jun. 2015, doi: 10.3978/j.issn.2218-676X.2015.06.04.

[45] J. Joung *et al.*, “Point-of-care testing for COVID-19 using SHERLOCK diagnostics,” *medRxiv*, May 2020, doi: 10.1101/2020.05.04.20091231.

[46] “Cancer.” https://www.who.int/news-room/fact-sheets/detail/cancer (accessed Aug. 22, 2020).

[47] P. T. Nghiem *et al.*, “PD-1 Blockade with Pembrolizumab in Advanced Merkel-Cell Carcinoma,” *N Engl J Med*, vol. 374, no. 26, pp. 2542–2552, Jun. 2016, doi: 10.1056/NEJMoa1603702.

[48] M. Jermyn *et al.*, “Intraoperative brain cancer detection with Raman spectroscopy in humans,” *Sci. Transl. Med.*, vol. 7, no. 274, pp. 274ra19-274ra19, Feb. 2015, doi: 10.1126/scitranslmed.aaa2384.

[49] E. Beaulieu *et al.*, “Wide-field optical spectroscopy system integrating reflectance and spatial frequency domain imaging to measure attenuation-corrected intrinsic tissue fluorescence in radical prostatectomy specimens,” *Biomed. Opt. Express, BOE*, vol. 11, no. 4, pp. 2052–2072, Apr. 2020, doi: 10.1364/BOE.388482.
[50] T. J. Chozinski *et al.*, “Expansion microscopy with conventional antibodies and fluorescent proteins,” *Nat Methods*, vol. 13, no. 6, pp. 485–488, Jun. 2016, doi: 10.1038/nmeth.3833.
[51] R. Dhingra and R. S. Vasan, “Biomarkers in cardiovascular disease: Statistical assessment and section on key novel heart failure biomarkers,” *Trends in Cardiovascular Medicine*, vol. 27, no. 2, pp. 123–133, Feb. 2017, doi: 10.1016/j.tcm.2016.07.005.
[52] U. Obahiagbon *et al.*, “A compact, low-cost, quantitative and multiplexed fluorescence detection platform for point-of-care applications,” *Biosensors and Bioelectronics*, vol. 117, pp. 153–160, Oct. 2018, doi: 10.1016/j.bios.2018.04.002.
[53] R. D. Black, N. G. Bolick, R. A. Richardson, and M. W. Dewhirst, “In Vivo Monitoring of a Fluorescently Labeled Antibody in Mice With Breast Cancer Xenografts,” *IEEE Sensors Journal*, vol. 8, no. 1, pp. 81–88, Jan. 2008, doi: 10.1109/JSEN.2007.912911.
[54] M. Biehl and T. Velten, “Gaps and Challenges of Point-of-Care Technology,” *IEEE Sensors Journal*, vol. 8, no. 5, pp. 593–600, May 2008, doi: 10.1109/JSEN.2008.918919.
[55] Y. Hagihara *et al.*, “Photoactivatable oncolytic adenovirus for optogenetic cancer therapy,” *Cell Death & Disease*, vol. 11, no. 7, Art. no. 7, Jul. 2020, doi: 10.1038/s41419-020-02782-6.
[56] S. Kumar *et al.*, “MoS2 Functionalized Multicore Fiber Probes for Selective Detection of Shigella Bacteria based on Localized Plasmon,” *Journal of Lightwave Technology*, pp. 1–1, 2020, doi: 10.1109/JLT.2020.3036610.
[57] C. Leitão *et al.*, “Cortisol AuPd plasmonic unclad POF biosensor,” *Biotechnology Reports*, vol. 29, p. e00587, Mar. 2021, doi: 10.1016/j.btre.2021.e00587.
[58] A. G. Leal-Junior, A. Frizera, C. Marques, and M. J. Pontes, “Optical Fiber Specklegram Sensors for Mechanical Measurements: A Review,” *IEEE Sensors Journal*, vol. 20, no. 2, pp. 569–576, Jan. 2020, doi: 10.1109/JSEN.2019.2944906.
[59] R. Feng *et al.*, “Mutations in TUBB8 and Human Oocyte Meiotic Arrest,” *New England Journal of Medicine*, vol. 374, no. 3, pp. 223–232, Jan. 2016, doi: 10.1056/NEJMoa1510791.
[60] J. R. Lakowicz, *Principles of Fluorescence Spectroscopy*, 3rd edition. Springer Science & Business Media, 2013.
[61] J. G. Webster and A. J. Nimunkar, *Medical Instrumentation: Application and Design*, 5th ed. John Wiley & Sons, 2020.
[62] L. B. Mcgown and K. Nithipatikom, “Molecular Fluorescence and Phosphorescence,” *Applied Spectroscopy Reviews*, vol. 35, no. 4, pp. 353–393, Nov. 2000, doi: 10.1081/ASR-100101229.
[63] J. W. Lichtman and J.-A. Conchello, “Fluorescence microscopy,” *Nature Methods*, vol. 2, no. 12, Art. no. 12, Dec. 2005, doi: 10.1038/nmeth817.
[64] R. Camacho Dejay, “Polarization portraits of lightharvesting antennas: from single molecule spectroscopy to imaging,” Ph.D. thesis, Lund University, Lund, Sweden, 2014. Accessed: Jan. 08, 2021. [Online]. Available: http://lup.lub.lu.se/record/4434719
[65] M. Feshki, M. S. Monfared, and B. Gosselin, “Development of a Dual-Wavelength Isosbestic Wireless Fiber Photometry Platform for Live Animals Studies,” in *2020 42nd Annual International Conference of the IEEE Engineering in Medicine Biology Society (EMBC)*, Jul. 2020, pp. 1836–1839. doi: 10.1109/EMBC44109.2020.9176191.

[66] C. Moreno-Hernández, D. Monzón-Hernández, I. Hernández-Romano, and J. Villatoro, “Single tapered fiber tip for simultaneous measurements of thickness, refractive index and distance to a sample,” *Opt. Express, OE*, vol. 23, no. 17, pp. 22141–22148, Aug. 2015, doi: 10.1364/OE.23.022141.
[67] R. Min *et al.*, “Inscription of Bragg gratings in undoped PMMA mPOF with Nd:YAG laser at 266 nm wavelength,” *Opt. Express, OE*, vol. 27, no. 26, pp. 38039–38048, Dec. 2019, doi: 10.1364/OE.27.038039.
[68] R. Min, C. Marques, O. Bang, and B. Ortega, “Moiré phase-shifted fiber Bragg gratings in polymer optical fibers,” *Optical Fiber Technology*, vol. 41, pp. 78–81, Mar. 2018, doi: 10.1016/j.yofte.2018.01.003.
[69] K. Angelino, P. Shah, D. A. Edlund, M. Mohit, and G. Yauney, “Clinical validation and assessment of a modular fluorescent imaging system and algorithm for rapid detection and quantification of dental plaque,” *BMC Oral Health*, vol. 17, no. 1, p. 162, Dec. 2017, doi: 10.1186/s12903-017-0472-4.
[70] T. Yang, H. Yang, C. Chang, G. R. D. Prabhu, and P. L. Urban, “Microanalysis Using Acoustically Actuated Droplets Pinned Onto a Thread,” *IEEE Access*, vol. 7, pp. 154743–154749, 2019, doi: 10.1109/ACCESS.2019.2948642.
[71] A. J. Das, A. Wahi, I. Kothari, and R. Raskar, “Ultra-portable, wireless smartphone spectrometer for rapid, non-destructive testing of fruit ripeness,” *Scientific Reports*, vol. 6, no. 1, Art. no. 1, Sep. 2016, doi: 10.1038/srep32504.
[72] A. F. D. Cruz, N. Norena, A. Kaushik, and S. Bhansali, “A low-cost miniaturized potentiostat for point-of-care diagnosis,” *Biosensors and Bioelectronics*, vol. 62, pp. 249–254, Dec. 2014, doi: 10.1016/j.bios.2014.06.053.
[73] V. Mackowiak, J. Peupelmann, and Y. Ma, “NEP – Noise Equivalent Power,” p. 5.
[74] T. Yokino *et al.*, “Grating-based ultra-compact SWNIR spectral sensor head developed through MOEMS technology,” in *MOEMS and Miniaturized Systems XVIII*, Mar. 2019, vol. 10931, p. 1093108. doi: 10.1117/12.2510472.
[75] A. Schwartz *et al.*, “Quantitating Fluorescence Intensity from Fluorophore: The Definition of MESF Assignment,” *J Res Natl Inst Stand Technol*, vol. 107, no. 1, pp. 83–91, 2002, doi: 10.6028/jres.107.009.
[76] A. Gollmer, A. Felgentraeger, T. Maisch, and C. Flors, “Real-time imaging of photodynamic action in bacteria,” *Journal of Biophotonics*, vol. 10, no. 2, pp. 264–270, 2017, doi: https://doi.org/10.1002/jbio.201500259.
[77] M. N. Khiarak, S. Martel, and B. Gosselin, “CMOS Optoelectronic Lock-in Amplifier with Semi-Digital Automatic Phase Alignment,” in *2019 IEEE International Symposium on Circuits and Systems (ISCAS)*, May 2019, pp. 1–5. doi: 10.1109/ISCAS.2019.8702587.
[78] A. Hu and V. P. Chodavarapu, “CMOS Optoelectronic Lock-In Amplifier With Integrated Phototransistor Array,” *IEEE Trans. Biomed. Circuits Syst.*, vol. 4, no. 5, pp. 274–280, Oct. 2010, doi: 10.1109/TBCAS.2010.2051438.
[79] P. M. Maya-Hernández, M. T. Sanz-Pascual, and B. Calvo, “CMOS Low-Power Lock-In Amplifiers With Signal Rectification in Current Domain,” *IEEE Transactions on Instrumentation and Measurement*, vol. 64, no. 7, pp. 1858–1867, Jul. 2015, doi: 10.1109/TIM.2014.2366978.
[80] A. De Marcellis, G. Ferri, and A. D’Amico, “One-Decade Frequency Range, In-Phase Auto-Aligned 1.8 V 2 mW Fully Analog CMOS Integrated Lock-In Amplifier for Small/Noisy Signal Detection,” *IEEE Sensors Journal*, vol. 16, no. 14, pp. 5690–5701, Jul. 2016, doi: 10.1109/JSEN.2016.2572732.
[81] P. Ciccarella, M. Carminati, M. Sampietro, and G. Ferrari, “Multichannel 65 zF rms Resolution CMOS Monolithic Capacitive Sensor for Counting Single Micrometer-Sized

Airborne Particles on Chip," *IEEE Journal of Solid-State Circuits*, vol. 51, no. 11, pp. 2545–2553, Nov. 2016, doi: 10.1109/JSSC.2016.2607338.
[82] A. De Marcellis, E. Palange, N. Liberatore, and S. Mengali, "Low-Cost Portable 1 MHz Lock-In Amplifier for Fast Measurements of Pulsed Signals in Sensing Applications," *IEEE Sensors Letters*, vol. 1, no. 4, pp. 1–4, Aug. 2017, doi: 10.1109/LSENS.2017.2713449.
[83] P. M. Maya-Hernández, B. Calvo-López, and M. T. Sanz-Pascual, "Ultralow-Power Synchronous Demodulation for Low-Level Sensor Signal Detection," *IEEE Transactions on Instrumentation and Measurement*, vol. 68, no. 10, pp. 3514–3523, Oct. 2019, doi: 10.1109/TIM.2018.2881821.
[84] G. Sciortino *et al.*, "Four-Channel Differential Lock-in Amplifiers With Autobalancing Network for Stimulated Raman Spectroscopy," *IEEE Journal of Solid-State Circuits*, vol. 56, no. 6, pp. 1859–1870, Jun. 2021, doi: 10.1109/JSSC.2020.3046484.
[85] A. De Marcellis, G. Ferri, A. D'Amico, C. Di Natale, and E. Martinelli, "A Fully-Analog Lock-In Amplifier With Automatic Phase Alignment for Accurate Measurements of ppb Gas Concentrations," *IEEE Sensors Journal*, vol. 12, no. 5, pp. 1377–1383, May 2012, doi: 10.1109/JSEN.2011.2172602.
[86] R. Agarwala, P. Wang, H. L. Bishop, A. Dissanayake, and B. H. Calhoun, "A 0.6V 785-nW Multimodal Sensor Interface IC for Ozone Pollutant Sensing and Correlated Cardiovascular Disease Monitoring," *IEEE Journal of Solid-State Circuits*, vol. 56, no. 4, pp. 1058–1070, Apr. 2021, doi: 10.1109/JSSC.2021.3057229.
[87] T. Rooijers, S. Karmakar, Y. Kusuda, J. H. Huijsing, and K. A. A. Makinwa, "A Fill-In Technique for Robust IMD Suppression in Chopper Amplifiers," *IEEE Journal of Solid-State Circuits*, vol. 56, no. 12, pp. 3583–3592, Dec. 2021, doi: 10.1109/JSSC.2021.3107350.
[88] C. Rhee, J. Park, and S. Kim, "A 0.3 lx–1.4 Mlx Monolithic Silicon Nanowire Light-to-Digital Converter With Temperature-Independent Offset Cancellation," *IEEE Journal of Solid-State Circuits*, vol. 55, no. 2, pp. 378–391, Feb. 2020, doi: 10.1109/JSSC.2019.2949257.
[89] Q. Fan, F. Sebastiano, J. H. Huijsing, and K. A. A. Makinwa, "A 1.8 μ W 60 nV/√Hz Capacitively-Coupled Chopper Instrumentation Amplifier in 65 nm CMOS for Wireless Sensor Nodes," IEEE Journal of Solid-State Circuits, vol. 46, no. 7, pp. 1534–1543, Jul. 2011, doi: 10.1109/JSSC.2011.2143610.
[90] Q. Fan, K. A. A. Makinwa, and J. H. Huijsing, "The Chopping Technique," in *Capacitively-Coupled Chopper Amplifiers*, Q. Fan, K. A. A. Makinwa, and J. H. Huijsing, Eds. Cham: Springer International Publishing, 2017, pp. 11–27. doi: 10.1007/978-3-319-47391-8_2.
[91] C. C. Enz and G. C. Temes, "Circuit techniques for reducing the effects of op-amp imperfections: autozeroing, correlated double sampling, and chopper stabilization," *Proceedings of the IEEE*, vol. 84, no. 11, pp. 1584–1614, Nov. 1996, doi: 10.1109/5.542410.
[92] T. Rooijers, S. Karmakar, Y. Kusuda, J. H. Huijsing, and K. A. A. Makinwa, "31.4 A Chopper-Stabilized Amplifier with -107dB IMD and 28dB Suppression of Chopper-Induced IMD," in *2021 IEEE International Solid- State Circuits Conference (ISSCC)*, Feb. 2021, vol. 64, pp. 438–440. doi: 10.1109/ISSCC42613.2021.9365790.
[93] M. P. Garde, A. Lopez-Martin, R. G. Carvajal, and J. Ramírez-Angulo, "Super Class-AB Recycling Folded Cascode OTA," *IEEE Journal of Solid-State Circuits*, vol. 53, no. 9, pp. 2614–2623, Sep. 2018, doi: 10.1109/JSSC.2018.2844371.
[94] L. Orozco, "Analog Dialogue 47-05, May (2013)," p. 5, 2013.
[95] M. A. P. Pertijs and W. J. Kindt, "A 140 dB-CMRR Current-Feedback Instrumentation Amplifier Employing Ping-Pong Auto-Zeroing and Chopping," *IEEE Journal of Solid-*

State Circuits, vol. 45, no. 10, pp. 2044–2056, Oct. 2010, doi: 10.1109/JSSC.2010.2060253.

[96] C.-G. Yu and R. L. Geiger, "An automatic offset compensation scheme with ping-pong control for CMOS operational amplifiers," *IEEE Journal of Solid-State Circuits*, vol. 29, no. 5, pp. 601–610, May 1994, doi: 10.1109/4.284713.

[97] J. F. Witte, K. A. A. Makinwa, and J. H. Huijsing, "A CMOS Chopper Offset-Stabilized Opamp," *IEEE Journal of Solid-State Circuits*, vol. 42, no. 7, pp. 1529–1535, Jul. 2007, doi: 10.1109/JSSC.2007.899080.

[98] A. T. K. Tang, "A 3 µV-offset operational amplifier with 20 nV/√Hz input noise PSD at DC employing both chopping and autozeroing," in 2002 IEEE International Solid-State Circuits Conference. Digest of Technical Papers (Cat. No.02CH37315), Feb. 2002, vol. 1, pp. 386–387 vol.1. doi: 10.1109/ISSCC.2002.993094.

[99] R. Wu, K. A. A. Makinwa, and J. H. Huijsing, "A Chopper Current-Feedback Instrumentation Amplifier With a 1 mHz 1/f Noise Corner and an AC-Coupled Ripple Reduction Loop," IEEE Journal of Solid-State Circuits, vol. 44, no. 12, pp. 3232–3243, Dec. 2009, doi: 10.1109/JSSC.2009.2032710.

[100] H. Chandrakumar and D. Marković, "A High Dynamic-Range Neural Recording Chopper Amplifier for Simultaneous Neural Recording and Stimulation," *IEEE Journal of Solid-State Circuits*, vol. 52, no. 3, pp. 645–656, Mar. 2017, doi: 10.1109/JSSC.2016.2645611.

[101] E. A. M. Klumperink, S. L. J. Gierkink, A. P. van der Wel, and B. Nauta, "Reducing MOSFET 1/f noise and power consumption by switched biasing," *IEEE Journal of Solid-State Circuits*, vol. 35, no. 7, pp. 994–1001, Jul. 2000, doi: 10.1109/4.848208.

[102] H. Tian and A. El Gamal, "Analysis of 1/f noise in switched MOSFET circuits," *IEEE Transactions on Circuits and Systems II: Analog and Digital Signal Processing*, vol. 48, no. 2, pp. 151–157, Feb. 2001, doi: 10.1109/82.917783.

[103] H. Tian and A. A. El Gamal, "Noise analysis in CMOS image sensors," 2000.

[104] A. G. Mahmutoglu and A. Demir, "Analysis of Low-Frequency Noise in Switched MOSFET Circuits: Revisited and Clarified," *IEEE Transactions on Circuits and Systems I: Regular Papers*, vol. 62, no. 4, pp. 929–937, Apr. 2015, doi: 10.1109/TCSI.2015.2388834.

[105] A. Hassibi and T. H. Lee, "A programmable electrochemical biosensor array in 0.18 /spl mu/m standard CMOS," in *ISSCC. 2005 IEEE International Digest of Technical Papers. Solid-State Circuits Conference, 2005.*, Feb. 2005, pp. 564-617 Vol. 1. doi: 10.1109/ISSCC.2005.1494120.

[106] S. B. Anand and B. Razavi, "A 2.75 Gb/s CMOS clock recovery circuit with broad capture range," in *2001 IEEE International Solid-State Circuits Conference. Digest of Technical Papers. ISSCC (Cat. No.01CH37177)*, Feb. 2001, pp. 214–215. doi: 10.1109/ISSCC.2001.912609.

[107] M. R. Valero Bernal, S. Celma, N. Medrano, and B. Calvo, "An Ultralow-Power Low-Voltage Class-AB Fully Differential OpAmp for Long-Life Autonomous Portable Equipment," *IEEE Transactions on Circuits and Systems II: Express Briefs*, vol. 59, no. 10, pp. 643–647, Oct. 2012, doi: 10.1109/TCSII.2012.2213361.

[108] J. A. Galan, A. J. Lopez-Martin, R. G. Carvajal, J. Ramirez-Angulo, and C. Rubia-Marcos, "Super Class-AB OTAs With Adaptive Biasing and Dynamic Output Current Scaling," *IEEE Transactions on Circuits and Systems I: Regular Papers*, vol. 54, no. 3, pp. 449–457, Mar. 2007, doi: 10.1109/TCSI.2006.887639.

[109] P. R. Surkanti and P. M. Furth, "Converting a Three-Stage Pseudoclass-AB Amplifier to a True-Class-AB Amplifier," *IEEE Transactions on Circuits and Systems II: Express Briefs*, vol. 59, no. 4, pp. 229–233, Apr. 2012, doi: 10.1109/TCSII.2012.2188462.

[110] E. Cabrera-Bernal, S. Pennisi, A. D. Grasso, A. Torralba, and R. G. Carvajal, “0.7-V Three-Stage Class-AB CMOS Operational Transconductance Amplifier,” *IEEE Transactions on Circuits and Systems I: Regular Papers*, vol. 63, no. 11, pp. 1807–1815, Nov. 2016, doi: 10.1109/TCSI.2016.2597440.
[111] J. Beloso-Legarra, C. A. de la Cruz-Blas, A. J. Lopez-Martin, and J. Ramirez-Angulo, “Gain-Boosted Super Class AB OTAs Based on Nested Local Feedback,” *IEEE Transactions on Circuits and Systems I: Regular Papers*, vol. 68, no. 9, pp. 3562–3573, Sep. 2021, doi: 10.1109/TCSI.2021.3090154.
[112] K. N. Leung, P. K. T. Mok, W.-H. Ki, and J. K. O. Sin, “Three-stage large capacitive load amplifier with damping-factor-control frequency compensation,” *IEEE Journal of Solid-State Circuits*, vol. 35, no. 2, pp. 221–230, Feb. 2000, doi: 10.1109/4.823447.
[113] R. S. Assaad and J. Silva-Martinez, “The Recycling Folded Cascode: A General Enhancement of the Folded Cascode Amplifier,” *IEEE Journal of Solid-State Circuits*, vol. 44, no. 9, pp. 2535–2542, Sep. 2009, doi: 10.1109/JSSC.2009.2024819.
[114] W. Wattanapanitch, M. Fee, and R. Sarpeshkar, “An Energy-Efficient Micropower Neural Recording Amplifier,” *IEEE Transactions on Biomedical Circuits and Systems*, vol. 1, no. 2, pp. 136–147, Jun. 2007, doi: 10.1109/TBCAS.2007.907868.
[115] K. Nakamura and L. R. Carley, “An enhanced fully differential folded-cascode op amp,” *IEEE Journal of Solid-State Circuits*, vol. 27, no. 4, pp. 563–568, Apr. 1992, doi: 10.1109/4.126544.
[116] J. Adut, J. Silva-Martinez, and M. Rocha-Perez, “A 10.7-MHz sixth-order SC ladder filter in 0.35-/spl mu/m CMOS technology,” *IEEE Transactions on Circuits and Systems I: Regular Papers*, vol. 53, no. 8, pp. 1625–1635, Aug. 2006, doi: 10.1109/TCSI.2006.879070.
[117] M. Noormohammadi, V. K. Lazarjan, and K. HajSadeghi, “New Operational Transconductance Amplifiers using current boosting,” in *2012 IEEE 55th International Midwest Symposium on Circuits and Systems (MWSCAS)*, Aug. 2012, pp. 109–112. doi: 10.1109/MWSCAS.2012.6291969.
[118] K.- Baek, J.- Gim, H.- Kim, K.- Na, N.- Kim, and Y.- Kim, “Analogue circuit design methodology using self-cascode structures,” *Electronics Letters*, vol. 49, no. 9, pp. 591–592, Apr. 2013, doi: 10.1049/el.2013.0554.
[119] A. Nedungadi and T. Viswanathan, “Design of linear CMOS transconductance elements,” *IEEE Transactions on Circuits and Systems*, vol. 31, no. 10, pp. 891–894, Oct. 1984, doi: 10.1109/TCS.1984.1085428.
[120] Ko-Chi Kuo and A. Leuciuc, “A linear MOS transconductor using source degeneration and adaptive biasing,” *IEEE Transactions on Circuits and Systems II: Analog and Digital Signal Processing*, vol. 48, no. 10, pp. 937–943, Oct. 2001, doi: 10.1109/82.974782.
[121] M. Kachare, A. J. Lopez-Martin, J. Ramirez-Angulo, and R. G. Carvajal, “A compact tunable CMOS transconductor with high linearity,” *IEEE Transactions on Circuits and Systems II: Express Briefs*, vol. 52, no. 2, pp. 82–84, Feb. 2005, doi: 10.1109/TCSII.2004.842065.
[122] P. Monsurro, S. Pennisi, G. Scotti, and A. Trifiletti, “Linearization Technique for Source-Degenerated CMOS Differential Transconductors,” *IEEE Transactions on Circuits and Systems II: Express Briefs*, vol. 54, no. 10, pp. 848–852, Oct. 2007, doi: 10.1109/TCSII.2007.906203.
[123] L. Zuo and S. K. Islam, “Low-Voltage Bulk-Driven Operational Amplifier With Improved Transconductance,” *IEEE Transactions on Circuits and Systems I: Regular Papers*, vol. 60, no. 8, pp. 2084–2091, Aug. 2013, doi: 10.1109/TCSI.2013.2239161.
[124] S. Chatterjee, Y. Tsividis, and P. Kinget, “0.5-V analog circuit techniques and their application in OTA and filter design,” *IEEE Journal of Solid-State Circuits*, vol. 40, no. 12, pp. 2373–2387, Dec. 2005, doi: 10.1109/JSSC.2005.856280.

[125] S. M. Anisheh, H. Abbasizadeh, H. Shamsi, C. Dadkhah, and K. Lee, “98-dB Gain Class-AB OTA With 100 pF Load Capacitor in 180-nm Digital CMOS Process,” *IEEE Access*, vol. 7, pp. 17772–17779, 2019, doi: 10.1109/ACCESS.2019.2896089.
[126] J. Ramirez-Angulo and M. Holmes, “Simple technique using local CMFB to enhance slew rate and bandwidth of one-stage CMOS op-amps,” *Electronics Letters*, vol. 38, no. 23, pp. 1409–1411, Nov. 2002, doi: 10.1049/el:20020764.
[127] H. Tian, B. Fowler, and A. E. Gamal, “Analysis of temporal noise in CMOS photodiode active pixel sensor,” *IEEE Journal of Solid-State Circuits*, vol. 36, no. 1, pp. 92–101, Jan. 2001, doi: 10.1109/4.896233.
[128] P. A. J. Nuyts, P. Reynaert, and W. Dehaene, “Continuous-Time Digital Design Techniques,” in *Continuous-Time Digital Front-Ends for Multistandard Wireless Transmission*, P. A. J. Nuyts, P. Reynaert, and W. Dehaene, Eds. Cham: Springer International Publishing, 2014, pp. 125–185. doi: 10.1007/978-3-319-03925-1_4.
[129] H. Pekau, A. Yousif, and J. W. Haslett, “A CMOS integrated linear voltage-to-pulse-delay-time converter for time based analog-to-digital converters,” in *2006 IEEE International Symposium on Circuits and Systems*, May 2006, p. 4 pp. – 2376. doi: 10.1109/ISCAS.2006.1693099.
[130] M. Maymandi-Nejad and M. Sachdev, “A monotonic digitally controlled delay element,” *IEEE Journal of Solid-State Circuits*, vol. 40, no. 11, pp. 2212–2219, Nov. 2005, doi: 10.1109/JSSC.2005.857370.
[131] B. I. Abdulrazzaq, I. Abdul Halin, S. Kawahito, R. M. Sidek, S. Shafie, and N. A. Md. Yunus, “A review on high-resolution CMOS delay lines: towards sub-picosecond jitter performance,” *SpringerPlus*, vol. 5, no. 1, p. 434, Apr. 2016, doi: 10.1186/s40064-016-2090-z.
[132] V. K. Lazarjan, M. N. Khiarak, A. B. Gashti, A. Garnier, and B. Gosselin, “Miniaturized Wireless Cell Spectrophotometer Platform in Visible and Near-IR Range,” in *2018 IEEE Life Sciences Conference (LSC)*, Montreal, QC, Canada, Oct. 2018, pp. 29–32. doi: 10.1109/LSC.2018.8572252.
[133] “Simple Op Amp Measurements | Analog Devices.” https://www.analog.com/en/analog-dialogue/articles/simple-op-amp-measurements.html (accessed Jan. 22, 2022).
[134] “Measuring Noise of Low-Fixed-Gain Differential Amplifiers | Analog Devices.” https://www.analog.com/en/analog-dialogue/articles/low-fixed-gain-diff-amp-noise.html (accessed Jan. 17, 2022).